Computer Aided Medical Procedures
(CAMP)
Prof. Dr. Nassir Navab

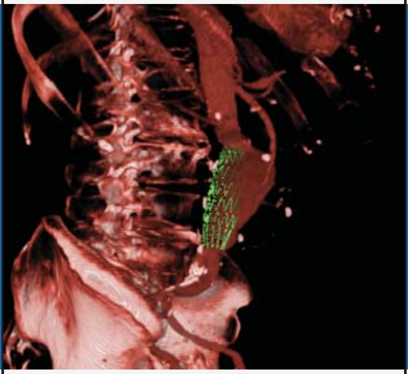

Dissertation

New Approaches to Computer Assistance for Endovascular Abdominal Aortic Repairs

Stefanie Demirci

Fakultät für Informatik
Technische Universität München

TECHNISCHE UNIVERSITÄT MÜNCHEN

Chair for Computer-Aided Medical Procedures & Augmented Reality

New Approaches to Computer Assistance for Endovascular Abdominal Aortic Repairs

Stefanie Demirci

Vollständiger Abdruck der von der Fakultät für Informatik der Technischen Universität München zur Erlangung des akademischen Grades eines

Doktors der Naturwissenschaften (Dr. rer. nat.)

genehmigten Dissertation.

Vorsitzender: Univ.-Prof. Dr. Johann Schlichter

Prüfer der Dissertation:

1. Univ.-Prof. Dr. Nassir Navab
2. Prof. Dr. Franjo Pernus
   University of Ljubljana/Slowenien

Die Dissertation wurde am 02.11.2010 bei der Technischen Universität München eingereicht und durch die Fakultät für Informatik am 06.04.2011 angenommen.

To Mikail, my light

Abstract

With the establishment of minimally-invasive procedures for abdominal surgery, image guidance has become more and more important. The intraoperative use of medical imaging data has on the one hand increased the safety and robustness of such procedures. On the other hand, it has increased the radiation exposure. The introduction of computer based navigation systems has improved the situation to a great extent. However, they are not optimized for every application in abdominal catheter interventions.

This work presents new approaches to computer assistance for endovascular abdominal aortic repairs. In the current clinical workflow there is no technical guidance during the intervention except for two dimensional X-Ray images. An integration of preoperative three dimensional image data is further complicated by medical instruments occluding relevant anatomical structures in the images. Here, we introduce interventional registration methods that are able to handle such occlusions and further image dissimilarities. Thereby, contrast removal and disocclusion techniques are integrated within an image registration procedure. Furthermore, we show for the first time that a detection of the stent graft in the interventional image and a three dimensional recovery of its shape can be obtained at the same time. This allows image-based tracking of the prosthesis and simultaneous visualization within a volume rendering of the patient scan. All introduced methods are completely image based and do not require additional equipment to be introduced into the intervention room. The thesis is completed by presenting detailed evaluation of the methods using both synthetic images and real clinical data.

Keywords:
Image guided intervention, medical image registration, robust similarity measures, disocclusion, stent detection.

Zusammenfassung

Mit Einführung von minimal-invasiven Verfahren in der Bauchchirurgie hat die intraoperative Bildunterstützung mehr und mehr an Bedeutung gewonnen. Der intraoperative Einsatz bildgebender Daten erhöht auf der einen Seite die Sicherheit und Robustheit dieser Verfahren. Auf der anderen Seite wurde die Strahlenbelastung dadurch erheblich verstärkt. Die Einführung Computer-basierter Navigationssysteme hat einen großen Teil dazu beigetragen die Situation zu verbessern. Allerdings sind sie nicht für jede Art von Bauch-Kathetereingriffen optimiert.

Diese Arbeit stellt neue Ansätze vor wie mit Hilfe von moderner Computermethodiken endovaskuläre Bauchaortareparaturen technisch und bildlich unterstützt werden können. Im aktuellen klinischen Arbeitsablauf gibt es keine technische Navigationsunterstützung während des Eingriffs mit Ausnahme von zweidimensionalen Röntgenaufnahmen. Da vor allem bei Baucheingriffen relevante anatomische Strukturen in den Röntgenbildern durch medizinische Instrumente verdeckt werden können, ist eine Integration der präoperativen dreidimensionalen Bilddaten durch existierende Methoden nur unter erheblichem Robustheitsverlust möglich. Wir stellen hier Methoden zur interventionellen Bildregistrierung vor, die in der Lage sind mit solchen Verdeckungen und weiteren Bildunterschieden umzugehen. Dazu werden spezielle robuste Ähnlichkeitsmaŝe sowie Algorithmen zur Disokklusion entwickelt und in die Bildregistrierung integriert. Darüber hinaus zeigen wir zum ersten Mal, dass es möglich ist den Stentgraft im interventionellen Bild zu detektieren und gleichzeitig seine dreidimensionale Form wiederherzustellen. Dies ermöglicht bildbasiertes Tracking der Prothese und gleichzeitige Darstellung innerhalb eines Volume-Rendering des präoperativen Patientenbildes. Alle vorgestellten Methoden sind ausschließlich bildbasiert und benötigen keine zusätzliche technische Ausrüstung, die in den Interventionsraum eingegliedert werden muss. Die Arbeit wird durch detaillierte Auswertungen der Methoden mit synthetischen Bildern als auch realen klinischen Daten abgerundet.

Schlagwörter:
Bildgeführte Intervention, medizinische Bildregistrierung, robuste Ähnlichkeitsmaße, Disokklusion, Stenterkennung.

Acknowledgments

I would like to express my deepest gratitude to Prof. Nassir Navab for the extraordinary supervision and his unexceptional support. Besides many motivating and creative ideas in endless meetings at unusual locations and time, he has always had an open ear for all kind of challenges - professional and personal - I had to face during four years. I also like to thank all the people from CAMP for the warm welcome in their group and their support. In particular, I want to thank Martin Groher, Max Baust, and Darko Zikic for sharing their enormous knowledge and experience. I also owe many thanks to Martin Horn and Martina Hilla for their continuous technical and administrative support throughout the years.

Also, I want to thank my students Guy Lejeune, Michael Emmersberger, and Markus Urban without whom this PhD thesis would not have been possible. I am also grateful for all the help and valuable explanations I got from my physician partners, in particular Frode Manstad-Hulaas, Dr. med. Reza Ghotbi, and Dr. med. Mojtaba Sadeghi. Of course, I also thank Siemens AX for the one-year financial support, and Klaus Klingenbeck-Regn, Martin Ostermeier, and Marcus Pfister for valuable input.

Finally I would like to thank my family for motivating me throughout the years even in challenging times. Selcuk, I owe you so much!

Contents

1. Introduction

The field of vascular surgery has seen a tremendous evolvement in the past decades. The care of patients with vascular diseases including the direct repair of lesions of the vascular tree, was previously the uncontested province of the vascular surgeon. The first use of medical images (X-ray) as an adjunct to surgery reported only a few months after the discovery of X-rays in 1895 [110], marked the dawn of the *image guided surgery* (IGS) era. The subsequent rapid progress of IGS was predominantly made possible by the development of various medical imaging technologies including endoscopic and laparoscopic imaging, Ultrasound (US), and molecular imaging. For a complete review on the history of IGS the reader is referred to [136].

In the late 1960s, Charles Dotter, a radiologist, pioneered the concept of *endovascular intervention* by being able to dilate stenotic atherosclerotic lesions in the iliac arteries using a series of catheter of increasing diameter. Very soon, *catheter-based therapy* became a popular alternative for treating certain vessel lesions. The most recent development has been a hybrid of a limited surgical exposure and the catheter-based introduction of a stent graft to treat aneurysmal disease. Taken its name from the English dentist Charles Stent who developed a thermoplastic material for taking impressions of toothless mouths in 1856 [138], stent grafts became the major impetus for endovascular procedures excluding an aneurysm, closing an arteriovenous fistula, and reconstructing the central lumen of a dissected vessel.

In contrast to conventional open surgery, *endovascular interventions* are performed minimally-invasive, i.e. only a small incision is needed to insert instruments such as catheters and guide wires. Location and navigation of these instruments is then performed under fluoroscopic and angiographic image guidance.

As *endovascular intervention* became competitive with and, in many cases, more desirable than direct vascular surgery, the traditional role of the vascular surgeon was challenged. To emphasize the fact that intra-arterial intervention was another form of surgery and, hence, should be included in the repertoire of a vascular surgeon, the term *endovascular surgery* was invented as an alternative to *endovascular intervention*.

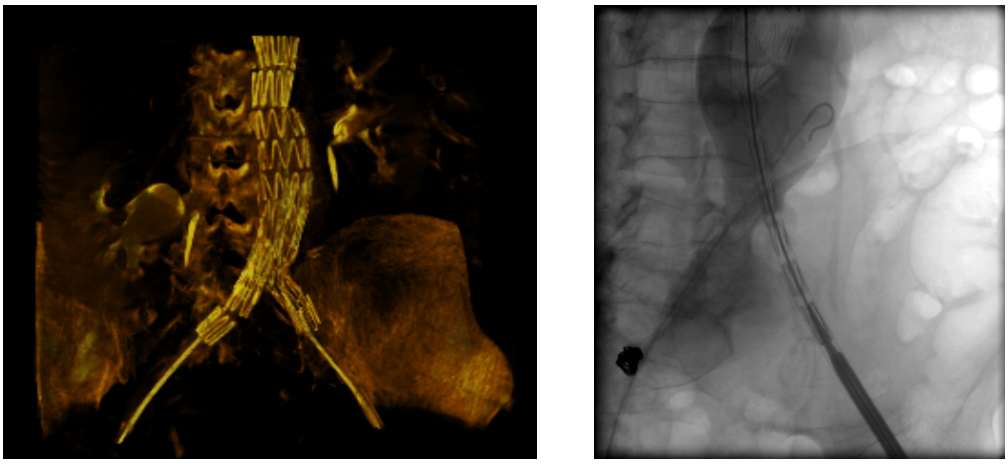

Figure 1.1.: Interventional X-ray images with occluding medical instruments

1.1. Motivation

> *"There must be a perfect coordination between the eyes on the monitor and the foot on the fluoro pedal, interconnected by a brain that thinks interventionally!"*

This quotation found in a textbook for medical students [26], points out very nicely the challenges a vascular surgeon has to face nowadays. Besides deep knowledge about the history of vascular diseases and extensive training in conventional treatment methods, they have to acquire certain *endo-skills* and *habits* including remote catheter-mediated actions, indirect visualization, interventional mindset, and catheter and imaging skills. Of course, it is not possible to eliminate these requirements, but with the help of computer assistance visualization can be made a lot more intuitive and thereby support the physician's actions.

The workflow of *endovascular interventions* requires that images of patients are acquired before the treatment (preoperatively) for diagnosis and/or procedure planning. In order to allow most reliable diagnosis and most accurate treatment planning, most preoperative images are acquired in 3D with high quality settings. In contrast, imaging data acquired during medical procedures (intraoperatively), is of less quality with lower signal-to-noise ratio and lower dimensionality (2D slices or 2D projections). Due to high zooming capabilities of intraoperative imaging devices, they yield a higher spatial resolution, such that the state of instruments and patient anatomy over time can be assessed quite accurately. Recent advances in intraoperative imaging have brought 3D acquisitions into operating rooms. However, they do not yield nearly the same quality as preoperative scanners and due to hard time constraints and high X-ray dosage, are performed rarely.

The registration of pre- and intraoperative data sets would fuse patient anatomy information of superior quality with information capturing the current state of the operation. In addition to a speed up in treatment duration and reduction of harmful radiation that physicians and patients are exposed to, such a registration would pave the way for new image-guided roadmapping and navigation techniques Although registration systems are already commercially available, they are not optimized specifically for *endovascular surgeries*. Most such software works with external (fiducials) or anatomical landmarks launching a point-based registration method. Here, one problem is the durability of fiducials that need to be attached to the patient throughout the entire procedural workflow, starting from the acquisition of the preoperative image until the end of the actual intervention. From experience, these stickers gets displaced very easily by patients' movement. Another disadvantage also for anatomical landmarks, is the fact that, in particular in abdominal interventions, medical instruments such as catheters, guide wires, stent grafts, clips, and scissors, are present within the interventional images (see Fig. 1.1) might occlude the selected points that are crucial for the registration step. As a solution to the aforementioned problems would be the use of intensity-based methods and some commercially available systems also provide this choice. However, even the incorporation of robust similarity measures can not prevent instability due to severe outliers introduced by area-wide occlusions.

A second challenge for image guidance during EVAR is the appropriate visualization of the registration result. Whereas in other image guided surgery domains external tracking is used to locate the current position of a medical tool and visualize it within the preoperative 3D scan, this is not an option for endovascular interventions. Although research in sensor technology has lead to very small devices that can be mounted onto a guide wire or stent graft catheter, they do not survive inside the aorta where they are exposed to very high pressure and flow. Therefore image-based solutions are highly needed.

1.2. Contributions

In the course of this work, we present several approaches for computer assistance for endovascular abdominal aortic repair including 2D-3D and 3D-3D registration algorithms as well as stent graft detection methods. Following, we present a summary of the technical contributions in this thesis, along with the corresponding publications.

Based on our publications [33, 93, 32], we propose two novel robust similarity measures that are able to handle image dissimilarities and occlusions for rigid 3D-3D registration. By a number of experiments, we show that these measures significantly improve the accuracy and robustness for matching intraoperative C-arm cone-beam CT images with preoperative CTA scans compared to existing similarity measures. This conclusion was also confirmed by a medical study comparing our registration method to a commercially available procedure integrated within Siemens AXIOM Artis workstations.

In order to address the problem of occluding medical instruments, we present disocclusion-based 2D-3D registration of medical images [33, 32]. Therefore, we introduce two novel disocclusion techniques, namely *Spline Interpolation* and *Poisson*

Editing, that are integrated into a 2D-3D registration framework. In our processing pipeline, the occluded region is first processed by a disocclusion technique that reconstructs the obstructed image parts. Then, a robust 2D-3D image registration algorithm is computed on the processed interventional image and a preoperative 3D scan of the patient. Besides our novel techniques, we also include *Digital Inpainting* as disocclusion method into an evaluation framework using *Gradient Correlation*,*Gradient Difference*,*Huber Gradient Correlation*, and *Tukey Gradient Correlation* as similarity measures.

In this thesis, we show for the first time that image-based tracking of the prosthesis and simultaneous visualization within a volume rendering of the patient scan is possible. By using a model-based approach, we are able to detect the stent graft in the interventional image and recover its shape in 3D at the same time. The method is fully automatic and does therefore not interrupt the medical workflow. By an automatic preprocessing and choosing a global-to-local registration approach, we are able to abandon any user interaction and still meet the desired robustness. The complexity of our registration scheme is reduced by including constraints that resemble the geometric properties of the stent graft, and by applying semi-simultaneous optimization strategy.

1.3. Outline of the Thesis

This thesis is subdivided into three parts according to the introduction of background information, state-of-the-art review, and presentation of novel approaches to computer assistance for endovascular aortic repair.

Part I: Background Information

CHAPTER 2: MEDICAL BACKGROUND

This chapter gives an overview of medical imaging technologies relevant for this work followed by a short introduction in the abdominal vessel system with main focus on the aorta. Eventually, one selected disease of the aorta, abdominal aortic aneurysm (AAA), is explained.

CHAPTER 3: TECHNICAL PRINCIPLES

The methodological basis of this thesis is presented in this chapter. After clarifying our notation and usage of images and image functions, the basics of medical image segmentation and registration are detailed. We also give an introduction to the concept of disocclusion.

Part II: State of the Art

CHAPTER 4: TREATMENT OF ABDOMINAL AORTIC ANEURYSMS

The state-of-the-art treatment method is endovascular aortic repair (EVAR) which we describe in detail within this chapter. Here, an exact analysis of the medical and, more importantly for this thesis, the imaging workflow is given. Additionally, we present a critical analysis in terms of challenges and applicability of state-of-the-art algorithms providing computer assistance for EVAR.

CHAPTER 5: DISSIMILARITY IN INTERVENTIONAL IMAGE REGISTRATION

The clinical application that is focused in this work, Transarterial Chemoembolization. A short introduction in liver vessel systems and tumor treatment followed by a critical analysis in terms of challenges and applicability of state-of-the-art algorithms.

Part III: New Approaches to Computer Assistance for Endovascular Abdominal Aortic Repairs

CHAPTER 6: INTERVENTIONAL IMAGE REGISTRATION: ADDRESSING DISSIMILARITY IN IMAGES

We present an algorithm for robust rigid 2D-3D and 3D-3D registration that is able to handle image dissimilarities such as varying presence of contrast and small perforated occlusions.

CHAPTER 7: DISOCCLUSION-BASED IMAGE REGISTRATION

Targeting the problem of large, area-wide occlusions in the interventional images, we investigate the effect of disocclusion methods to accuracy and robustness of rigid 2D-3D registration. We therefore introduce two novel techniques for reconstructing occluded image parts.

CHAPTER 8: MODEL-BASED DETECTION AND 3D RECOVERY OF STENT SHAPE

A novel algorithm for automatic detection of the stent graft in intraoperative 2D images is presented. By employing a model-based approach, we are able to simultaneously recover the 3D stent shape and visualize it within a preoperative CTA scan of the same patient.

CHAPTER 9: CONCLUSION

A short summary followed by a discussion of the integration of the registration algorithms into clinical workflow and future work.

Appendix

A. MEDICAL STENTS

The large variety of medical stents is presented in this chapter. The focus is laid on the classification of vascular stents and stent grafts in terms of their different design and application.

B. AAA-THROMBUS SEGMENTATION

In this chapter, we present a solution to the problem to accurately segment the thrombus of AAAs in preoperative 3D images. By using a hybrid approach that integrates local as well as global image information and combines it with additional shape constraints, our algorithm is able to overcome leakage into adjacent objects.

C. SASOMI- AN INTUITIVE GUI FOR AAA-THROMBUS SEGMENTATION REFINEMENT

The design of an interactive graphical user interface is introduced providing an intuitive solution for refining an automatic AAA presegmentation.

D. QUANTIFICATION OF ABDOMINAL AORTIC DEFORMATION AFTER EVAR

Here, we present a method for quantifying the deformation of an aneurysmatic aorta imposed by an inserted stent graft device.

E. ABBREVIATIONS

This chapter includes a list of abbreviations used throughout this thesis.

F. PUBLICATIONS

All publications contributed to the scientific community during this work are listed in this chapter.

Part I.

Background Information

2. Medical Background

Before addressing the technical details, let us first introduce some medical background around the main application focus of this thesis. This chapter gives an overview of different medical imaging techniques that are involved in the treatment process of aortic aneurysms and details the disease itself.

2.1. Medical Imaging

There are mainly two types of medical imaging technologies classified in common literature. *Anatomical Imaging* summarizes all modalities that produces images with anatomical information only whereas *Functional Imaging* includes techniques which measure biological and physiological processes. In the following sections some functional and anatomical imaging techniques are explained. Mind that this thesis does not aim at giving an entire overview of all existing medical imaging techniques (the interested reader is referred to [3]) but rather focus on those that are involved in the treatment process of aortic aneurysms.

2.1.1. Computed Tomography (CT)

Computed Tomography (CT) has been the first image intensifier that produces digitalized information, which can be directly processed by a computer [27]. The device consists of an X-ray source and a detector both mounted on a gantry. As in conventional radiology, radiation passes the human body from the X-ray source and is attenuated by different human tissues to varying extents. In today's common spiral CT, the table is moved continuously in the longitudinal body axis while the gantry rotates around the patient.

A CT scan consists of several x-ray images, representing cuts of the anatomy of an individual along one direction. In most cases, the produced images represent axial slices of the patient's anatomy. This data is generated using an x-ray source that rotates around the patient. An x-ray sensor plate is positioned on the opposite side of the source and is rotated with it. Many scans, at multiple rotation angles of the source-sensor system, are progressively acquired, as the patient passes gradually through the field of electromagnetic emission. The data stream thereby represents the varying radiographic intensity detected when the rays reach the sensor. After a rotation of 360° of the source-sensor system, the data is computer processed in order to calculate cross-sectional estimations of the radiographic density. Further advanced technology with more effective computers and newer software strategies can process not only stationary cross-sections but also continuously changing ones, as the patient slides slowly through the x-ray circle. These are called helical or spiral CTs, whose processing systems can automatically generate 3D volumetric information by integrating the data of the individual slices. These 3D models can sometimes be rotated and scaled for multiple perspective views and are able to demonstrate the acquired anatomy very accurately. Stationary devices can also reproduce 3D models by interpolation of the missing information between the images. However, they are of a lower quality, because of that missing data. Further software of CT intensifiers can reproduce sagital and frontal slices of the acquired region.

The radiographic density, detected by the sensor, is expressed in Hounsfield units (HU). They form a spectrum from -1000 (black) to 1000 (white) to classify all kinds of organic material of the body in CT scans. Each pixel is assigned a numerical value, which represents the average of all attenuation values contained within the corresponding position of the patients body. The range of conventional CT scanners is 2000 HU wide, although some modern scanners have a greater range of HU of up to 4000. Alternative CT software allows Hounsfield units to be displayed with color maps, so that every tissue (i.e. organ or structure of interest) can be better distinguished.

In Computed Tomography Angiography (CTA), the patients vasculature can be emphasized by injecting a fluid with high X-Ray attenuation, a so-called contrast agent, prior to imaging.

The invention of CT scanners in 1972 goes back to the British engineer Godfrey Hounsfield working for EMI. While the company is commonly known for the recording and marketing of popular music, it also maintained a research department (EMI Laboratories). Interestingly, the development of CT was likely to be driven by the world-famous music group The Beatles, whose success have helped raising the urgently needed funds [42].

2.1.2. Magnetic Resonance Imaging (MRI)

In contrast to the X-Ray based CT imaging technique, Magnetic Resonance Imaging (MRI) does not use any ionizing radiation. Based on the principle of nuclear magnetic resonance, it provides much greater contrast between the different soft tissues of the body than CT, thus, making it especially useful in neurological, musculoskeletal, cardiovascular, and oncological imaging.

MRI scanners create a strong magnetic field magnetizing small biological magnets in the human body consisting of protons located in the nucleus of the hydrogen atom [27]. The body is then stimulated with radio waves in order to change the steady-state orientation of protons. Once the radio wave emission is stopped, the magnetic protons emit radiofrequency signals as their excitation decays. The signals vary in intensity according to nuclear abundance and molecular chemical environment. They are then used to construct internal images of the body by computerized axial tomography.

There are several MR Angiography techniques, either based on flow effects or on contrast [27]. Injection of contrast agents similar to CTA, is currently the most common method of acquiring MRA. Here, however, the contrast agent need to have magnetic characteristics and be of extracellular nature. Another possibility is to use time of flight (TOF) technique where a short echo time and flow compensation is applied in order to make flowing blood much brighter than stationary tissue. As this method is dependent on flowing blood, areas with slow flow (such as large aneurysms) or flow that is in plane of the image may not be well visualized. In phase contrast imaging (PC-MRA), the phase of the MRI signal is manipulated by varying magnetic fields. An image acquisition that is orthogonal to the fields is then acquired and the difference of the two image is calculated. Static tissues such as muscle or bone will subtract out, however moving tissues such as blood will acquire a different phase since it moves constantly through the gradient, thus also giving its speed of the flow. In order to visualize flow in all direction at a time, three separate image acquisitions must be computed. Despite the slowness of this method, the strength of the technique is that in addition to imaging the flowing blood, quantitative measurements of blood flow occur at the same time.

Magnetic resonance imaging is a relatively new technology. Only some years after the publication of a first MR image in 1973 by Paul Lauterbur (State University of New York), the first human scan was made in 1977 [42]. By comparison, the first human X-ray image was taken in 1895.

2.1.3. Positron Emission Tomography (PET)

First introduced in the late 1950s, *Positron Emission Tomography* (PET) is a nuclear imaging method that visualizes functional processes in the human body [87]. Depending on the part of the body in question, a positron emitting radiotracer is selected and injected into the patient. While he is moved through the scanner, planar images of the distribution of radioactivity are obtained from many angles around him. After the employment of mathematical image reconstruction methods this as a whole allows the 3D and even 4D (the 4th dimension being time) visualisation of tracer concentration.

The most commonly used radioisotope is FDG (^{18}F-Fluorodesoxyglucose) analyzing the glucose metabolism. This is of interest in particular for medical imaging of brain, heart, and tumours, as respective cells have a high carbon hydrate metabolism.

In recent years, techniques have emerged that combine anatomical with functional imaging techniques facilitating a more accurate localisation of functional information in the anatomical background of the patient. The invention of PET/CT scanners in 1998 [133] has improved the clinical workflow by scanning the patient quasisimultaneously and making the standard PET transmission scan redundant. Current research projects [31, 122] investigate a similar technique for the combination of MRI and PET scanners.

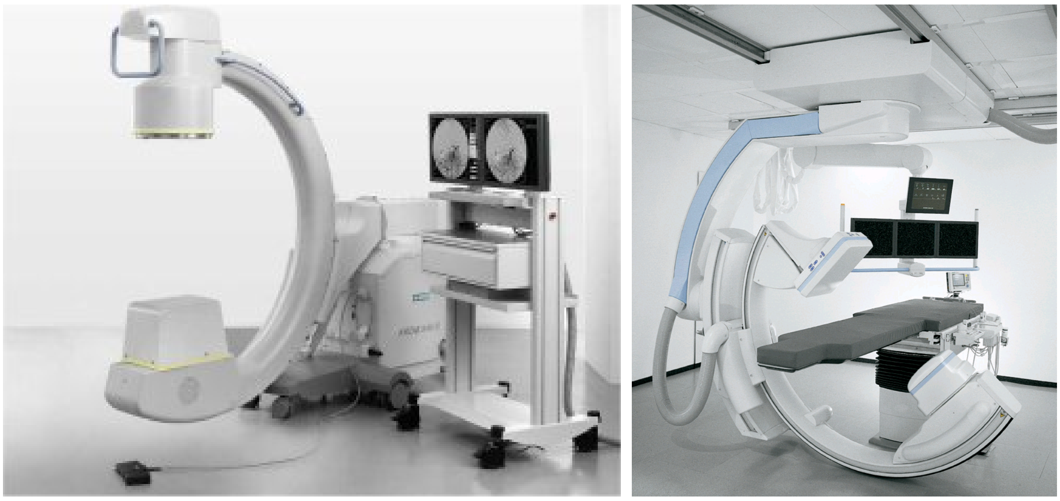

(a) mobile C-arm with image intensifier (b) angiography suite with integrated flatpanel C-arm

Figure 2.1.: Intraoperative C-arm systems.

2.1.4. Ultrasonography (US)

In *Ultrasonography* (US), a hand-held transducer is put in direct contact with the patients skin, using some coupling gel to avoid any air in-between [27]. The transducer emits short ultrasound pulses that propagate into the body and are reflected by the anatomic structures. The returning echoes are converted into brightness values and displayed on the screen as a 2D image, representing a slice of anatomic information pointed from the transducer downwards into the patient.

Compared to other anatomical imaging techniques like CT and MRI, the analysis of US images requires more education and experience as the produced images are not as sharp and clear [27]. However it does not employ ionizing radiation and has therefore found wide applications in medical imaging. Also, the inexpensiveness and portability of the US equipment is a further advantage compared to CT or MRI.

2.1.5. Intraoperative X-ray Imaging

The most commonly used intraoperative imaging device is a so-called C-arm. Initially used in general surgery or orthopedic applications, C-arms are now described by both manufacturers and users as highly versatile, thanks to the technological advancements made since the original designs. In fact, C-arm usage recently has expanded to also include minimally invasive surgeries in cardiac and vascular applications.

A C-arm consists of a C-shaped machine with an X-ray source and a detector plane each mounted at respective end of the C [145]. The patient can be screened from different viewpoints by by moving the table into the iso-center of the C and altering two possible angles, table position, and zoom. Similar to CT imaging, the physical law of radiation attenuation is used to produce images. In contrast to CT, where a fan beam is traveling through the object (creating only few lines of intensities), C-arms emit a cone-beam of X-rays that fills a 2D array with intensities.

The minimal functionality of C-arms that are currently used in hospitals covers fluoroscopic, angiographic, and digital subtraction image acquisition. Fluoroscopic imaging creates image sequences of up to 15 FPS and thereby allows the physician to obtain real-time moving images of the internal structures of a patient. Being not visible in fluoroscopic sequences, the vascular system can be highlighted by angiographic imaging where radio-opaque contrast is injected into the vessels of interest and X-ray images are captured with a frame rate of approximately 5 FPS. In digitally subtracted angiography (DSA), a non-contrasted X-ray image is subtracted from a contrasted one to visualize the vessels only. The spatial resolution of fluoroscopic, angiographic images or DSAs currently goes down to 0.13mm per pixel.

Depending on the integrated detector system, C-arms use mainly two different technologies for transferring X-rays into gray values and thereby producing digitized images (see Fig. 2.1). An *image intensifier* first converts photons into electrons that, by acceleration, produce photons that can be captured by a CCD camera. A big disadvantage of this technology is the emerging image distortion caused by a curve-to-plane warping and the earth magnetic field. For calibration issues, it is important to know about the presence of distortion in order to determine corresponding points of 2D image plane and 3D image. In order to overcome this major drawback, *flat panel* technology has been introduced. It transfers X-rays into light rays and use thin-film-transistor technology to detect those rays by elements with the size of a pixel. As an advantage, this technology yields lower patient dose and increases image quality.

As an advancement of conventional mobile C-arms (Fig. 2.1(a)), fixed angiography suites (Fig. 2.1(b)) provide powerful functionality in particular for vascular applications[67, 39]. The integrated stationary C-arms have the ability to perform a rotational run around the patient to acquire 150-500 projection images from different viewpoints allowing cone beam CT reconstructions. Additional, flat panel detectors provide an efficient and practically distortion free environment. With this, 3D volumes can be computed in less than 1 minute with a spatial resolution of down to $0.4mm^3$, either visualizing 3D vasculature [55] or intensity volumes measured in Hounsfield units [128]. Up to now, preoperative CT scanners still have a better Hounsfield resolution than intraoperative C-arms [128]. A number of terms have emerged in the literature to describe these new volumetric imaging technologies, including C-arm CT, cone-beam CT, cone-beam volume CT, volume CT, angiographic CT, and flat-panel CT [103]. In the remainder of this work, we will use the term C-arm cone-beam CT to refer to a 3D reconstruction of projection images aquired by a rotational run of a stationary flat panel C-arm. When using the term angiography suites, we refer to any commercially available interventional suite that is equipped with a stationary C-arm that is able to produce C-arm cone-beam CT images.

Stationary C-arm machines can be optionally equipped with two (biplane) X-ray-source detector systems where the two image planes are usually related by a

90 degree rotation relative to each other. Especially minimally invasive neurological surgeries are typically performed using biplane C-arms, whereas abdominal or cardiac procedures are usually monitored by monoplane imaging systems with just one X-ray-source detector system.

2.1.6. DICOM-Standard

Digital Imaging and Communications in Medicine (DICOM) is a standard for handling, storing, printing, and transmitting information in medical imaging. Besides a file format definition it includes a network communications protocol which is an application protocol that uses TCP/IP to communicate between systems.

Due to the great variety of medical imaging devices and the requirements to store all acquired image material as well as to communicate between the different devices, the American College of Radiology (ACR) and the National Electrical Manufactures Association (NEMA) were first to release a standard, ACR/NEMA 300, in 1985 [112]. In the following years, several extensions were created, like Papyrus developed by the University Hospital of Geneva (Switzerland) and SPI (Standard Product Interconnect) supported by Siemens Medical Systems and Philips Medical Systems. A first large scale deployment of this technology was made in 1992 where Siemens Medical Systems and others deployed the first US military Picture Archiving and Communications System (PACS) at all major Army and Air Force medical treatment facilities. In 1993 the third version of the standard under a different name, DICOM 3.0, was released in which network support was added and the Conformance Statement was introduced. Officially, the latest version of the standard is still 3.0, however, it has been constantly updated and extended since its first publication.

The DICOM format transmits data in an hierarchical model, the *real world information model* [98], grouping information into data sets. It is divided into four layers: patient, study, series, and instance. This means that every instance of an DICOM object includes all information that is needed in order to assign it to a certain image series within a certain study of the same patient. Additionally, the DICOM data object has one special attribute containing the image pixel data. For many modalities, this corresponds to a single image. However, the attribute may contain multiple frames or slices, allowing storage of multi-frame and multi-dimensional data. The compression of pixel data can be accomplished using common standards such as JPEG, JPEG Lossless, JPEG 2000, and Run-length encoding (RLE).

2.2. The Aorta

Every human body contains an intricate network of strong and flexible blood vessels called veins and arteries whose purpose is to carry blood to and from the heart in order to nourish body cells. The aorta originates in the left ventricle of the heart

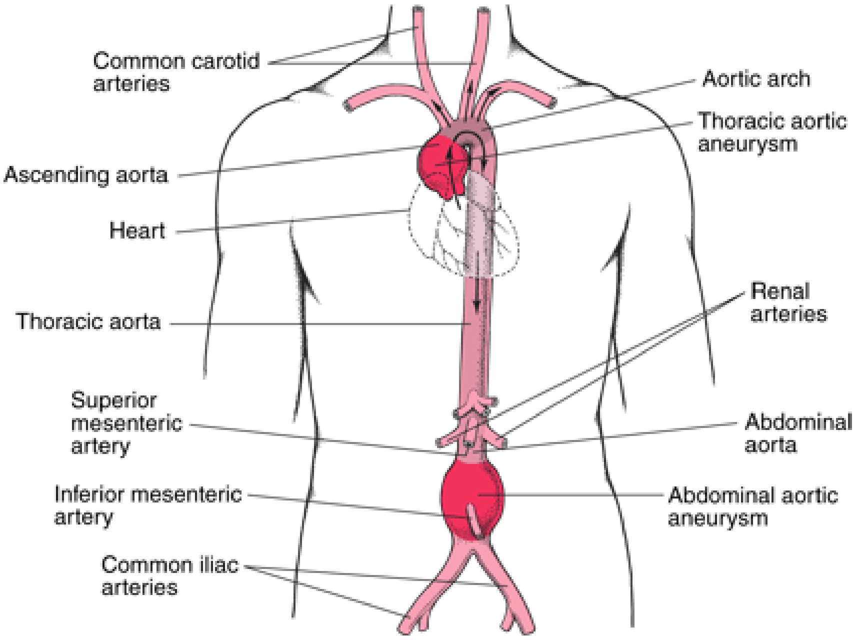

Figure 2.2.: Major vessels of the aorta

as main artery of the circulation system (Figure 2.2[1]) and is responsible for the blood supply of the entire body. It belongs to the arteries of elastic type (*arteriae elastotypica*), whose wall is separated in three layers: the outer (*tunica externa* or *adventitia*), the middle (*tunica media*) and the inner (*tunica interna* or *intima*). It ends up in the aortic bifurcation (*bifurcatio aortae*), where it is further divided in the two iliac arteries. The aorta is seperated into four parts. The ascending part (*pars ascendens aortae*) is the area where the coronary arteries of the heart emerge. It is in continuity with the arch of the Aorta (*arcus aortae*), from which three main arteries spring up to supply the upper body: the brachiocephalic trunk (*truncus brachicephalicus*) for the right head and arm, the left common carotid (*A. carotis communis sinistra*) for the left head and the left subclavian (*A. subclavia sinistra*) for the left arm. The subsequent part is called descending or thoracic (*pars descendens aortae*) and it ends up in the diaphragm. The last one is the abdominal part (*pars abdominalis aortae*) with bifurcations for all the abdominal organs: the celiac trunk (*truncus coeliacus*), the renal arteries (*Ae. renales*), the superior mesenteric (*A. mesenterica superior*) and the inferior mesenteric (*A. mesenterice inferior*).

The aortic vessel wall consists of three main layers [139] (see Figure 2.3[2]).

Intima. Also denoted as *tunica intima*, this layer consists of endothelial cells as well as fine,elastic and collagen fibers. A number of circularly arranged elastic bands

---

[1] From The Merck Manual of Medical Information - Second Home Edition, edited by Mark H. Beers. Copyright 2003 by Merck & Co., Inc., Whitehouse Station, NJ. Available at: `http://www.merck.com/mmhe/sec03/ch035/ch035b.html`.

[2] From Euan A. Ashley,Josef Niebauer: Cardiology explained. Copyright 2004 by Remedica, Chicago, IL. Available at: `http://www.ncbi.nlm.nih.gov/bookshelf/br.fcgi?book=cardio&part=A196`.

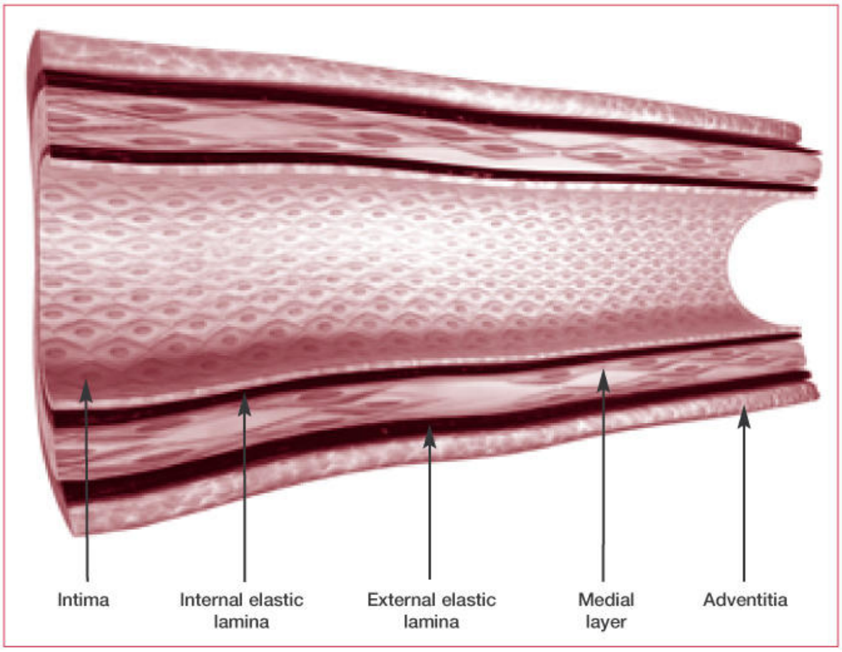

Figure 2.3.: The aortic wall

called the *internal elastic lamina* forms the border to the next outer layer.

Media. The thickest layer, also called *tunica media*, is mainly composed of diagonally oriented smooth muscle cells and only rare amount of elastic and collagen fibers. The border to the most outer layer is formed by another thick elastic band called *external elastic lamina*.

Adventitia. This outermost layer, also known as *tunica externa*, is mostly composed of longitudinal, elastic and collagen fibres mixed with smooth muscel cells.

In the larger blood vessels of the body, such as the aorta, the surrounding of the adventitia is composed of the *vasa vasorum*, a network of small nutrient capillaries.

2.3. Abdominal Aortic Aneurysm (AAA)

2.3.1. Definition

Aneurysms are defined as permanent, irreversible, localized dilatations of the arteries (see Fig. 2.4[3]). According to the German Society of Vascular Surgery and Vascular Medicine, an aneurysm is said to occur when the dilatation exceeds more than 50% of the normal diameter Aneurysms may be classified according to their gross

---

[3] Copyright ©2010, A.D.A.M., Inc.
Available at `http://www.ncbi.nlm.nih.gov/bookshelf/br.fcgi?book=adam&part=A000162`.

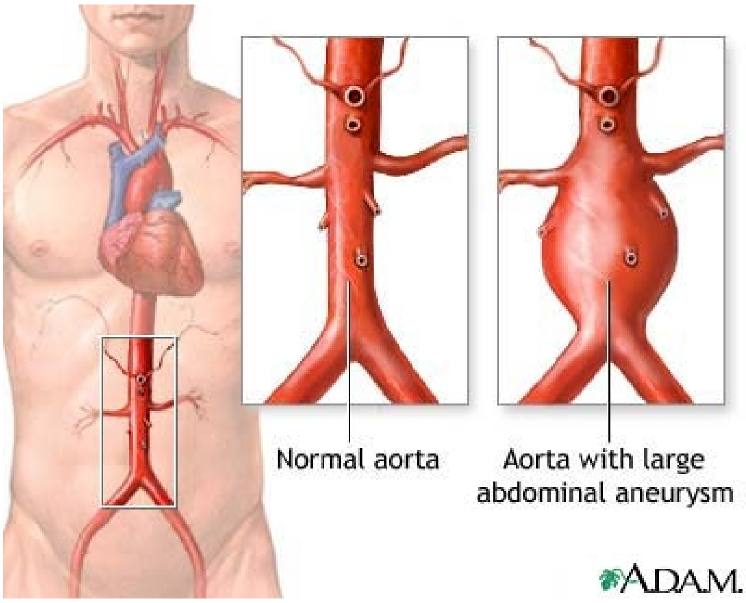

Figure 2.4.: Abdominal Aortic Aneurysm (AAA)

appearance [24] (see Fig. 2.5[4]). A *fusiform aneurysm* affects the entire circumference of a segment of the vessel, resulting in a diffusely dilated artery. In contrast, a *saccular aneurysm* involves only a portion of the circumference, resulting in an outpouching of the vessel wall. The third shape shown in Fig. 2.5 is a *ruptured aneurysm* that has burst and caused bleeding into the surrounding tissues. Aortic aneurysms are further classified according to their location within the aorta, *thoracic aortic aneurysm* (TAA) or *abdominal aortic aneurysm* (AAA). As this thesis focuses on AAA, we will limit the following definitions and etiology to this type of aortic aneurysm.

AAAs result from conditions that cause degradation or abnormal production of the aortic wall's structural components, elastin and collagen. The causes may be broadly categorized as degenerative diseases, inherited or developmental diseases, and trauma. The most common pathologic condition associated with degenerative aneurysms is *atherosclerosis*. Many patients with AAAs have coexisting risk factors or even *atherosclerosis* in oder blood vessels. Inflammation and biomechanical wall stress contribute to the degenerative process that characterize most AAAs.

AAAs occur more frequently in males than in females, and the incidence increases with age. The disease is the tenth leading cause of death in men 65 to 75 years [135]. 12 to 19 percent of first-degree relatives, predominantly men, of a patient with an AAA will develop an aneurysm [68] indicating also a genetic coherence.

---

[4] From The Internet Encyclopedia of Science, Health & Disease.
Available at `http://www.daviddarling.info/encyclopedia/A/aneurysm.html`.

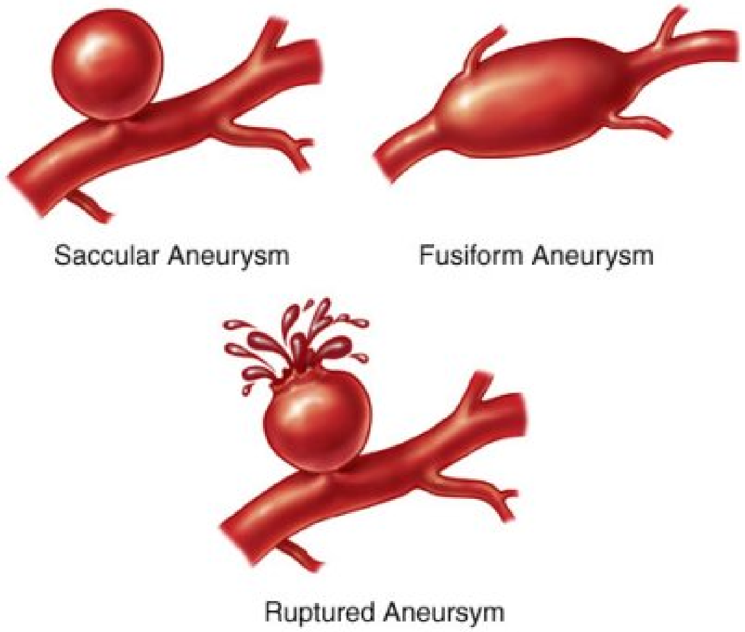

Figure 2.5.: Gross appearances of aneurysms

2.3.2. Diagnosis

Symptomatic AAAs usually involve hypogastrium or lower back pain that is steady and gnawing and lasts hours to days [68]. Hypotension is another common symptom. However, most AAAs are asymptomatic and are often first detected on an imaging study ordered for other indications. Doctors may feel a pulsatile abdominal mass and can usually hear a whooshing sound (bruit) caused by turbulence as blood rushes past the aneurysm [135]. However, the size of an aneurysm tends to be overestimated on physical examination and even normal aortas may sometimes feel enlarged [68].

Different imaging devices can be used to visualize and diagnose AAAs. A more complete description of each of these techniques is given in section 2.1. Abdominal US has a sensitivity and specificity approaching 96% for the detection of AAA and is therefore frequently used to screen for the presence of AAA [135]. CTA of the abdomen can determine the size and shape of an aneurysm more accurately than US but exposes the person to radiation. Yet it is widely used by physicians, as it's precise enough to allow different measurements for surgery planning. *Magnetic Resonance Angiography* (MRA) is also accurate but may not be available as quickly as US or CTA. Recent studies [118, 75] have suggested a combination of PET and CT, namely PET-CT, in order to visualize inflammation within the aneurysm wall. It has been claimed that increased cell activity inside the AAA indicates instability of the wall increasing the rupture risk. However, so far, it has not been given enough evidence to include PET-CT acquisitions into official guidelines for AAA diagnostic and treatment.

2.3.3. Treatment

The major risk posed by an abdominal aortic aneurysm is rupture and its high associated mortality. Fillinger et al. [43] performed a large trial of patients with ruptured aneurysms. In their conclusions 25% died before reaching a hospital, another 51% percent died at the hospital without undergoing surgery, and of the those who had surgery, the operative mortality was 46%, yielding an overall 30-day survival of just 11%.

There are basically three treatment options for an AAA depending on various factors like the shape and stadium of the aneurysm and the age and general health condition of the patient.

Mechanical intervention is currently the only treatment shown to be effective in preventing AAA rupture and aneurysm-related death; it is reserved for AAA $\geq$5.5 cm in diameter for men and $\geq$5.0 cm in women [4]. Treatment using open surgical repair involves opening the body with a large cut (incision) into the abdomen. The damaged area is separated surgically from the vessel and replaced with a synthetic tube called (aortic) graft. It is quite a massive intervention that is performed under general anesthesia involving cardiopulmonary bypass (CPB) via a heart-lung machine, and takes about 3 to 4 hours. It usually requires the patient to stay for 3 days in an intensive care unit and remain in hospital for 7 to 10 days. Thus, recovery time is typically about a week but it can be as high as three months bearing risks due to anesthesia and the large incision (like infection, etc.). However, it is a good option for a long-term success as the damaged area is completely removed.

Although surgical repair is the preferred treatment, it is not applicable to the care of patients with smaller aneurysms or those with medical contraindications to surgery. Here β-blocker therapy is considered important for reducing the risk of AAA expansion and rupture [47]. This should be accompanied by an appropriate risk factor modification such as control of hypercholesterolemia and hypertension and discontinuation of cigarette smoking. Small aneurysms should be followed up with periodic surveillance imaging to monitor their size.

A third treatment option is endovascular repair which was developed to reduce the risks associated with open surgery and to provide a treatment option for patients who are not deemed to be surgical candidates. As this work is centered around endovascular aortic repair, we will give a more detailed description of the procedure in chapter 4.1.

3. Technical Principles

This thesis aims at presenting novel computer assistance techniques for the treatment of AAAs. However, before coming to the details, we first need to introduce some basic concepts of medical image processing starting with the image itself and passing on to image segmentation and registration techniques. In the end of this chapter, we also present the concept of disocclusion that is rather related to computer vision than to medical imaging. These four sections provide the methodological basis for the review of state of the art procedures (Part II) and the novel methods presented in Part III.

3.1. Images

This thesis is concerned with *(digital) images* and some special kinds of their processing. This section introduces our representation of images and presents some of the notations used in the remainder of this thesis.

When creating an image with an acquisition system, i.e. a simple viewing camera, light enters the camera lens and hits the image plane. In a typical Charged Coupled Device (CCD) camera, the physical image plane consists of a rectangular grid of $m \times n$ small black *photosensors*. These are sensitive to light and convert light energy in continuously varying electrical signals representing the light intensity. An image I is defined as a continuous n-dimensional light intensity function $I : \Omega \longrightarrow \mathbb{R}$ ($\Omega \subset \mathbb{R}^n$) that maps a spatial location to a scalar value representing brightness intensity.

In order to save an image in an electronic system, the continuous electrical signal has to be discretized both in its spatial location on the image (*sampling*) as well as in its value (*quantization*). This procedure is called *digitalization* rasterizing an image, i.e. spatial locations are distributed on a regular grid. The grid points are referred to as pixels ($n = 2$) or voxels ($n \geq 3$). In general, medical images are of dimension 2, $2 + t$, 3, $3 + t$ depending on the imaging modality and acquisition mode (single image, sequence of frames). For the remainder of this thesis, we will restrict the possible dimension of images to $n = \{2, 3\}$ according to the images acquired during the entire process of EVAR.

The *histogram* of a digital image with gray-levels in the range $[0, L-1]$, is the graphical presentation of a discrete function $h(i_k) = n_k$, where i_k is the kth gray level in $[0, L-1]$ and n_k is the number of pixels in the image with intensity i_k. The histogram can be effectively used for image enhancement and for segmentation.

Images can be derived to extract the gradient information of the underlying intensity-mapping function. Given an image I, we will denote the gradient $\nabla I =$

$\frac{\partial I}{\partial \mathbf{x}}$.

3.2. Medical Image Segmentation

Image segmentation is the grouping of image pixels, with in some way resembling characteristics, into meaningful and usually connected structures, such as curves (edges) or regions, according to a given set of rules [111]. It can be formally explained as the partitioning of the image domain $\Omega \subset \mathbb{R}^n$ into homogeneous regions $\Omega_1, \Omega_2, \ldots, \Omega_l \subset \Omega$ such that

$$\Omega = \bigcup_{i=1}^{l} \Omega_i \tag{3.1}$$

The objective of a segmentation is the recognition of objects and their distinction from the background.

In the following sections, we will describe three main types of segmentation methods commonly used for medical applications.

3.2.1. Algorithms on Pixel Level

Pixel based segmentation techniques are the simplest of all segmentation approaches. For the distinction and definition of different regions, the gray values in the image are observed and typical values or intervals for each structure are determined.

Thresholding

Thresholding segmentation approaches are based on the investigation of the histogram of the image. If the object for detection is clearly separated from the background, then the histogram of the image has at least two dominant distributions of intensities and thus two local maxima. Traditionally, one obvious way to extract the object from the background is to select an intensity threshold value T, which separates the two maxima, e.g. a local minimum between them. The segmentation is then accomplished by scanning the image pixel by pixel and defining each pixel, depending on its intensity value in comparison to the threshold, as object or background. Instead of just choosing one intensity value, two thresholds can be selected defining a range of intensity values. This might be suitable for images showing a more complex intensity distribution with more than two histogram peaks which is the case for most medical images.

Although this method is fast and simple, it suffers from several drawbacks. The thresholds for interesting regions highly depend on the image quality and might change from an image to another showing the same scene. Also, this technique assumes that the region to be detected, has a different intensity distribution than its background, which is not the case in particular for medical images. Eventually, this method works on pixel intensities only and does not take into account any connectivity information. Therefore, it is very sensitive to outliers.

Region Growing

Compared to the thresholding approach described above, this method additionally uses connectivity information. It starts with a seed point and merge homogeneous neighbors into the region. The crucial criterion is the homogeneity definition for which several definitions may be used:

- The neighboring pixel value is inside a previously fixed range of intensity values.
- The difference between the intensities of a new pixel and its neighbor, which is part of the region, is lower than some previously fixed threshold.
- The new pixel intensity is inside the intensity distribution of the entire region to be segmented. The expansion of the region is also dependent on the neighborhood definition.

A neighborhood can be 4 or 8 pixels around the center pixel in 2D; 6, 18 or 26 voxels in 3D.

The advantage of this technique is that it uses an intensity criterion to decide if a pixel belongs to the model and a connectivity criterion to be sure that a possible new pixel is connected with the seed. However, there is no constraint on the shape of the region and if no suitable intensity borders are available, the region might expand to infinity.

Edge Based Segmentation

The aim of an edge based segmentation is to determine the boundaries of interesting objects by detecting image edges.

The first and second derivatives of the image function give information about locations of edges in an image. The first derivative is zero in areas of constant gray level values and non-zero in areas where the values are no longer continuous. It forms a maximum where the image function changes from a low to a high intensity value (from dark to light) and a minimum at the opposite situation. The second derivative has a zero crossing at places where the first derivative has its extrema.

Canny edge detector [17] is the current standard edge detection scheme. It is described as the first order derivative of a Gaussian filter and consists of four processing steps. The first step is to filter out the noise in the original image, by applying a Gaussian filter. Then, the gradient of the smoothed image is calculated to detect edges in x and y direction respectively. In order to normalize the width of all edges to be only one pixel, nonmaxima suppression is applied for suppressing high values of the gradient magnitude. The last step consists of thresholding the nonmaxima suppressed magnitude image in order to reduce the number of false edge fragments.

3.2.2. Active Contours

The main idea of the *Active Contours* approach is that the boundary between the targeted object and its background is considered as a deformable model. After defining an initial contour, it is evolved towards an optimal shape and position ideally detecting the object to be segmented. Classified into different representations for the contour model, there are basically two main approaches that will be explained in the following sections.

Explicit Active Contours

Since its introduction in the late 1980s [71], various names, such as snakes, balloons, and parametric deformable contours or surfaces, have been used in the literature to refer to *Explicit Active Contours* or *Surfaces*. Here, curves and surfaces are represented explicitly by parameters, i.e. positions of the contour points. In 2D, a possible representation of curve is $C(s) = (x(s), y(s))$ moving through the spatial domain of an image.

During deformation, the points of the contour are moved by applying either an energy minimizing formulation and a dynamic force formulation [142]. We can formulate the energy function as

$$\begin{aligned} E(C(s)) &= E_{int}(C(s)) + E_{ext}(C(s)) && (3.2) \\ &= \frac{1}{2}\int_0^1 \alpha(s)|C'(s)|^2 + \beta(s)|C''(s)|^2 ds + \int_0^1 P(C(s))ds && (3.3) \end{aligned}$$

where $C'(s), C''(s)$ denote the first and second order derivative of the curve. The internal energy E_{int} specifies the tension or the smoothness of the contour. Here, the first-order derivative discourages stretching and makes the model behave like an elastic string, whereas the second-order derivative discourages bending and makes the model behave like a rigid rod. The weighting parameters α, β can be used to control the strength of the model tension and rigidity. The external energy E_{ext} is defined over the image domain and computed by integrating a potential energy function $P(x, y)$ along the curve $C(s)$. A typical potential energy function is designed to lead a deformable contour toward step edges. It is also possible to add other terms to force the expansion or shrinking of the model. A nearly complete collection of efficient energy formulations for *Explicit Active Contours* can be found in [69].

Although *Explicit Active Contours* have been applied successfully in a wide range of applications, they have several limitations [25]. In cases where the deformation has to cover a large change in size, the contour has to be reparameterized dynamically which increases computation time in particular for 3D applications. *Explicit Active Contours* is known to be quite sensitive to the initialization and get stuck in undesired local minima especially in medical images. Also the extension to other segmentation criteria such as color, texture, or motion is not straight-forward. Furthermore, the parametric approach has difficulty dealing with topological adaptation such as splitting or merging model parts, a useful feature for the detection of multiple objects or objects of unknown topology.

Implicit Active Contours

First introduced in the early 1990's [20, 91], *Implicit Active Contours* soon got ahead of the explicit formulation for many segmentation tasks within the medical field. Its major advantage is the ability to automatically handle topological changes and removing the issues of contour parameterization [25]. This is accomplished by employing curve evolution theory and the level set method for front propagation.

The purpose of curve evolution theory is to use only geometric measures such as the unit normal and curvature for contour deformation [142]. Let us again consider a moving curve $C(s,t) = (x(s,t), y(s,t))$, now with an additional parameter t for denoting the time step. Denoting its inward unit normal as N and its curvature as κ, the evolution of the curve along its normal direction can be characterized by the following partial differential equation:

$$\frac{\partial C}{\partial t} = F(\kappa)N \tag{3.4}$$

with $F(\kappa)$ determining the speed of the evolution. The basic idea of *Implicit Active Contours* is to couple the speed of deformation with the image data, so that the evolution of the curve stops at object boundaries.

The evolution is implemented using the level set method first brought up by Osher and Sethian [104, 123]. The propagation of a contour is achieved by evolving a time-dependent embedding function $\phi(x, y, t)$, the *so-called level set function*. Having the curve $C(s,t)$ as zero level leads to $\phi\left(C(s,t), t\right) = 0$. Deriving this with respect to time parameter t gives

$$\frac{\partial \phi}{\partial t} + \nabla\phi \frac{\partial C}{\partial t} = 0 \tag{3.5}$$

Inserting the definition of the normal $N = \frac{\nabla\phi}{|\nabla\phi|}$ and Equ. 3.4, it can be rewritten as

$$\frac{\partial \phi}{\partial t} = F(\kappa)|\nabla\phi| \tag{3.6}$$

The inclusion of image data is accomplished by the selection of speed function $F(\kappa)$. A possible solution for objects that have good contrast, is to include image gradient information [20, 91]:

$$F(\kappa) = \frac{1}{1 + |\nabla G_\sigma * I|}(\kappa + F_0) \tag{3.7}$$

where $G_\sigma * I$ denotes the image I convolved with a Gaussian smoothing filter. However, in particular medical images lack sufficient contrast so that intensive research has been done on the formulation on suitable speed functions [88, 89, 22, 25, 147].

3.2.3. Active Shape Models

Instead of using a random initialization of the curve as suggested in the previous sections, *Active Shape Models* (ASMs) allow the integration of a priori knowledge about the shape to be segmented and its gray-level appearance in the image. Consequently, training with many examples is required in order to acquire a shape model (with its variability) and the gray-level appearance (with its variability).

In its most popular implementation [23], a statistical model of the shape and its variations is created by a training set of shapes represented by landmark points. It is given by the principal components of vectors of landmark points. The gray-level appearance model is limited to the border of the object and consists of the normalized first derivative of profiles centered at each landmark that run perpendicular to the object contour. The cost (or energy) function to be minimized is the Mahalanobis distance of these first derivative profiles. The fitting procedure is an alternation of landmark displacements and model fitting in a multiresolution framework.

3.3. Medical Image Registration

The goal of *Image Registration* is to accurately relate information of two or more images [61]. In the case of *Medical Image Registration* the focus is laid on medical images, i.e. acquired by the modalities described within section 2.1. Due to the great variety of registration problems and different algorithms to solve them, there have been some attempts in the literature to categorize registration algorithms, the most thorough and promising was given by [90]. According to their classification, this thesis concerns the problem of multimodal intrasubject registration of the abdomen. The modalities involved are CT and interventional C-arm acquiring 2D and 3D image data and thereby defining a registration paradigm for rigid 3D-3D and projective 2D-3D transformations. Our paradigm is further constrained by an intrinsic registration basis relying only on patient generated image content without the need for any extrinsic markers such as fiducials. We will constrain the general description and review of registration algorithms of the following sections to our defined paradigm.

3.3.1. General Formulation

Given two images I^M and I^F denoted as moving and fixed image, *image registration* describes the problem of estimating the optimal transformation $\hat{\mathbf{T}}$ of I^M such that it perfectly aligns with I^F in terms of a certain energy $\mathcal{E}$:

$$\hat{\mathbf{T}} = \arg\min_{\mathbf{T}} \mathcal{E}(I^F, \mathbf{T} \circ I^M) \tag{3.8}$$

In the case of 3D-3D registration, the domains of both images are three-dimensional ($\Omega^M \subset \mathbb{R}^3, \Omega^F \subset \mathbb{R}^3$) whereas for 2D-3D registration, the 3D volume is set to be the moving image ($\Omega^M \subset \mathbb{R}^3$) and the 2D image is fixed ($\Omega^F \subset \mathbb{R}^2$).

In Equ. (3.8), operation $\circ$ represents the application of $\mathbf{T}$ on image I^M. Practically, this is realized by *interpolation*, in particular by two contrary approaches (see Fig. 3.1). During *backward warping*, the application algorithms cycles through the old image, applies the transformation to every single pixel, and creates a warped image

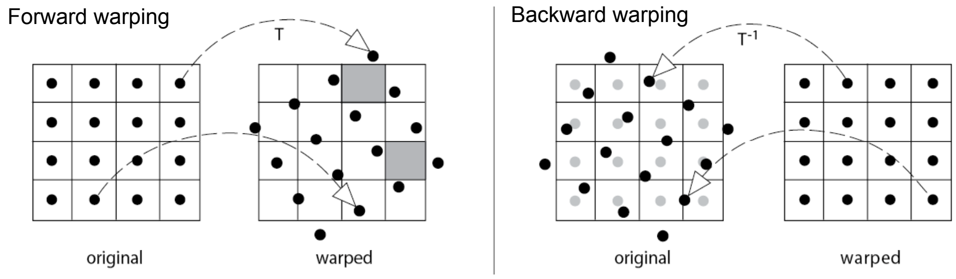

Figure 3.1.: Concept of *forward* and *backward warping*

from the resulting positions. In the contrary procedure, *forward warping*, an empty target image is created first where the cycle is performed on.

In the following sections, we will explain the details of the registration paradigm given by Equ. (3.8).

3.3.2. Transformations

The choice of transformation $\mathbf{T}$ is defined by the given registration problem and also directly related to the imaging modalities involved. In general, one can distinguish four types of different transformation classes each of which is explained for the 2D and 3D case in the following subsections.

Rigid Transformation

A rigid transformation

$$\mathbf{T}_{\text{rigid}} = \begin{bmatrix} s\mathbf{R} & \mathbf{t} \\ \mathbf{0} & 1 \end{bmatrix} \tag{3.9}$$

is a composition of rotation $\mathbf{R}$, translation $\mathbf{t}$, and an isotropic scaling factor s. In order to specify the transformation in 2D, the angle of rotation (r), the value of translation in x and y direction (t_x, t_y) as well as the scaling factor s must be given. The literature therefore refers to it as 4 degree of freedom (4-DOF) $\mathbf{T}_{\text{rigid}}$ whereas the 3D matrix is named as 9-DOF as it includes three values for scaling (s_x, s_y, s_z), rotation angles (r_x, r_y, r_z)), and translation (t_x, t_y, t_z) for the three image dimensions.

Affine Transformation

An affine transformation

$$\mathbf{T}_{\text{affine}} = \begin{bmatrix} \mathbf{A} & \mathbf{t} \\ \mathbf{0} & 1 \end{bmatrix} \tag{3.10}$$

is a non-singular linear transformation $\mathbf{A}$ followed by a translation $\mathbf{t}$. In 2D, the affine matrix $\mathbf{A}$ can be decomposed to

$$\mathbf{A} = \mathbf{R}(\theta)\mathbf{R}(-\phi) \begin{pmatrix} s_1 & 0 \\ 0 & s_2 \end{pmatrix} \mathbf{R}(\phi) \tag{3.11}$$

to be the concatenation of a rotation (by ϕ), a non-isotropic scaling by s_1 and s_2 respectively in the (rotated) x and y directions, a rotation back (by $-\phi$), and finally another rotation (by θ) [58]. The 2D $\mathbf{T}_{\text{affine}}$ therefore forms a 6-DOF transformation matrix whereas the 3D case captures 12-DOF.

Projective Transformation

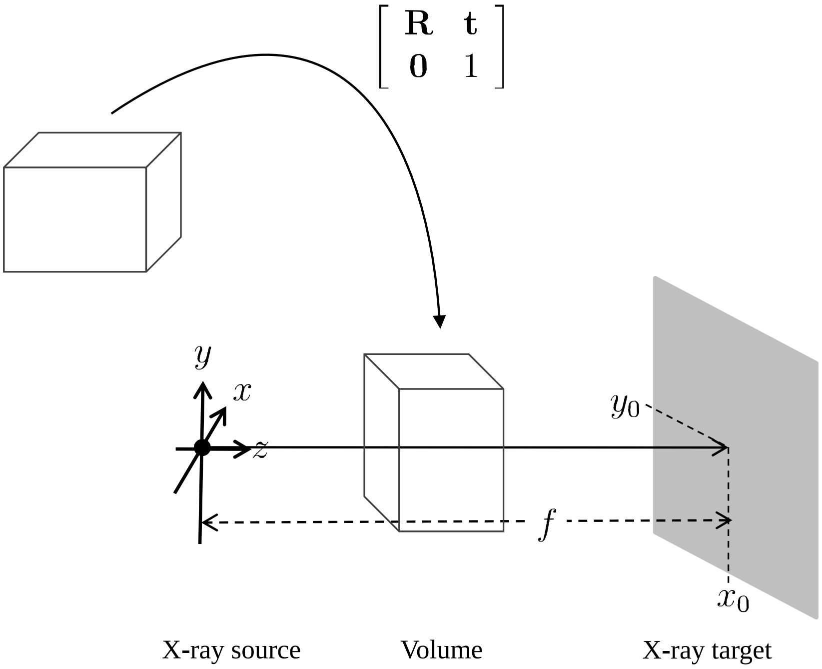

Figure 3.2.: The concept of perspective projection following the description of [58]

In the sense of medical image registration, projections are mostly employed in 2D-3D registration algorithms to describe the geometric mapping from locations in 3D onto the 2D view. The projection transformation

$$\mathbf{T}_{\text{projective}} = \mathbf{K} \begin{bmatrix} s\mathbf{R} & \mathbf{t} \\ \mathbf{0} & 1 \end{bmatrix} \tag{3.12}$$

consists of the 6-DOF extrinsic parameters $[\mathbf{R}|\mathbf{t}]$ for rotation and translation of a 3D volume and additional 4-DOF intrinsic imaging parameters

$$\mathbf{K} = \begin{pmatrix} \alpha_x & 0 & x_0 \\ 0 & \alpha_y & y_0 \\ 0 & 0 & 1 \end{pmatrix} \tag{3.13}$$

of the pinhole projection model [58] with focal length in x- and y-dimensions $\alpha_x = \frac{f}{s_x}, \alpha_y = \frac{f}{s_y}$ (s_x, s_y is the respective size of a pixel in the target X-ray) and principal point (x_0, y_0). The concept of perspective projection is visualized in Fig. 3.2.

In practical implementations of 2D-3D registration paradigms involving CT volumes and 2D X-ray images, a projective transformation is nowadays realized through the concept of *Digitally Reconstructed Radiographs* (DRR). Thereby, a synthetic X-ray image is computed by casting virtual rays through the 3D CT volume and calculating the X-ray attenuation along each ray. This process is called *volume rendering*. DRRs were first introduced for 3D treatment planning in radiation therapy [126], but soon became an interesting input for the realization of 2D-3D registration algorithms. However, DRRs are computationally expensive to create, and their required iterative generation typically creates a bottleneck in the execution of the registration process. For a volume of size $N \times N \times N$, most volume rendering techniques, such as ray casting [83], splatting [10, 11], and shear-warp [76], have $\mathcal{O}(N^3)$ time complexity. Light-field methods reduce this time complexity by pre-computing some projection values and then interpolating the latter to generate DRR [121], but they require large memory to store the pre-projection values. Monte Carlo volume rendering [84] is a very efficient technique for producing DRRs from large medical datasets since the involved projection process is independent of the volume size and only related to the number of samples. However, their convergence rate is slow. Because of the increasing performance of Graphics Processing Units (GPUs) in the last couple of decades, the GPU has become an attractive target for DRR generation and image registration algorithms [80, 72, 146].

Deformable Transformation

For many medical applications, rigid transformations are not sufficient to meaningfully align two images. In particular soft tissue deforms in arbitrary ways caused by breathing, organ specific motion, or medical instruments.

Compared to the transformations explained previously, a deformation can not be represented as a matrix. Instead, one has to describe the motion for every individual pixel between two images. This is widely realized by a *displacement field*

$$\mathbf{u} : \Omega \longrightarrow \mathbb{R}^n \qquad \text{(here } n = 2, 3) \tag{3.14}$$

defined on the image domain $\Omega \subset \mathbb{R}^n$.

Substituting transformation $\mathbf{T}$ by displacement field $\mathbf{u}$, Equ. (3.8) can be rewritten as

$$\hat{\mathbf{u}} = \arg\min_{\mathbf{u}} \mathcal{E}(I^F, \mathbf{u} \circ I^M) \tag{3.15}$$

3.3.3. Energy Function

Intrinsic image registration paradigms employ energy functions $\mathcal{E}$ that include image information only [90]. This image content can be presented as the original intensity gray values (*intensity-based registration*), or a limited set of anatomical landmark or feature points (*feature-based registration*). It is not within the focus of this thesis to capture the entire variety of different energy functions used for image registration. Therefore, we restrict the following classification to the most popular measures and those that will be used in the remainder of this thesis.

Intensity-based

Intensity-based techniques use the intensity mapping of the images to define a *similarity measure*. Therefore, one image must be transformed together with its intensities in order to create an overlapping region with the other image where correspondency is assumed to exist at every pixel location. The similarity measure then calculates the quality of fit given this correspondency induced by transformation $\mathbf{T}$. In the following we will present the most commonly used intensity-based measures and will explain their mathematical notation on sample images $I, J \in \{\mathbb{R}^2, \mathbb{R}^3\}$. The overlapping region $\Omega_I \cap \Omega_J$ is discretized in N pixels (if $\Omega_I, \Omega_J \subset \mathbb{R}^2$) or voxels (if $\Omega_I, \Omega_J \subset \mathbb{R}^3$).

Difference-based Measures. Measures such as *Sum of Absolute Differences*

$$\mathcal{SAD}(I, J) = \frac{1}{N} \sum_{i=1}^{N} |I(\mathbf{x}_i) - J(\mathbf{x}_i)| \tag{3.16}$$

and *Sum of Squared Differences*

$$\mathcal{SSD}(I, J) = \frac{1}{N} \sum_{i=1}^{N} (I(\mathbf{x}_i) - J(\mathbf{x}_i))^2 \tag{3.17}$$

, calculate the difference of intensity at each location. However, they make the implicit assumption that after registration, the images differ only by Gaussian noise [61].

Correlation-based Measures. By computing the statistical correlation of intensities, correlation-based measures are independent of linear intensity changes. This makes the measure very suitable for intra-modality registration. The most famous amongst these measures is *Normalized Cross Correlation* (sometimes also referred to as *Correlation Coefficient*)

$$\mathcal{NCC}(I, J) = \frac{\sum_{i=1}^{N} \left(I(\mathbf{x}_i) - \bar{I}\right) \left(J(\mathbf{x}_i) - \bar{J}\right)}{\sqrt{\sum_{i=1}^{N} \left(I(\mathbf{x}_i) - \bar{I}\right)^2} \sqrt{\sum_{i=1}^{N} \left(J(\mathbf{x}_i) - \bar{J}\right)^2}} \tag{3.18}$$

where $\bar{I}, \bar{J}$ denote the mean intensity values of images I, J. A related measure that uses image gradient values instead of image intensities is *Gradient Correlation*. Here, $\mathcal{NCC}$ is calculated between gradients of I, J in each single component respectively. The final value of this measure is the average of these normalized cross correlations. The formula for the 2D case ($\Omega^I, \Omega^J \subset \mathbb{R}^2$) is given by

$$\mathcal{GC}(I, J) = \frac{1}{2} \left(\mathcal{NCC}\left(\frac{dI}{dx}, \frac{dJ}{dx}\right) + \mathcal{NCC}\left(\frac{dI}{dy}, \frac{dJ}{dy}\right) \right) \tag{3.19}$$

In the 3D case ($\Omega^I, \Omega^J \subset \mathbb{R}^3$), $\mathcal{NCC}$ is additionally computed in the third component of the image gradients leading to

$$\mathcal{GC}(I, J) = \frac{1}{3} \left(\mathcal{NCC}\left(\frac{dI}{dx}, \frac{dJ}{dx}\right) + \mathcal{NCC}\left(\frac{dI}{dy}, \frac{dJ}{dy}\right) + \mathcal{NCC}\left(\frac{dI}{dz}, \frac{dJ}{dz}\right) \right) \tag{3.20}$$

Information-theoretic Measures. These measures determine the amount of shared information in the two images and are particularly suitable for inter-modality registration. The idea goes back to the famous Shannon-Wiener entropy developed in communication theory in the 1940s [124]. Transferring the entropy to images, information included in one image I can be measured by

$$\mathcal{H}(I) = -\sum_i P(I = i) \log P(I = i). \tag{3.21}$$

Here, image I is treated as random variable and $P(I = i)$ gives the probability of intensity i within image I. One can easily see that the value of Equ.(3.21) will be zero if there is just one constant intensity in the images. On the other hand, the maximum entropy is obtained if every intensity is equally likely to occur. A common application of the entropy measure for registering images I, J is *Mutual Information*

$$\mathcal{MI}(I, J) = H(I) + H(J) - H(I, J) \tag{3.22}$$

using the *Joint Entropy* of images

$$\mathcal{H}(I, J) = -\sum_i \sum_j P(I = i, J = j) \log P(I = i, J = j) \tag{3.23}$$

with $P(I = i, J = j)$ being the probability of pairs of image values occurring together.

Regularization for Deformation. Displacement fields can represent any deformation, however, not all such deformations are anatomically plausible. Physical deformations typically obey certain rules, e.g. tissue stiffness, and sharp corners are not likely to occur. Therefore, an additional penalization term needs to be added to the intensity-based energy allowing, on the one hand, only plausible deformations and, on the other hand, decreasing the dimensionality of the optimization space.

$$\mathcal{E}(I^F, \mathbf{u} \circ I^M) = \mathcal{S}(I^F, \mathbf{u} \circ I^M) + \alpha \mathcal{R}(\mathbf{u}) \tag{3.24}$$

where $\mathcal{S}$ denotes one of the intensity-based similarity measures explained above, and $\mathcal{R}$ a regularization term. The positive scalar α controls the influence of the regularization terms. The most commonly used terms are *diffusion regularization*

$$\mathcal{R}_{\text{diffusion}}(\mathbf{u}) = \sum_{\mathbf{x} \in \Omega} ||\nabla \mathbf{u}_x(\mathbf{x})||^2 + ||\nabla \mathbf{u}_y(\mathbf{x})||^2 + ||\nabla \mathbf{u}_z(\mathbf{x})||^2 \tag{3.25}$$

penalizing harsh local displacements in x and y direction (if $\Omega \subset \mathbb{R}^2$) and z direction (if $\Omega \subset \mathbb{R}^3$).

Feature-based

Compared to the intensity-based measures that uses the entire image content to measure the quality of fit, feature-based methods usually minimize a *distance measure* accumulated over only a set of identified features or landmark points. It requires an additional step prior to the registration procedure to extract this information. Whereas anatomical landmarks are most commonly selected manually by the user itself, image features are extracted automatically. Most commonly, a binary image is created and either resulting surfaces or the extracted points are matched. The big drawback is that the registration accuracy is limited to the accuracy of the extraction step.

The most popular method for matching 3D shapes represented as a set of points, curves, surfaces, or volumes, is the *Iterative Closest Point* (ICP) method [7]. Whatever the original two shape representations, they are first converted to two set of points $M = \{\mathbf{m}_1, \dots, \mathbf{m}_{N_M}\}$ and $D = \{\mathbf{d}_1, \dots, \mathbf{d}_{N_D}\}$. In each iteration step, the algorithm selects the closest points as correspondences and calculates the transformation $\mathbf{T}$ for minimizing the equation

$$\mathcal{E}_{\text{ICP}}(\mathbf{T}) = \sum_{i=1}^{N_M} \sum_{j=1}^{N_D} w_{ij} ||\mathbf{m}_i - (\mathbf{T}\mathbf{d}_j)|| \tag{3.26}$$

where w_{ij} are the weights for a point match assigned as $w_{ij} = 1$ if $\mathbf{m}_i$ is the closest point to $\mathbf{d}_j$ and $w_{ij} = 0$ otherwise. As closeness measure, the Euclidean distance is used.

Another popular surface matching technique is the *head-and-hat* algorithm [106] where two equivalent surfaces are identified in the images. The first is represented as a stack of discs, and is referred to as the head, and the second surface is represented as a list of unconnected 3D points. The registration transformation is determined by iteratively transforming the (rigid) hat surface with respect to the head surface, until the closest fit of the hat onto the head is found. The measure of closeness of fit used is the squared distance between a point on the hat and the nearest point on the head, in the direction of the centroid of the head.

In particular for matching binary structures, the use of a distance transform has a direct impact on the performance of the registration algorithm. A distance transform of a binary image labels all pixels in this image with their distance from the surface of the object. In the *Chamfer Matching* [14] procedure the distance transform is computed by means of local distances. More recently, exact Euclidean distance transforms have been used in place of the chamfer transform [63].

3.3.4. Optimization

An optimization problem can be formulated as

$$\hat{\mathbf{x}} = \arg\min_{\mathbf{x}} F(\mathbf{x}) \tag{3.27}$$

with *costfunction* $F : \Omega \longrightarrow \mathbb{R}^n$. An optimization algorithm therefore aims at finding a parameter vector $\hat{\mathrm{x}}$ (*minimizer*) such that $\forall \mathbf{x} \in \Omega : F(\hat{\mathbf{x}}) \leq F(\mathbf{x})$. Likewise Equ. 3.27 can be formulated as a maximization where $\hat{\mathrm{x}}$ (*maximizer*) has to fulfill $F(\hat{\mathbf{x}}) \geq F(\mathbf{x}) \forall \mathbf{x} \in \Omega$. $\Omega \in \mathbb{R}^n$ defines the *search space* of the optimization algorithm. In medical image registration, F equals the energy $\mathcal{E}$, whose computation requires the traversal of possibly quite large images. Since it depends on the actual image content, this energy is in most cases highly non-linear. Therefore the class of optimization problems that can be applied to medical image registration problems is *unconstrained non-linear optimization*. The decision for a certain optimization algorithm affects mostly the computation speed, robustness and capture range of the registration algorithm. This work does not aim at presenting the whole range of different optimization algorithms and therefore we restrict the following description to the most popular used for medical image registration. For an almost complete review of optimization algorithms, we refer to [115].

Best Neighbor Search. This method (also called *Hill Climbing*) is probably the simplest optimization scheme. During each iteration, it evaluates a number of neighbors of the current parameter estimate and adopts the neighbor which yields the best cost function value, as the central estimate for the successive iteration. A popular strategy to select the neighbors is to just add and subtract a certain step size to every parameter separately. With n being the dimension of the search space of the costfunction, it results in $2n$ costfunction evaluations per iteration. If no better estimate is obtained, either the step size is reduced, or the algorithm terminates. Of course, this method needs a good initialization value since it is prone to fall into local minima.

Powell-Brent Direction Search. Starting at a given position in the parameter space, this algorithm minimizes the costfunction successively along certain directions [115]. Two problems arise thereby. Finding the best directions within the n-dimensional search space, and doing efficient line minimization on a new costfunction with only one parameter.

Powell's method [114] gives a solution to the first problem. The first set of directions are the individual unit directions of the search space themselves. After n line minimizations, a new first direction is established as the direction vector connecting the last and the current estimate. At the same time the direction of largest decrease is omitted so that, in the next iteration, line minimization can be performed in n directions.

The latter problem of realizing efficient line minimization on only one parameter was solved by Brent's method [16]. It uses both parabolic interpolation and golden section search, choosing dynamically in each step which one is more appropriate.

Downhill Simplex Method. A more advanced search strategy is the *Downhill Simplex* method [99]. In an n-dimensional space, a simplex represents a minimal geometric shape of $n + 1$ points which certain operations can be applied to in order to find a global optimum. A starting simplex is defined around the initial parameter estimate and the costfunction is evaluated at its corners. Depending on the results, the shape of the simplex is changed according to rules for reflection, expansion, and contraction in order to shrink, enlarge, or move the search region. If the region within the simplex falls below a defined threshold, the algorithm assumes to have found an optimum and returns the corner point of the simplex yielding the smallest costfunction value.

The biggest advantage of this method compared to the other search methods is that it uses the minimal number of evaluations that span the parameter space. Moreover, since the shape of the simplex is flexible in all dimensions, traveling through narrow regions can be performed much more efficiently.

Gradient Descent/Ascent Method. If the gradient of costfunction F is available, a very basic way to find an optimum is to analyze the gradient and to step successively in its direction:

$$\mathbf{x}_{i+1} = \mathbf{x}_i + \alpha \frac{dF(\mathbf{x}_i)}{d\mathbf{x}_i} \tag{3.28}$$

The *learning rate* α is a positive constant if we are seeking for a maximum (*Gradient Ascent*), and negative otherwise (*Gradient Descent*). Starting from an initial value for $\mathbf{x}_0$, the update of Equ. 3.28 is iterated until the norm of the gradient becomes too small. The *Steepest Descent/Ascent* method, an extension of the previous algorithm, conducts a line search along the direction of the gradient in order to find an optimal value for α.

3.3.5. Validation

Validation is a crucial part of the development process of intrinsic medical image registration algorithms. Besides qualitative visual assessment of the registration result by an expert, the accuracy of an algorithm should also be qualitatively analyzed in order to decide whether it is good enough for a particular clinical application, or to compare it to another algorithm [61]. Therefore a reference solution has to be created which the solution provided by the proposed algorithm can be compared to. As another important evaluation step, the robustness of the algorithm has to be shown. It analyzes the behavior of the method in special situations and measures how often it converges to the right solution when applied with different input, and how much disturbance can be introduced until the registration fails.

Reference Solution

For quantitative accuracy analysis, it is crucial to obtain parameters that represent the correct transformation between the images. This transformation is generally denoted as *Ground Truth* $\mathbf{T}_{gt}$. Such a transformation could be computed by a *Gold Standard* technique if it is available for the respective registration problem. The term refers to a known technique that computes a correct image alignment. This can be achieved by using invasive markers attached to the patients and running a point-based registration with known correspondences. Instead of placing invasive markers, another possibility is to manually determine corresponding anatomical landmarks.

Accuracy Measures

The accuracy of a registration algorithm is determined via the registration error and is usually varying over the image. With $\mathbf{T}$ being the calculated transformation and $Q = \{\mathbf{q}_i\}$ being a set of k points distributed over the entire volume extents, several error measures have been proposed:

mTRE. The *mean target registration error* [44] determines the 3D error to the ground truth transformation $\mathbf{T}_{gt}$:

$$mTRE(Q, \mathbf{T}_{gt}, \mathbf{T}_{reg}) = \frac{1}{k} \sum_{i=1}^{k} ||\mathbf{T}_{reg}\mathbf{q}_i - \mathbf{T}_{gold}\mathbf{q}_i||$$

For 2D-3D registration algorithms, however, it has been proven to be more suitable to use the *mean target registration error in the projection direction* [137] in order to assess the magnitude of $mTRE$ in the projection direction:

$$mTREproj(Q, \mathbf{T}_{gt}, \mathbf{T}_{reg}, \mathbf{n}_{proj}) = \frac{1}{k} \sum_{i=1}^{k} ||\mathbf{T}_{reg}\mathbf{q}_i - \mathbf{T}_{gt}\mathbf{q}_i \cdot \mathbf{n}_{proj}||$$

where $\mathbf{n}_{proj}$ is the normal to the projection plane.

mPD. The *mean projection distance* [137] determines the 2D error in the projection plane:

$$mPD(Q, \mathbf{P}_{gt}, \mathbf{P}_{reg}) = \frac{1}{k} \sum_{i=1}^{k} ||\mathbf{P}_{reg}\mathbf{q}_i - \mathbf{P}_{gt}\mathbf{q}_i||$$

This measure is more appropriate for 2D-3D registration evaluation as it directly includes the projective component of the registration.

mRPD. The *mean reprojection distance* [95] determines the registration error after reprojecting each point back into 3D:

$$\begin{aligned} mRPD(Q, &\mathbf{T}_{gt}, \mathbf{T}_{reg}) \\ &= \frac{1}{k} \sum_{i=1}^{k} ||D(L_i(source, \mathbf{T}_{reg}\mathbf{q}_i), \mathbf{T}_{gt}\mathbf{q}_i)|| \end{aligned}$$

where $D(L_i, \mathbf{T}_{gold}\mathbf{q}_i)$ is the minimum distance between the 3D point at gold standard position and a line L_i through the 3D point at registered position and the X-ray source.

Robustness

During robustness assessment, the registration algorithm is tested for reproducibility of correct results under different scenarios introducing disturbances. Usually this evaluation is performed in randomized studies, also called Monte Carlo simulations. A set of displacements from the Ground Truth transformation is created and new initial transformations are established which serve as input to the algorithm.

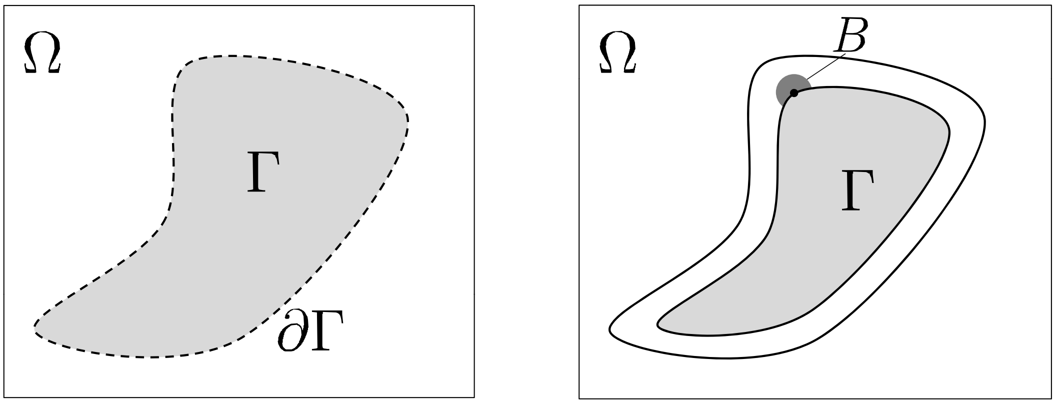

(a) (b)

Figure 3.3.: Visualization of Disocclusion Notation: (a) image domain Ω with occluded region Γ, (b) new state of Γ after a few iterations of the inpainting algorithm.

The displacements can be categorized into different ranges and the registration can be evaluated by the capture range which measures the biggest displacement from the Ground Truth where the algorithm is still successful. Usually success of a registration is given as a fixed threshold of the accuracy error function. The resulting distribution allows one to draw conclusions on the overall robustness, the number of outliers, and the performance in the individual transformation parameters. Often the mean and standard deviation of the individual transformation parameters are computed for studying the spatial behavior of the algorithm. For such an evaluation to be statistically meaningful, a large number of realistic clinical data sets of different patients has to be included. However, this has been rarely realized in the literature.

3.4. Disocclusion

In the computer vision community, the term *disocclusion* refers to the attempt of recovering scene information obstructed by visible parts[131]. Let $I : \Omega \longrightarrow \mathbb{R}$ define an image on a domain $\Omega \subset \mathbb{R}^2$. In the following, we denote by $\Gamma \subset \Omega$ the occluded image part and by $\partial\Gamma$ its boundary (see FIG. 3.3(a)). The aim of disocclusion is to reconstruct the intensity values $I(x_\Gamma, y_\Gamma)$ for all pixel positions $(x_\Gamma, x_\Gamma) \in \Gamma$ based on the image information which is available in the remaining part of the image domain $\Omega \setminus \Gamma$.

There have been several different approaches in the literature and Tauber et al.[131] gives an excellent overview. Two of the most promising approaches, *Digital Image Inpainting* [6] and *Poisson Image Editing* [108] are presented in the next two subsections.

3.4.1. Digital Inpainting

By imitating the process of expert inpainting for art restoration, *Digital Image Inpainting* [6] aims at reverting deterioration or at removing occluding elements from an image. Given the occluded image region, the solution is to transport image information along the isophotes, the direction normal to the image gradients, from $\Omega \setminus \Gamma$ into the occluded region Γ. Therefore, we compute an image function $\bar{I} : \Gamma \to \mathbb{R}$ such that $\bar{I}(x_\Gamma, y_\Gamma) = I(x_\Gamma, y_\Gamma)$ for all pixels $(x_\Gamma, y_\Gamma) \in \partial\Gamma$ on the boundary. The value in the interior Γ are, however, solution to a different partial differential equation:

$$\left\langle n(x_\Gamma, y_\Gamma), \nabla\bar{I}(x_\Gamma, y_\Gamma)\right\rangle = 0, \tag{3.29}$$

which is a stationary transport equation. The transport direction $n : \Gamma \to \mathbb{R}^2$ is thereby estimated based on the image information in a small neighborhood B around each pixel (x_Γ, y_Γ) in the already inpainted parts of Γ - see Fig. 3.3(b).

Bornemann and März[15] recently published a more efficient implementation of this inpainting method that is significantly faster while achieving high quality results at the same time.

3.4.2. Poisson Image Editing

The idea of *Poisson Image Editing* [108] is to achieve a reconstruction of the occluded region Γ via a certain *guidance field* $g : \Gamma \to \mathbb{R}^2$. Compared to *Digital Image Inpainting*, with this guided technique, it is possible to also bridge larger gaps in the image.

$$\min_{\bar{I}} \int_\Gamma \left\|\nabla\bar{I} - g\right\|_2^2 \, dx, \text{ subject to } \bar{I}|_{\partial\Gamma} = I|_{\partial\Gamma}. \tag{3.30}$$

Given such a *guidance-field* g, we are seeking for an image function $\bar{I}$ that is equal to I on the boundary of Γ and whose gradient is close, with respect to the L_2-norm, to the guidance field g. The solution of (7.6) can be computed by solving the Poisson equation

$$\Delta\bar{I}(x_\Gamma, y_\Gamma) = \operatorname{div}(g(x_\Gamma, y_\Gamma)), \qquad \forall(x_\Gamma, y_\Gamma) \in \Gamma. \tag{3.31}$$

This is the reason for naming this approach *Poisson Image Inpainting*. The reconstructed pixel values inside Γ can be then obtained by

$$I(x_\Gamma, y_\Gamma) = \bar{I}(x_\Gamma, y_\Gamma). \tag{3.32}$$

Part II.

State of the Art

4. Treatment of Abdominal Aortic Aneurysms

4.1. Endovascular Aortic Repair (EVAR)

In the last decade, EVAR has gained acceptance as an alternative to open surgical repair, with reduced risks. It provides substantial clinical benefit for the patient [60] such as decreased use of the intensive care unit, diminished length of hospital stay, and early return to normal activities [144]. Results of three European randomized trials [13, 54, 18] however indicate that the perioperative survival advantage with EVAR as compared with open repair is limited to the first two postoperative years. The long-term success rate of EVAR is still to be examined. Concerning ruptured AAAs, a recent study [50] shows that mortality may be improved with the use of endovascular repair (33% endovascular versus 41% open). Especially in patients 70 years or older, mortality after endovascular repair was lower than for open surgery (36% vs 47%).

For some patients, however, EVAR might not be the preferred treatment option. According to the German Society of Vascular Surgery and Vascular Medicine, measurements of the landing zones need to be within the following ranges: an aneurysm neck $\geq$ 15mm of length, a neck diameter $\leq$ 34mm, normal aortic wall without extensive calcification, moderate aortic kinking.

It is important to analyze the procedural steps of EVAR in detail in order to be able to integrate suitable computer assistance. In the next subsections, we present a description of its medical and imaging workflow and discuss the challenges physicians have to face.

4.1.1. Workflow

The implantation of an endovascular stent graft inside the aorta is a minimally-invasive procedure for the treatment of aortic aneurysms and aortic dissections. A descriptive visualization of the procedure is given in Fig. 4.1[1]. After the insertion of a pigtail catheter and guide wires, a shaft catheter including a folded stent graft is placed inside the aneurysm or dissection. Before unfolding the stent graft, the physician must ensure that branching vessels are not occluded. In this stage, misplacements of the stent graft can certainly lead to partial or total cut-offs of blood

---

[1] From Diseases and Conditions Index, National Heart Lung and Blood Institute, National Institute of Health, U.S. Department of Health & Human Services. Available at `http://www.nhlbi.nih.gov/health/dci/Diseases/arm/arm_treatments.html`.

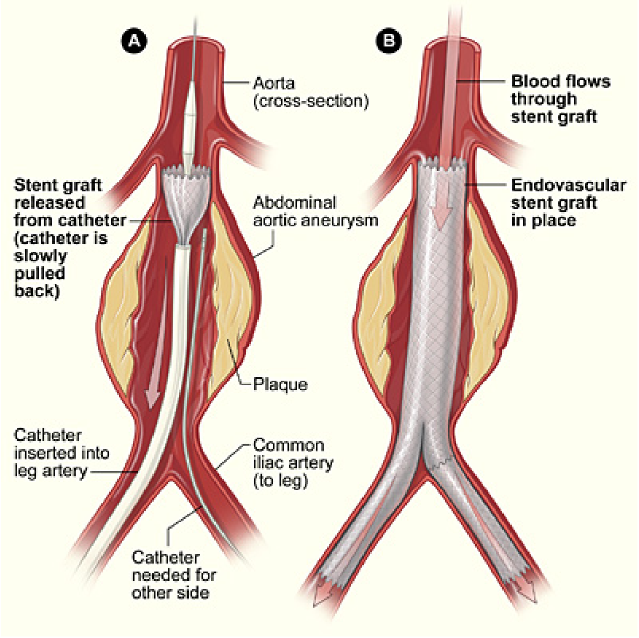

Figure 4.1.: Endovascular Aortic Repair (EVAR) in the abdomen

supply of vitally important organs. Another critical complication is presented by an *Endoleak* where blood still enters in between the stent graft and the aneurysm sac. It is evidence of incomplete exclusion of the aneurysm from the circulation and may be the result of an incomplete seal between the stent graft and the wall of the blood vessel or fabric defects or porosity [21].

The procedure is partitioned into three clinical phases [21], namely preoperative, intraoperative, and postoperative phase. Each of these phases will be described in detail in the following paragraphs.

Preoperative Phase

The insertion of a prosthesis inside the aneurysmatic aorta requires accurate treatment planning. Physicians need to carefully choose the appropriate stent graft from a variety of different models and producers, each of them being unique in material and shape.

Whereas knowledge about the diameter of the aneurysm, its relation to the renal arteries and extension in the iliac arteries used to be sufficient for conventional open treatment of AAAs, with the introduction of EVAR, additional information have become essential for adequate sizing of the stent graft to prevent endoleakage and unreliable stent fixation [1]. Important measurements include diameter, length and angulation of the proximal and distal landing zones, the distance from the lowest renal artery to the aortic bifurcation and to each iliac bifurcation, the diameter of the aortic bifurcation, presence of and location of thrombus in the AAA, quality of landing zones and potential access routes in terms of calcification or atheroma,

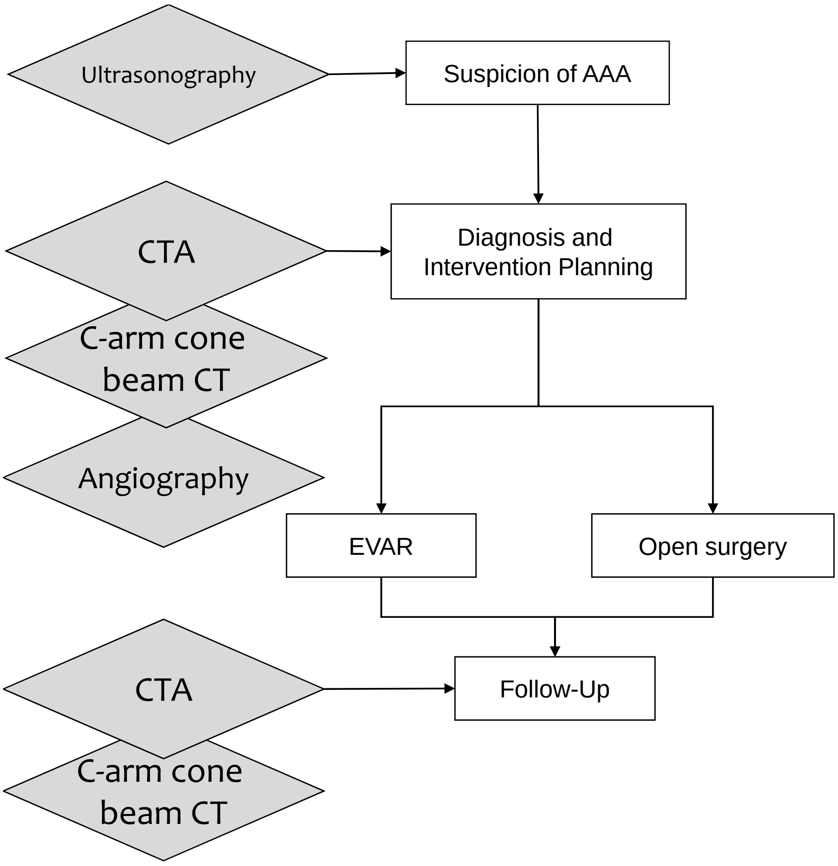

Figure 4.2.: Medical Workflow for AAA Diagnosis and Treatment

and presence of vascular anomalies (multiple renal arteries, early bifurcations, venous anomalies) [48]. Figure 4.4[2] shows a sample measurement form that is used by physicians to select the appropriate stent graft device.

Due to its unbeaten advantages in terms of resolution (see sections 2.1 and 2.3.2), most clinicians do the measurements in a CTA scan of the patient. Nowadays, angiography suites (detailed description in section 2.1.5) are equipped with modified stationary C-arms that are able to acquire CT-like slice images following the same main technical principles as CT. Although this new technology aims at improving the interventional situation by allowing 3D reconstructions during the intervention, recent studies [38, 101] have examined its feasibility also for preoperative scans. Although resulting images have lower contrast resolution than conventional CTA scans and artefacts are more likely to occur, it has been shown that radiologists are able to do accurate measurements. This could be timesaving in particular for acute cases, avoiding patient transfer to a CT laboratory.

If strong aortic kinking is present in the aneurysm region, it is very difficult to do exact length measurements in the CTA scan [119]. An insertion of the stent

---

[2] From Gore Medical. Available at `http://www.goremedical.com/resources/dam/assets/AN0444-EN3.pdf`.

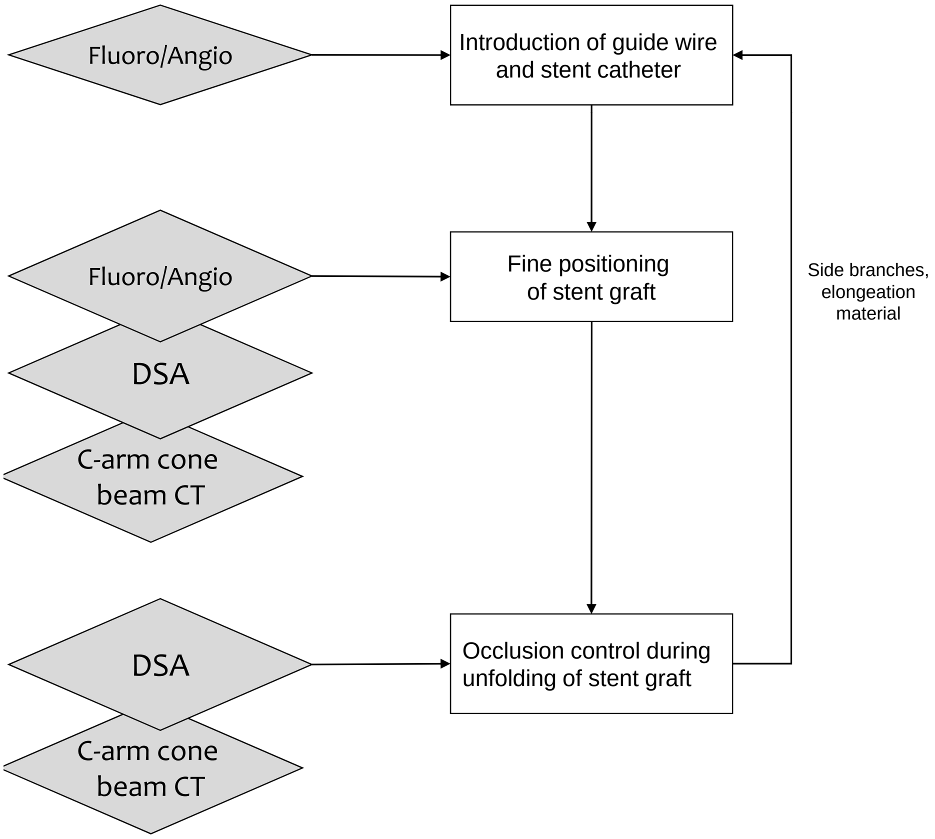

Figure 4.3.: Imaging Workflow for EVAR

graft causes a straightening of the aorta and a shift/spanning of the aneurysmatic mass. However, the extent of the straightening and the shift is not predictable. Some physicians perform an additional *Angiography* for more accurate measurements of the required stent graft length. Under alternating fluoroscopy and angiographic imaging, a thick catheter is inserted in the femoral artery and pushed through until it reaches the aneurysm. The catheter applies similar mechanical forces to the aortic wall as the stent graft and length measurements can thereby be done more accurately.

Intraoperative Phase

In the current clinical workflow, the intraoperative deployment of the stent graft into the aorta is performed via two-dimensional imaging only. Using either general anesthesia or regional anesthesia, one or both femoral arteries are exposed depending on the type of stent graft that is required. A needle followed by a guidewire is then placed in the femoral artery, and the guidewire is extended up the aorta under continuous fluoroscopy imaging. Then, an angiography or DSA sequence is acquired in order to provide a roadmap for placing the device. The graft catheter delivery system is passed up, over the guidewire, and positioned across

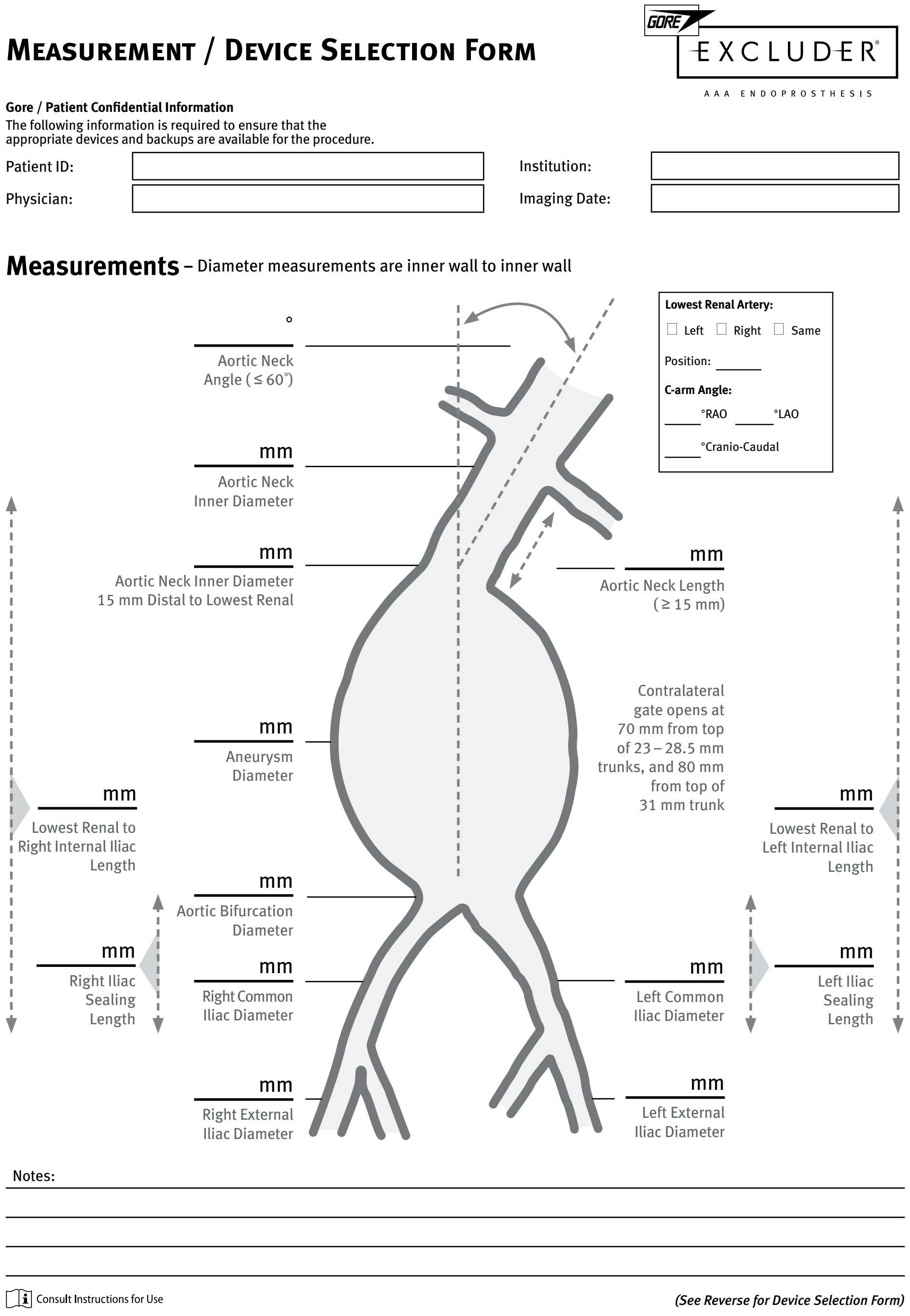

MEASUREMENT / DEVICE SELECTION FORM

GORE EXCLUDER®

AAA ENDOPROSTHESIS

Gore / Patient Confidential Information
The following information is required to ensure that the appropriate devices and backups are available for the procedure.

Patient ID: ☐ Institution: ☐

Physician: ☐ Imaging Date: ☐

Measurements – Diameter measurements are inner wall to inner wall

Lowest Renal Artery:
☐ Left ☐ Right ☐ Same
Position: ______
C-arm Angle:
_____°RAO _____°LAO
_____°Cranio-Caudal

_____° Aortic Neck Angle (≤ 60°)

_____ mm Aortic Neck Inner Diameter

_____ mm Aortic Neck Inner Diameter 15 mm Distal to Lowest Renal

_____ mm Aortic Neck Length (≥ 15 mm)

_____ mm Aneurysm Diameter

Contralateral gate opens at 70 mm from top of 23 – 28.5 mm trunks, and 80 mm from top of 31 mm trunk

_____ mm Lowest Renal to Right Internal Iliac Length

_____ mm Lowest Renal to Left Internal Iliac Length

_____ mm Aortic Bifurcation Diameter

_____ mm Right Iliac Sealing Length

_____ mm Right Common Iliac Diameter

_____ mm Left Common Iliac Diameter

_____ mm Left Iliac Sealing Length

_____ mm Right External Iliac Diameter

_____ mm Left External Iliac Diameter

Notes:

Consult Instructions for Use

(See Reverse for Device Selection Form)

Figure 4.4.: Sample measurement form for accurate stent graft selection

the aneurysm. Acquiring several angiography sequences from different view angles, the graft is deployed immediately below the renal arteries. A balloon within the catheter delivery system is then positioned across the attachment site and expanded in order to seat the hooks into the wall of the aorta. A completion angiography or DSA sequence is then obtained to make certain that the graft is properly seated and there is no evidence of flow between the graft and the aneurysm.

As conventional planar angiography cannot detect all graft-related anomalies, it has been suggested to use C-arm cone beam CT instead to ensure clinical success [9, 8, 38]. Although not evaluated in any clinical studies, medical imaging groups as well as the community of interventional radiologists try to push forward the intraoperative use of C-arm cone beam CT for navigation support and accurate stent positioning [12, 129]

Postoperative Phase

After stent graft insertion and deployment, physicians as well as radiologists need to repeatedly confirm the success of the treatment. Failures are generally classified in device-specific and morphologic complications [5]. Therefore, the goals of post-procedural imaging are to confirm the appropriate placement of the stent graft, to follow the long-term fate and size of the AAA sac, to detect remote stent graft failure (structural or functional), and to better characterize any endoleaks [48]. Available imaging modalities must hence allow the physician to systematically evaluate several parameters, including maximum aortic diameter, the neck and the length of the aneurysm, the presence of endoleaks, and stent configuration, during follow-up [52].

Again, similar to preoperative imaging, CTA is the modality of choice due to its high contrast resolution and the possibility it offers to correctly measure significant parameters. If an immediate treatment of occlusive complications is considered, interventionalists usually prefer on table imaging solutions avoiding patient transfer to a CT laboratory [39]. However, the suggested conventional planar angiography [48] does not detect all anomalies. Presenting a solution to this problem, recent studies [9, 8, 39, 38] document the beneficial use of angiography suites and possible on table C-arm cone beam CT reconstructions for acute cases.

4.1.2. Challenges

The entire interventional catheter navigation is done under 2D angiography imaging where the physician is missing the important 3D information. As the catheter and stent position is only visualized in 2D, more image acquisitions are needed during fine positioning of the stent graft before unfolding. This means an increase in radiation dose and used contrast agent at the same time as branching vessels need to be made visible in the images.

With the implementation of systems providing interventional C-arm cone beam CT reconstructions, the image information available for the interventionalist has been improved. However, such acquisitions produce an intense radiation exposure

[39] and are too time-consuming for constant application throughout the entire procedure. Normal size detectors of today's interventional angiographic imaging systems generally cover a field of 30 x 40 cm; a region that does not include enough information for difficult navigation tasks during abdominal aortic interventions [101].

Over the last years, treatment of complicated AAA using endovascular techniques has been approached demanding customized stent grafts with fenestrations or scallops [92, 56]. These treatment procedures incorporate an even higher risk of stentgraft-related complications such as occlusion of visceral arteries due to graft displacement and andoleaks. Disadvantages related to conventional intraoperative imaging modalities such as fluoroscopy and angiography, include prolonged procedure duration, poor visualization in some regions of the aorta, and navigational limitations.

4.2. Computer Assistance for EVAR

As already mentioned within the previous section, a thorough treatment planning is crucial for a successful outcome of EVAR. Measurements need to be done most accurately in order to define an appropriate stent graft in terms of model as well as size and diameter. When it comes to complex aneurysms degraded by severe aortic kinking or incorporating a highly calcified aneurysm thrombus, measurements need to include the thrombus that is very difficult to segment. Whereas the aortic lumen is highlighted by injected contrast agent and has strong gradient values to surrounding structures, the aortic wall and aneurysm thrombus are visually very hard to detect. More information on this topic as well as our solution to this problem is described in the Appendix B and C.

Addressing the problem of measuring the correct stent graft parameters, *virtual stenting* methods have been introduced for intracranial [82] as well as aortic [45, 37] stenting procedures in order to provide the physician with a preview of the selected device within a preoperative 3D scan of the patient. Due to the limited interaction possibilities provided to the physicians and radiologists when inspecting the preoperative patient scan, finding the correct parameters of the desired stent graft device is very difficult. In particular for patients suffering from kinking in the abdominal aorta, it is almost impossible to do accurate measurements. However, these solutions do not offer a visualization of the intraoperative situation compared to the preoperative definition. However, there is no interventional ground truth data available to validate these solutions for clinical application. In particular the involved biomechanical model of the stent graft is not extracted from real interventional scenarios but is defined based on approximated geometric models in their early research development phases. Besides, aortic stent devices are simulated by simplex meshes assuming the device to have a mesh-like structure [45, 37]. This is not given for abdominal aortic stent grafts, which are composed of a synthetic fabric tube, the *graft* (e.g. from woven polyester), supported by a rigid structure, and the *stent* (usually a metal web). In order to extract realistic behavior of abdominal aortic stent grafts, their geometric shapes need to be detected in interventional image series capturing the intravascular unfolding process.

The focus of this thesis is the presentation of methods for visualization enhancement during the EVAR intervention. The entire interventional catheter navigation is done under 2D angiography imaging where the physician is missing the important 3D information. As the catheter and stent position is only visualized in 2D, multiple additional image acquisitions are needed during fine positioning of the stent graft before unfolding. This means an increase in radiation dose and used contrast agent at the same time as branching vessels need to be made visible in the images. There have been several approaches published in the past, to overcome these drawbacks.

Imamura et al. [66] As a first solution, the authors present a system for registration of preoperative 3D-CTA and intraoperative fluoroscopic images during EVAR intervention. DRR images are generated by parallel voxel projection of 3D CTA after extracting an aorta region. By increasing/decreasing CT value in the aorta region of CTA, DRR with/without contrast media injection are obtained. Within their experimental setup, the authors investigate characteristics of several matching measures including robust measures, on simulated as well as clinical data. Results show that in particular robust SAD with M-estimator is a suitable matching measure. By using a parallel projection for DRR computation instead of the commonly employed perspective, it is impossible to estimate position in perpendicular direction to the projection plane. This is, however, a crucial part of an accurate 2D-3D registration algorithm and in particular important for the application during EVAR.

Pujol et al. [116] As the gold-standard fluoroscopic guidance of catheter and stent graft has several pitfalls in terms of radiation exposure and use of nephrotoxic radiographic contrast, the authors investigate the application of interventional transabdominal Ultrasound imaging (US). As this imaging technique can not be used as a tracking tool to follow the progression of the endoprosthesis, a navigation system is developed that enables a real-time localization of the endoprosthesis via registration between pre-operative CT scans, intra-operative 2.5D US data, and the magnetically tracked delivery device of an endoprosthesis. A modified ICP algorithm computes the transformation between the internal surface of the aorta segmented from CT images and its position in the ultrasound data. Although preliminary results are promising, research in this direction have not been conducted any further.

Göksu et al. [51] The authors propose a 3D navigation system for standard fluoroscopic guided EVAR. Prior to the intervention, physicians are able to plan the navigation and stent placement in a patient-specific virtual environment allowing to segment the abdominal vessel tree in the preoperative CT scan and to position a virtual C-arm in order to simulate 2D fluoroscopy-like images of the scan. Intraoperatively, 2D fluoroscopic views are reproduced from the planned C-arm positions and registered to the preoperative CT volume by means of a chamfer distance map. The 3D localization of the endovascular devices is tracked either interactively by the user or automatically on the 2D sequences by a block matching method. The system further realizes a first solution to take into account tissue deformation by medical instruments and to update the virtual environment with the intraoperative data. Therefore, the vessel centerline is extracted in 2D, backprojected into the 3D environment of the CT scan employing the projection parameters found by the previous registration procedure. These 3D points are then non-rigidly matched to the centerline points of the vessel extracted from the preoperative CT volume. This procedure, however, assumes that the C-arm pose has not changed since the execution of the 2D-3D registration. In practice, this can not be assured as the C-arm pose as well as the table position changes constantly during conventional EVAR. Without any possibility to access the approximate translation parameters of both the C-arm and the patient table, the proposed method would be too inefficient for practical use.

Raheem et al. [117] Compared to the previously reviewed publications employing rigid 2D-3D registration algorithms, Raheem et al. suggest to additionally use a non-rigid 2D-3D registration of the preoperatively acquired CT and intraoperative fluoroscopic images during the EVAR intervention. Therefore, an initial rigid registration of both datasets is refined by manually picked landmarks and the thin plate spline algorithm to deform the CT surface so it more accurately represents the interventional scene. Experiments show that registration errors can be reduced significantly compared to a rigid registration only. For practical use, however, the presented method need to be further automated.

Liao et al. [85] The authors present a deformable 2D-3D registration algorithm for AAAs that takes less user interaction than the previously described aproach. The proposed method takes the 3D graph generated from a segmentation of the CT volume and the 2D distance map calculated from the 2D X-ray image as the input. The similarity measure consists of a difference measure, a length preservation term and a smoothness regularization term, all of which are defined and efficiently calculated on the graph. Although experiments on synthetic as well as real clinical images show promising results, a suitable 2D segmentation of the vessel might not always be easy to achieve, in particular when medical instruments are present within the anatomy.

Manstad-Hulaas et al. [92] The authors evaluate the feasibility of electro-magnetic tracking in combination with fluoroscopic guidance for EVAR navigation support. A custom made stent graft is guided to the proper position with the aid of sensors attached to the catheter and providing position information for visualization within the preoperative CT scan. Results show that the use of electro-magnetic tracking in combination with fluoroscopic guidance is feasible for EVAR. Deformation and other anatomy changes in between the preoperative and intraoperative situation are, however, not taken into account and it is highlighted by the authors that solutions to this problem can increase the impact of the proposed method.

Carrell et al. [19] The authors examine the feasibility of an automated rigid 2D-3D image registration system to simplify the navigational challenges faced in complex endovascular aortic procedures. The method first requires the user to select a region of interest where the intensity-based rigid registration is based on. DRR images are computed subsequently during optimization using the internal parameters of the X-ray device. Visual as well as quantitative analysis of the errors measured in manually picked landmark points, reveals good results for axial views. However, the algorithm fails when used in highly angulated aortas because of the degree of aortic deformation caused by the introducer and endovascular graft.

Although EVAR provides substantial clinical benefit for the patient [60], severe long-term problems including stent graft migration and aorta deformation have been reported in clinical research studies [105, 53, 5]. The analysis and quantification of stent graft migration have been subject to extensive research work in the medical imaging community [96, 79, 78], all addressing thoracic stent graft migration induced by the heart movement and continuous blood pressure in downward direction. The deformation and implied degeneration of the aorta by the stent graft is again reason for several long-term complications such as recalcification and endoleakage creation. Existing publications concern the analysis of flow changes and detection of turbulences as indication for locations of high complication risk [86, 62] rather than the deformation of the aorta induced by the stent graft. We have presented a method to quantify this deformation by non-rigidly aligning the preoperative and the postoperative aortic shape extracted from the pre and postinterventional patient scans respectively. The details of our procedure are described within appendix D.

5. Dissimilarity in Interventional Image Registration

Intensity-based image registration matches two images according to their contents, e.g. intensities, assuming that all parts of the images are visible and not corrupted. In interventional images however, important image information might be occluded by medical instruments such as catheters, grafts, and probes. Also, the unideal acquisition situation further introduces noise into the image acquisition process that is visible in the resulting images. If not taken into account, such dissimilarities and occlusions can severely affect the robustness of image registration algorithms.

5.1. Robust Similarity Measures

Most of the intensity-based similarity measures described in Section 3.3.3 are not robust with respect to outliers, therefore large intensity differences can affect this error term significantly. When it comes to a realistic interventional setup, robust measures are preferred due to difficult image quality and dissimilarity occurrences [107].

Due to its power in separating outlying noise in data, *M-estimators* have been widely used in statistics [65, 134]. For estimating a parameter vector $V = [v_1, v_2, \ldots, v_n]^T$, M-estimators are generalizations of the usual maximum likelihood estimates with the more general structure

$$\arg\min_V \left(\prod_i \rho(x_i|V) \right) \tag{5.1}$$

where ρ is a symmetric positive definite function with a unique minimum at zero and is chosen to increase slower than quadratically. Instead of solving this problem directly, we can reformulate it as an iterated weighted least-square problem

$$\sum \psi(x_i, V) \frac{dx_i}{dj} = 0 \quad \text{for } j = 1, 2, \ldots, n. \tag{5.2}$$

The derivative $\psi(x) = \frac{d\rho(x)}{dx}$ is called *influence function*, which measures the influence of data point on the value of parameter estimate. There exist several choices for ρ and ψ in the literature and the most popular are listed in Fig. 5.1. Several of these methods have been used in combination with conventional similarity measures to allow robust image registration. In the following, we will give a review of these robust measures employing the notation introduced in section 3.3.3.

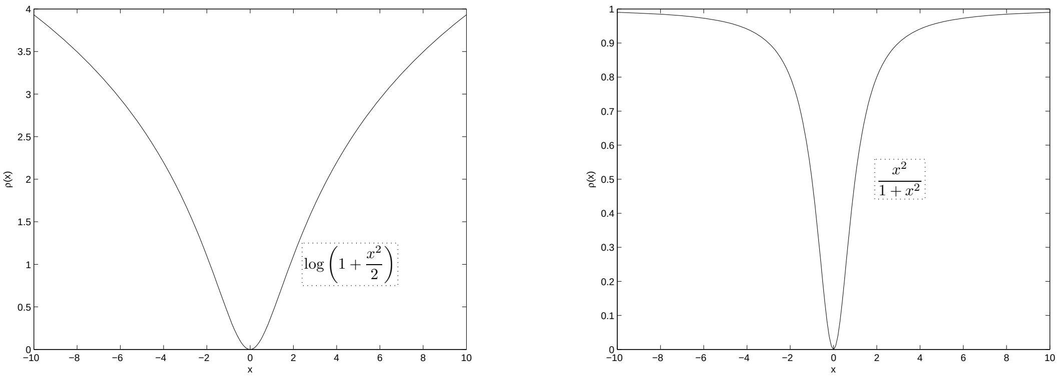

(a) Cauchy (b) Geman-McClure

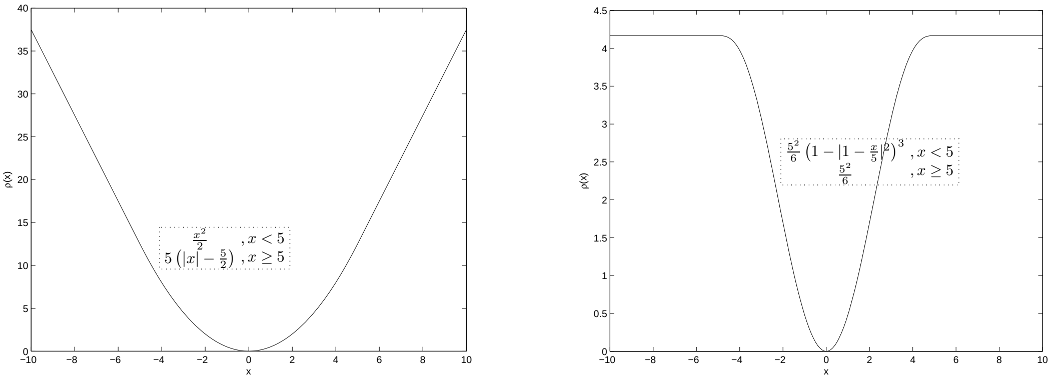

(c) Huber (d) Tukey

Figure 5.1.: Famous M-estimator functions and plots of the corresponding ρ-functions

Arya et al. [2] The authors suggest robust registration with their introduced *M-estimator Correlation Coefficient* (MCC), a combination of *Huber* [65] and *Tukey* [134] *M-estimators* (see Fig. 5.1(c) and 5.1(d)) with the $\mathcal{NCC}$ measure:

$$\mathcal{MCC}_{\text{Huber}}(I,J)=\frac{\sum_{i=1}^{N} m^H(i)\left(I(\mathbf{x}_i)-\bar{I}\right)\left(J(\mathbf{x}_i)-\bar{J}\right)}{\sqrt{\sum_{i=1}^{N} m_I^H(i)\left(I(\mathbf{x}_i)-\bar{I}\right)^2}\sqrt{\sum_{i=1}^{N} m_J^H(i)\left(J(\mathbf{x}_i)-\bar{J}\right)^2}} \tag{5.3}$$

and

$$\mathcal{MCC}_{\text{Tukey}}(I,J)=\frac{\sum_{i=1}^{N} m^T(i)\left(I(\mathbf{x}_i)-\bar{I}\right)\left(J(\mathbf{x}_i)-\bar{J}\right)}{\sqrt{\sum_{i=1}^{N} m_I^T(i)\left(I(\mathbf{x}_i)-\bar{I}\right)^2}\sqrt{\sum_{i=1}^{N} m_J^T(i)\left(J(\mathbf{x}_i)-\bar{J}\right)^2}} \tag{5.4}$$

where

$$m_I^H(i)=\begin{cases} I(\mathbf{x}_i)-\bar{I}, & |I(\mathbf{x}_i)-\bar{I}|<k_1 \\ k_h^H \operatorname{sgn}\left(I(\mathbf{x}_i)-\bar{I})\right), & \text{otherwise}\end{cases}$$

$$m_J^H(i)=\begin{cases} J(\mathbf{x}_i)-\bar{J}, & J(\mathbf{x}_i)-\bar{J}<k_2 \\ k_v^H \operatorname{sgn}\left(J(\mathbf{x}_i)-\bar{J}\right), & \text{otherwise}\end{cases}$$

and

$$m_h^T(i) = \begin{cases} (I(\mathbf{x}_i) - \bar{I}) \left(1 - \left(\frac{I(\mathbf{x}_i)-\bar{I}}{k_h^T}\right)^2\right)^2, & |I(\mathbf{x}_i) - \bar{I}| < c_1 \\ 0, & \text{otherwise} \end{cases}$$
$$m_v^T(i) = \begin{cases} (J(\mathbf{x}_i) - \bar{J}) \left(1 - \left(\frac{J(\mathbf{x}_i)-\bar{J}}{k_v^T}\right)^2\right)^2, & |J(\mathbf{x}_i) - \bar{J}| < c_2 \\ 0, & \text{otherwise} \end{cases}$$

Here, k_1, k_2, c_1, c_2 are predefined constants and represent the thresholds k, c of the Huber and Tukey M-estimators.

Weese et al. [140] Another famous choice for robust measures is the Geman and McClure [77] function visualized in Fig. 5.1(b). Weese et al. chose to employ a slight adaptation of this estimator for *Pattern Intensity* that is defined as

$$\mathcal{PI}(I, J) = \sum_{i=1}^{N} \sum_{d^2<r^2} \frac{\sigma^2}{\sigma^2 + ((I - sJ)(\mathbf{x}_i) - (I - sJ)(\mathbf{y}))^2} \tag{5.5}$$
$$d^2 = (x_1 - y_1)^2 + (x_2 - y_2)^2 \tag{5.6}$$

for a predefined search radius r and weight σ. The scaling value s for the creation of appropriate difference images must be determined carefully.

Penney et al. [107] Similar to Weese et al., the author combine the Geman and McClure function (Fig. 5.1(b)) with image gradient information. Their presented *Gradient Difference* is defined as

$$\mathcal{GD}(I, J) = \sum_{i=1}^{N} \frac{A_h}{A_h + \left(\frac{dI}{dx}(x, y) - s\frac{dJ}{dx}(x, y)\right)^2} \tag{5.7}$$
$$+ \sum_{(x,y)} \frac{A_v}{A_v + \left(\frac{dI}{dy}(x, y) - s\frac{dJ}{dy}(x, y)\right)^2} \tag{5.8}$$

where A_h, A_v are the variances of the gradient images $\frac{dI}{dx}, \frac{dI}{dy}$. Here, the scaling value s for the creation of appropriate difference images is optimized such that the entropy H of the difference image is minimal.

Imamura et al. [66, 40] Also employing an adapted version of the Geman and McClure [77] function (Fig. 5.1(b)), the authors present a robust version of SAD defined as

$$\mathcal{SAD}_{\text{robust}}(I, J) = \sum_{i=1}^{N} \frac{|I(\mathbf{x}_i) - J(\mathbf{x}_i)|^2}{\sigma^2 + |I(\mathbf{x}_i) - J(\mathbf{x}_i)|^2} \tag{5.9}$$

where $\sigma > 0$ is a constant defining the slope of the parabola.

Lai [77] Lai uses a combination the Cauchy M-estimator visualized in Fig. 5.1(a), and the SSD similarity measure to form new robust version defined as

$$\mathcal{SSD}_{\text{robust}}(I,J) = \sum_{i=1}^{N} \log\left(1 + \frac{(I(\mathbf{x}_i - J(\mathbf{x}_i))^4}{2\sigma}\right) \tag{5.10}$$

where $\sigma > 0$ is a constant defining the slope of the parabola.

Nikou et al. [100] Nikou et al. presents the usage of two similarity measures related to M-estimators, *robust least squares* and *robust inter-image uniformity*, for mono- and multi-modal 2D-3D registration. Thereby, their registration method can robustly handle dissimilarities occurring from large lesion evolution for multiple sclerosis patients, anatomy deformation, and different information representation for multi-modal images.

Gerogiannis et al. [49] Instead of incorporating M-estimators, Gerogiannis et al. designed a robust statistical similarity measure incorporating a *Student's t-mixture model*. Compared to a Gaussian mixture model, it provides robustness to outliers by heavier tails in the distribution plot.

5.2. Disocclusion for Image Registration

Instead of employing robust measures for image matching or registration, disocclusion aims at reconstructing the occluded parts of the image retaining its physical model. If combined with a registration procedure, disocclusion takes into account information about the shape or location of the occlusion whereas robust measures restrict outliers by smoothing the plot of the measure. However, one drawback compared to robust measures is the introduction of user interaction or preprocessing step in order to find the rough outline of the occlusion. In the following, we review several successful attempts of combining disocclusion with image registration.

Kaneko et al. [70] Kaneko et al. presents the *selective correlation coefficient* that masks out pixels belonging to the occluded region and only calculates the well-known correlation coefficient measure (see section 3.3.3) on non-occluded pixels. Compared to the usage of robust similarity measures, the application of binary masks require the user to at least outline the image occlusion region.

McGuire and Stone [97] The authors introduce fractional masks, an extension of binary occlusion masks, for use in coarse-to-fine registration algorithm using $\mathcal{NCC}$ (see section 3.3.3) similarity measure. Each coarse pixel has a corresponding fractional-mask value that gives the fraction of unoccluded fine pixels subsumed by the coarse pixel. Compared to binary masks, fractional masks tend to have lower false match rates.

Periaswamy et al. [109] A general-purpose registration algorithm for medical images is presented. In order to contend with partial or missing data, the expectation maximization (EM) algorithm [36] is incorporated. In the E-step, weights w are computed representing the likelihood for every pixel to belong to the non-occluded image region. The registration parameters are then estimated in the M-step where pixels having a lower weight, are given less consideration. Compared to the application of a binary or fractional mask, this approach does not require any user input on the actual position of the occlusion within the image.

Tomaževič, Markelj et al. [132, 94] Another solution to the problem of occlusions is given by reconstruction-based registration methods that first reconstructs a 3D image from two or more fluoroscopic or X-ray images acquired from different viewing angles, and then perform a 3D-3D registration. The authors additionally introduce a robust similarity measure based on mutual information, namely *asymmetric multifeature mutual information* [132], that gives robust results also for poor quality volumes resulting from a reconstruction of only a few interventional fluoroscopy images. Addressing the problem of high computation time, the authors propose to reconstruct only parts of the interventional scene in a subsequent publication [94]. By matching the volume gradients of the preoperative image to 3D gradients coarsely reconstructed from 2D interventional images, it is possible to reduce the number of required 2D images to reconstruct from, to only a few. Thereby, the authors are able to reduce computation time while improving accuracy and robustness at the same time. Although, it is shown by extensive evaluations that the reconstruction-based method is able to outperform conventional 2D-3D registration methods in terms of capture range and success rate, the requirement of several interventional images acquired from different viewpoints is a limitation for clinical use during EVAR.

Part III.

New Approaches to Computer Assistance for Endovascular Abdominal Aortic Repairs

6. Interventional Image Registration: Addressing Dissimilarity in Images

An important of goal of computer aided intervention is enhancing the intraoperative visualization with 3D image information and thereby providing navigation support to the physicians. Although modern angiographic systems allow three dimensional reconstructions during EVAR (see section 2.1.5 for more detail), detectors only cover a small region that does not include enough information for navigation tasks during abdominal aortic interventions. Thus, there is a need for combining preoperative 3D image information with 3D intraoperative image data. In an interventional setup, however, image dissimilarites lead to corrupt image information and therefore obstruct accuracy of existing registration algorithms.

Based on our publications [33, 93, 32], we propose two novel robust similarity measures in order to handle image dissimilarities and occlusions for rigid 3D-3D registration. In our experiments, we match intraoperative C-arm cone-beam CT images with preoperative CTA scans and compare results of our robust measures to those of algorithms using non-robust measures. The accuracy and robustness of our registration framework was further compared to a commercially available method included in Siemens Workstations that come along with AXIOM Artis angiography suites.

6.1. Robust Gradient Correlation Measures

When it comes to a realistic interventional setup, robust measures are preferred due to difficult image quality and dissimilarity occurrences [107]. For our intended medical application, we use the visible bony structure to align an interventional reconstruction volume to the preoperative CTA. We will therefore focus on robust gradient-based similarity measures.

In the following two paragraphs, we combine the two most powerful robust M-estimators with *gradient correlation* $\mathcal{GC}$ (see section 5.1). For the sake of a clearer arrangement of the notations in the remainder of this section, let us define

$$\mathcal{K}_h(x,y,z) = \left(\frac{dI}{dx}(x,y,z) - \overline{\frac{dI}{dx}}\right)\left(\frac{dJ}{dx}(x,y,z) - \overline{\frac{dJ}{dx}}\right) \tag{6.1}$$

$$\mathcal{K}_v(x,y,z) = \left(\frac{dI}{dy}(x,y,z) - \overline{\frac{dI}{dy}}\right)\left(\frac{dJ}{dy}(x,y,z) - \overline{\frac{dJ}{dy}}\right) \tag{6.2}$$

$$\mathcal{K}_d(x,y,z) = \left(\frac{dI}{dz}(x,y,z) - \overline{\frac{dI}{dz}}\right)\left(\frac{dJ}{dz}(x,y,z) - \overline{\frac{dJ}{dz}}\right). \tag{6.3}$$

6.1.1. Huber Gradient Correlation

Huber[65] describes the M-estimator (see section 5.1) as a parabola in the vicinity of zero that increases linearly at a given level k. Bringing the influence function of this M-estimator together with the $\mathcal{GC}$-measure results in the following notation for our novel similarity measure *Huber Gradient Correlation*:

$$\mathcal{HGC}(I,J) = \frac{\sum_{i=1}^{N} m_h^H(\mathbf{x}_i)}{\sqrt{\sum_{i=1}^{N} m_h^H(\mathbf{x}_i)^2}} + \frac{\sum_{i=1}^{N} m_v^H(\mathbf{x}_i)}{\sqrt{\sum_{i=1}^{N} m_v^H(\mathbf{x}_i)^2}} + \frac{\sum_{i=1}^{N} m_d^H(\mathbf{x}_i)}{\sqrt{\sum_{i=1}^{N} m_d^H(\mathbf{x}_i)^2}} \tag{6.4}$$

$$m_h^H(\mathbf{x}_i) = \begin{cases} \mathcal{K}_h(x,y,z), & |\mathcal{K}_h(x,y,z)| < k_h^H \\ k_h^H \operatorname{sgn}\left(\mathcal{K}_h(x,y,z)\right), & \text{otherwise} \end{cases}$$
$$m_v^H(\mathbf{x}_i) = \begin{cases} \mathcal{K}_v(x,y,z), & |\mathcal{K}_v(x,y,z)| < k_v^H \\ k_v^H \operatorname{sgn}\left(\mathcal{K}_v(x,y,z)\right), & \text{otherwise} \end{cases}$$
$$m_d^H(\mathbf{x}_i) = \begin{cases} \mathcal{K}_d(x,y,z), & |\mathcal{K}_d(x,y,z)| < k_d^H \\ k_d^H \operatorname{sgn}\left(\mathcal{K}_d(x,y,z)\right), & \text{otherwise} \end{cases}$$

Here, $\mathcal{K}_h, \mathcal{K}_v, \mathcal{K}_d$ are the functions defined in (6.1-6.3) and k_h^H, k_v^H, k_d^H represent the threshold k of the Huber M-estimator for each of the gradient directions x, y, z. We set these values to

$$\begin{aligned} k_h^H &= \alpha \cdot \sigma_x(I)\sigma_x(J) \\ k_v^H &= \alpha \cdot \sigma_y(I)\sigma_y(J) \\ k_d^H &= \alpha \cdot \sigma_z(I)\sigma_z(J) \end{aligned}$$

where $\sigma_x, \sigma_y, \sigma_z$ are the standard deviations of pixel intensities in x-,y-, and z-direction respectively and α is a predefined constant defining the outlier threshold. For our experiments on synthetic and real medical images, we empirically found $\alpha = 1.5$ to produce the best results.

6.1.2. Tukey Gradient Correlation

In contrast to Huber's parabolic function, Tukey[134] describes an M-estimator as a bisquare function that saturates for large values beyond a given level c instead of increasing linearly. Combining this M-estimator with the $\mathcal{GC}$-measure, we introduce *Tukey Gradient Correlation* as

$$\mathcal{TGC}(I,J) = \frac{\sum_{i=1}^{N} m_h^T(\mathbf{x}_i)}{\sqrt{\sum_{i=1}^{N} m_h^T(\mathbf{x}_i)^2}} + \frac{\sum_{i=1}^{N} m_v^T(\mathbf{x}_i)}{\sqrt{\sum_{i=1}^{N} m_v^T(\mathbf{x}_i)^2}} + \frac{\sum_{i=1}^{N} m_d^T(\mathbf{x}_i)}{\sqrt{\sum_{i=1}^{N} m_d^T(\mathbf{x}_i)^2}} \tag{6.5}$$

$$m_h^T(\mathbf{x}_i) = \begin{cases} \mathcal{K}_h(\mathbf{x}_i)\left(1-\left(\frac{\mathcal{K}_h(\mathbf{x}_i)}{k_h^T}\right)^2\right)^2, & |\mathcal{K}_h(\mathbf{x}_i)| < k_h^T \\ 0, & \text{otherwise} \end{cases}$$
$$m_v^T(\mathbf{x}_i) = \begin{cases} \mathcal{K}_v(\mathbf{x}_i)\left(1-\left(\frac{\mathcal{K}_v(\mathbf{x}_i)}{k_v^T}\right)^2\right)^2, & |\mathcal{K}_v(\mathbf{x}_i)| < k_v^T \\ 0, & \text{otherwise} \end{cases}$$
$$m_d^T(\mathbf{x}_i) = \begin{cases} \mathcal{K}_d(\mathbf{x}_i)\left(1-\left(\frac{\mathcal{K}_d(\mathbf{x}_i)}{k_d^T}\right)^2\right)^2, & |\mathcal{K}_d(\mathbf{x}_i)| < k_d^T \\ 0, & \text{otherwise} \end{cases}$$

As already applied for the definition of $\mathcal{HGC}$, $\mathcal{K}_h, \mathcal{K}_v, \mathcal{K}_d$ are the functions defined in (6.1-6.3). k_h^T, k_v^T, k_d^T represent the threshold c of the Tukey M-estimator for each of the gradient directions x, y, z. Here, we set these values to

$$\begin{aligned} k_h^T &= \beta \cdot |\sigma_x(I^{fluoro}) - \sigma_x(I^{drr})| \\ k_v^T &= \beta \cdot |\sigma_y(I^{fluoro}) - \sigma_y(I^{drr})| \\ k_d^T &= \beta \cdot |\sigma_z(I^{fluoro}) - \sigma_z(I^{drr})| \end{aligned}$$

where σ_x, σ_y are the standard deviations of pixel intensities in x-,y-, and z-direction respectively and β is a predefined constant defining the outlier threshold. For our experiments on synthetic and real medical images, we empirically found $\beta = 4.7$ to produce the best results.

6.2. Evaluation

The above described methods were embedded into a registration framework for matching 3D preoperative CTA scans to interventional C-arm cone beam CT scans of the same patient. Besides $\mathcal{HGC}$ and $\mathcal{TGC}$, we included $\mathcal{NCC}$ and $\mathcal{GC}$ for a comparative analysis of our proposed measures. The optimization of the registration equation was performed by the *Downhill Simplex* method.

We also tested the impact of binary maps for eliminating outliers in the optimization space introduced by medical instruments present in the intraoperative scan. Therefore, we employed the one-click connected component segmentation filter provided by ITK[1] that performs a region growing starting from a user indicated seed point. As lower and upper intensity thresholds ($p_{\text{lower}}, p_{\text{upper}}$), we defined

$$p_{\text{lower}} = \frac{1}{2}\max_{\mathbf{x}}(I(\mathbf{x})) \qquad p_{\text{upper}} = \max_{\mathbf{x}}(I(\mathbf{x})) \tag{6.6}$$

All experiments were performed on an Intel Core 2 PC containing 2.66 GHz CPU and 4096 MB of main memory. CTA images were acquired by either Siemens Somatom Sensation 64 or Siemens Somatom Definition, interventional images were taken by Siemens AXIOM Artis dTA angiography suite with dynaCT software. A total number of 6 datasets were made available by our medical partners and the respective image dimensions are given in the following table:

---

[1] Insight Toolkit, Kitware, `www.itk.org`

Table 6.1.: Dimensions of preoperative and intraoperative images

	image size (pixels)	pixel size (mm)
CTA	$512 \times 512 \times 300 - 657$	$0.52 \times 0.52 \times 0.5 - 2.0$
C-arm cone beam CT	$256 \times 256 \times 219$	$0.86 \times 0.86 \times 0.86$

In the following accuracy evaluation, a ground-truth transformation T_{gt} for every dataset was defined by a medical expert. On the basis of ten points randomly distributed over the entire interventional volume, we created 12 different starting positions yielding initial $mTRE$ values from 1 mm to 12 mm. As quantitative measures of accuracy, we calculated RMS errors in each of the 6 rigid body parameters $t_x, t_y, t_z, r_x, r_y, r_z$ and the average final $mTRE$ for each of the 6 datasets. Table 6.2

Table 6.2.: Accuracy evaluation of 3D-3D registration: RMS errors in rigid body parameters and final $mTRE$ values in mm averaged on all 6 datasets.

	Translation			Rotation			$mTRE$
	t_x (mm)	t_y (mm)	t_z (mm)	r_x (rad)	r_y (rad)	r_z (rad)	
$\mathcal{NCC}$	73.9	60.4	101.5	1.0	1.7	0.2	99.3
$\mathcal{NCC}_{\text{binary mask}}$	62.1	50.9	77.3	0.8	1.4	0.1	75.1
$\mathcal{GC}$	0.9	5.9	9.8	0.03	0.1	0.02	3.9
$\mathcal{GC}_{\text{binary mask}}$	0.9	2.3	1.9	≈ 0.0	0.1	≈ 0.0	1.7
$\mathcal{HGC}$	0.7	2.3	3.1	≈ 0.0	≈ 0.0	≈ 0.0	0.8
$\mathcal{HGC}_{\text{binary mask}}$	0.7	2.2	2.5	≈ 0.0	≈ 0.0	≈ 0.0	0.4
$\mathcal{TGC}$	0.9	2.0	3.5	≈ 0.0	≈ 0.0	≈ 0.0	1.0
$\mathcal{TGC}_{\text{binary mask}}$	0.5	2.0	3.1	≈ 0.0	≈ 0.0	≈ 0.0	0.5

shows these values averaged on all datasets. By comparing the numbers, it becomes obvious that $\mathcal{NCC}$ does not yield satisfying results even when a binary map is included ($mTRE$ values of 99.3 mm and 75.1 mm). Already by using a gradient-based measure, results can be improved to a large extent and the mean value for $mTRE$ decreases to 3.9 mm. Our proposed measures $\mathcal{HGC}$ and $\mathcal{TGC}$ yield similar small error measures as $\mathcal{GC}$ combined with a binary map. The improvement that can be achieved by also including a binary map for $\mathcal{HGC}$ and $\mathcal{TGC}$ are only marginaland therefore the additional requirement for user interaction for obtaining such a binary map can be omitted.

In order to further evaluate the practical impact of our $\mathcal{HGC}$ measure which gave best results for our previous example, we compared its results to a commercial registration method by Siemens Medical Solutions available on syngo X Workplace VA 60, 2003/04 which is based on $\mathcal{MI}$. In the course of a medical study, 14 intra- and postoperative datasets were registered 10 times with both algorithms yielding 140 registrations for each program. In all data sets five specified landmarks placed by two radiologists were used to evaluate the registration accuracy by calculating $mTRE$. A ground truth transformation was calculated by matching the 5 landmarks in the intra- and postoperative volumes.

The $mTRE$ mean ± SD for registrations using $\mathcal{MI}$ was 5.05 4.74 mm which

Table 6.3.: Comparative study of $\mathcal{HGC}$ and $\mathcal{MI}$

	$mTRE$ for $\mathcal{MI}$ (mm)	$mTRE$ for $\mathcal{HGC}$ (mm)
median	3.58	3.68
mean ± SD	5.05 ± 4.74	4.02 ± 1.52
min - max	1.7 - 36.8	1.8 - 9.4
90-percentile	9.1	5.8

could be reduced to 4.02 1.52 mm by $\mathcal{HGC}$ (see Table 6.3). Although the $mTRE$ median is slightly better for $\mathcal{MI}$ (3.6 mm compared to 3.7 mm), overall $mTRE$ values for $\mathcal{HGC}$ were significantly lower (p ¡ 0.001).

In summary, our proposed robust similarity measures $\mathcal{HGC}$ and $\mathcal{TGC}$ yield good results for registering intraoperative C-arm cone beam CT images to preoperative CTA scans and $\mathcal{HGC}$ outperforms $\mathcal{MI}$ for the same data.

7. Disocclusion-based Image Registration

This chapter is based on our publication [32] where we investigate the impact of disocclusion concepts to handle occlusion for 2D-3D medical image registration.

We present two disocclusion techniques, *Spline Interpolation* and *Stent Editing*, and integrate these in a novel registration procedure. Compared to robust similarity measures that restrict outliers by smoothing the plot of the measure and do not incorporate any information about the shape or location of the occlusion, disocclusion aims at reconstructing the image without the occluded region retaining the physical model of the image.

For evaluation purposes, we have performed extensive experiments on synthetic as well as patient data. We have evaluated the impact of the novel disocclusion techniques as well as the existing *Digital Image Inpainting* [6, 15] on registrations using *Gradient Correlation*, *Huber Gradient Correlation*, *Tukey Gradient Correlation*, and *Gradient Difference* [107] measures. Bringing together three disocclusion techniques with four similarity measures results in 16 evaluation cases including four evaluations of the similarity measures only, without any prior disocclusion. Using a standardized evaluation methodology, we perform a total amount of 144 registrations per case in each experiment.

The remainder of this chapter is organized as follows. After introducing our disocclusion techniques *Spline Interpolation* and *Stent Editing* within section 1, we describe the entire registration framework in section 2. The experimental setup and its results are presented in section 3.

7.1. Disocclusion Techniques

Compared to robust similarity measures that perform an outlier reduction for registration algorithms, disocclusion aims at reconstructing the image in the occluded region while retaining the physical model of the image.

Recapitulating the notation introduced in section 3.4, let $\Gamma \subset \Omega$ describe the occluded image part and $\partial\Gamma$ its boundary.

In the remainder of this section, we describe two methods for obtaining the intensity values $I(x_\Gamma, y_\Gamma)$ for all pixel positions $(x_\Gamma, x_\Gamma) \in \Gamma$ based on the image information which is available in the remaining part of the image domain $\Omega \setminus \Gamma$. In the experimental setup, we evaluate these disocclusion techniques, which act as preprocessing step for the interventional 2D-3D registration.

7.1.1. Spline Interpolation

A very intuitive way of eliminating occluded image regions consists in interpolating occluded pixels $(x_\Gamma, y_\Gamma) \in I|_\Gamma$ from all non-occluded pixels $(x, y) \in I|_{\Omega\setminus\Gamma}$ employing cubic spline curve interpolation [113]. Thereby, we approximate two B-spline curves for each image dimension:

$$C_x(u) = \sum_{i=0}^{n} N_{i,3}(u) P_i \tag{7.1}$$

$$C_y(v) = \sum_{i=0}^{m} N_{i,3}(v) P_i \tag{7.2}$$

where $N_{i,3}$ are the basis functions of degree 3 and P_i are the corresponding control points representing all $I(x, y)\ \forall (x, y) \in I|_{\Omega\setminus\Gamma}$. The non-periodic knot points $u \in \{0, 0, 0, 0, u_1, ..., u_{n-1}, 1, 1, 1, 1\}$ and $v \in \{0, 0, 0, 0, v_1, ..., v_{m-1}, 1, 1, 1, 1\}$ of the splines are calculated in chord length manner:

$$u_k = u_{k-1} + \frac{|x_k - x_{k-1}|}{N}, \quad k = 1, \ldots, n-1 \tag{7.3}$$

$$v_j = u_{j-1} + \frac{|y_j - y_{j-1}|}{M}, \quad j = 1, \ldots, m-1 \tag{7.4}$$

where N, M are the image dimensions in x and y direction. The interpolated pixel value of each occluded pixel (x_Γ, y_Γ) is then calculated by

$$I(x_\Gamma, y_\Gamma) = \frac{1}{2}\left(C_x\left(\frac{x_\Gamma}{N}\right) + C_y\left(\frac{y_\Gamma}{M}\right)\right). \tag{7.5}$$

7.1.2. Stent Editing

The core of this method is based on the *Poisson Editing* technique [108] introduced in section 3.4.2. The idea is to achieve a reconstruction of the occluded region Γ via a certain *guidance field* $g : \Gamma \to \mathbb{R}^2$.

$$\min_{\bar{I}} \int_\Gamma \left\|\nabla \bar{I} - g\right\|_2^2 dx, \text{ subject to } \bar{I}|_{\partial\Gamma} = I|_{\partial\Gamma}. \tag{7.6}$$

Given such a guidance-field g, we are seeking for an image function $\bar{I}$ that is equal to I on the boundary of Γ and whose gradient is close, with respect to the L_2-norm, to the guidance field g. The reconstructed pixel values inside Γ can be then obtained by

$$I(x_\Gamma, y_\Gamma) = \bar{I}(x_\Gamma, y_\Gamma). \tag{7.7}$$

For the success of this method, we need to carefully choose an appropriate guidance field g. We use the following two observations. Firstly, the abdominal aorta is almost parallel to the spinal column. Secondly, the outline of the catheter and thin wires of the stent graft are more or less parallel to its centerline. Thus all gradients of these wires are nearly orthogonal to the upper and lower borders of the vertebrae.

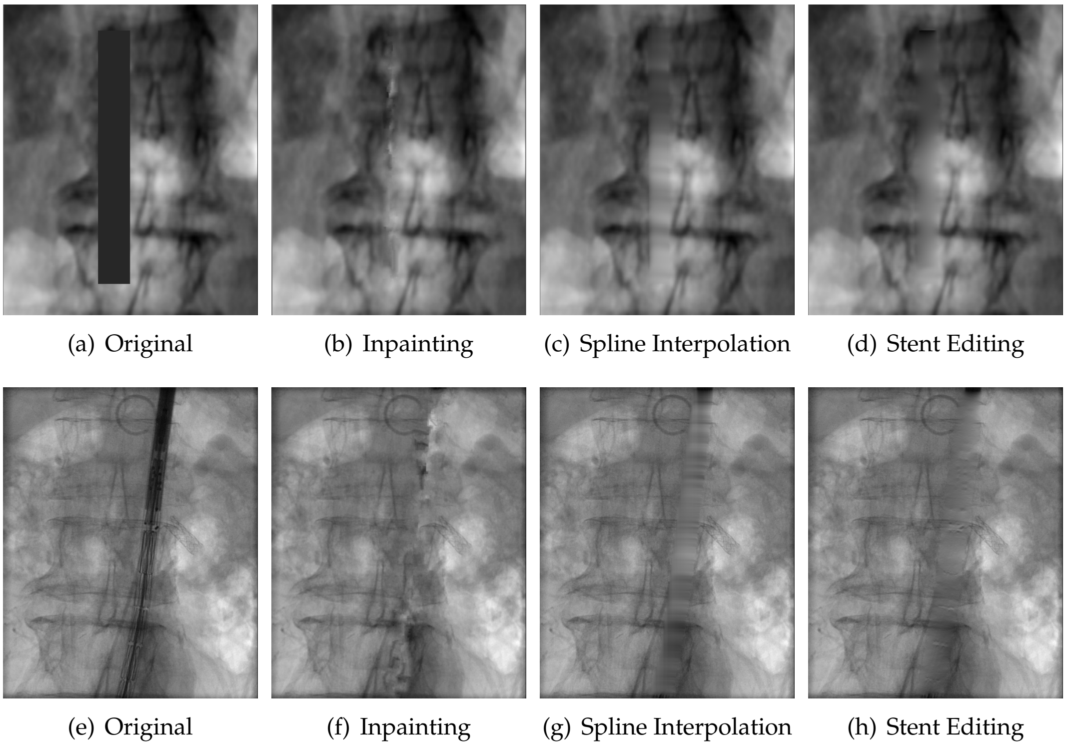
(a) Original (b) Inpainting (c) Spline Interpolation (d) Stent Editing

(e) Original (f) Inpainting (g) Spline Interpolation (h) Stent Editing

Figure 7.1.: Disocclusion processing: (a-d) real patient scan with synthetic projection and artificial occlusion, (e-h) real experiment

In order to obtain an approximation of the stent graft's centerline direction, we can compute the principal direction $\mathbf{v} \in \mathbb{R}^2$ of Ω using i.e. principal component analysis (PCA). If we assume that $\mathbf{v}$ and its orthogonal complement $\mathbf{v}^\perp$ are normalized, we can decompose ∇I as follows:

$$\nabla I(x) = \langle \nabla I(x), \mathbf{v} \rangle \cdot \mathbf{v} + \left\langle \nabla I(x), \mathbf{v}^\perp \right\rangle \cdot \mathbf{v}^\perp, \tag{7.8}$$

where $\langle \cdot, \cdot \rangle$ denotes the scalar product. The second term on the right hand side of (7.8) contains now all undesired gradients that belong to the wires of the stent graft. Consequently, a suitable guidance field is given by

$$g(x) = \langle \nabla I(x), \mathbf{v} \rangle \cdot \mathbf{v}. \tag{7.9}$$

By this choice of the guidance field we keep as much structural information as possible while avoiding to create unreasonable intensity information at the same time.

7.2. Registration Framework

We propose disocclusion-based registration with robust similarity measures to solve the problem of occlusions. As visualized in Fig. 7.2, our pipeline first initiates a reconstruction of the occluded image part, given an outline of the occluded

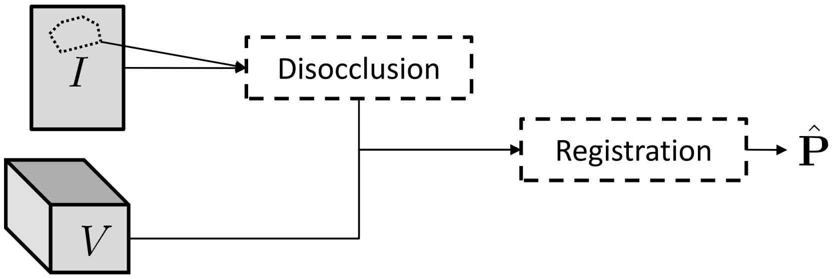

Figure 7.2.: Registration Pipeline

region, and then performs a 2D-3D registration of the reconstructed 2D image and the 3D preoperative volume employing a gradient-based similarity measure.

For our evaluation described in section 7.3, we analyze three different disocclusion techniques namely the existing *Digital Inpainting* method as well as our novel *Spline Interpolation* and *Adapted Stent Editing*. We also present an evaluation of different gradient-based similarity measures, the existing *Gradient Correlation* and *Gradient Difference* as well as the novel *Huber Gradient Correlation* and *Tukey Gradient Correlation* methods. These procedures are detailed within subsection 6.1.

In our practical implementation of the 2D-3D registration procedure, we realized the projection $\mathbf{P} \circ V$ through the concept of *Digitally Reconstructed Radiographs* (DRR) (see section 3.3.2). For its generation, we use GPU (Graphics Processing Unit) accelerated raycasting, implemented in OpenGL [41]. We employ a single render pass to compute the X-Ray attenuation A_{xy} along each ray l_{xy}.The conversion from CT houndsfield units to X-Ray attenuation values is performed by a 1D transfer function [72] which takes care of scaling, truncation, and saturation effects during conversion. The DRR images are rendered into a 32bit floating point offscreen render target and afterwards transferred to the CPU for evaluation of the similarity metric.

7.3. Experiments

A set of experiments was carried out in order to investigate the accuracy and robustness of the proposed disocclusion-based 2D-3D registration described within section B.1. We also performed a comparative study in order to analyze each of the proposed similarity measures together with the introduced disocclusion techniques.

Although segmented structures would yield ideal results, it is enough for each of the three proposed disocclusion techniques to have a rough outline of the occlusion. In a potential scenario, a manual outline of the occluded region or an indication the four corner points of a rectangle including the region could be forwarded to the disocclusion algorithm.

All registrations were carried out on a Windows XP Professional 2002 PC with Intel Core 2 CPU, 2.4 GHz, 2 GB RAM combined with 512 MB RAM on a GeForce 8800

GTS Graphics card. Except the DRR generation, the algorithms were not optimized for speed. By a number of tests, we found the *Downhill Simplex* method to give most suitable results for solving the optimization of the registration equation. The proposed algorithms could be used within interventional procedures. This requires the transfer of evaluation of similarity onto the GPU, which has been implemented and presented for several application within the medical image computing community [148].

Before presenting the results of our experiments in detail, we first give insight in our evaluation strategy in the following subsection.

7.3.1. Evaluation Strategy

We created a ground-truth projection matrix $\mathbf{P}_{gt}$ (the creation process will be explained in the following subsections) that can be decomposed in $\mathbf{P} = K\mathbf{T} = K[R|t]$ (see section 3.3.2 for more details). Given a set of 10 volume points $Q = \{\mathbf{q}_i\}$ with $i = 1, ..., 10$ randomly distributed within the overall range of the respective CT volume (including the occluded region) and following the methodology of van de Kraats et al.[137], we calculate $mTRE, mPD, mRPD$ (see section 3.3.5) for each experiment.

For all our experiments, a set of 10 volume points Q were randomly selected within the overall range of the respective CT scan. We adopted the strategy of van de Kraats et al.[137] to collect an appropriate number of different starting positions:

1. Choosing intervals for the starting position distance, 01, 12, ..., 12-13 mm.
2. For each interval, for each of the six transformation parameters, the range is determined that will yield an $mTRE$ less than or equal to the interval upper bound.
3. For each interval, transformations are generated, where the transformation parameters are chosen randomly from their predetermined range. Subsequently, the mTRE of the composite transformation is determined, and if that mTRE is within the interval it is kept, otherwise the transformation is discarded. This step is repeated until each interval contains 12 starting positions.

Next to the error measurements $mTRE, mPD, mRPD$ for accuracy inspection, we also calculate the *success rate* which indicates the percentage of registrations yielding a $mTRE$ of less than 20mm (success threshold), and the *capture range* which is 95% of the largest mPD of a successful registration. As success rate and capture range highly depend on the compactness of error distribution, their values are influenced by the selected success threshold. Due to this dependency, only the error measurements are significant accuracy indicators.

7.3.2. Real Volume with Synthetic Projection

For this experiment, a real abdominal CTA scan acquired by a SIEMENS Somatom Definition scanner, was provided by our partner clinic. We produced a DRR from

	Modality	Size	Resolution (mm)
synthetic projection	CTA	512 x 512 x 398	0,59 x 0,59 x 1,25
	DRR	308 x 982	1,00 x 1,00
real	CTA	512 x 512 x 398	0,59 x 0,59 x 1,25
	X-ray	308 x 982	0,15 x 0,15

Table 7.1.: Image dimensions for the respective experimental setups

an arbitrary projection and digitally inserted an occlusion such that the bone structure is partially hidden (FIG. 7.1(a)). The respective image dimensions are given in TABLE 7.1.

We evaluated the robustness, accuracy, and success of the proposed registration framework (see FIG. 7.2). Tests were performed using the three disocclusion techniques presented in section 7.1 followed by a 2D-3D image registration using 4 different similarity measures ($\mathcal{GC}, \mathcal{GD}, \mathcal{HGC}, \mathcal{TGC}$). Including the normal case where no disocclusion technique was applied, this sums up to 16 evaluation cases to be compared to each other. Image results of the disocclusion procedures can be seen in FIG. 7.1(a-d). TABLE 7.2 shows error measures $mTRE, mPD, mRPD$ as well as success rate and capture range for each of the cases. In additional to mean values, we present the minimum and maximum of all error measures in order to allow the reader a better analysis of the differences. In order to quantitatively determine the significance of the results, we also performed the *t-test* in between each two of the disocclusion techniques (including none) for each similarity measure separately. We computed the test three times for each error measure ($mTRE, mPD, mRPD$) resulting in three significance values for each similarity measure and each couple of dissoclusion techniques. The average significance values (p values) are presented in TABLE 7.3. A p value equal to or less than 0.05 is considered significant and less than 0.01 is considered very significant. For allowing an analysis of the effect of the robust similarity measures and disocclusion techniques to each single rigid body parameter ($t_x, t_y, t_z, r_x, r_y, r_z$) introduced in section 3.3.2, TABLE 7.4 shows the respective root mean square errors (RMSE) between ground truth values and final registration positions.

Regarding all values and measures, $\mathcal{GD}$ performs best and TABLE 7.2 shows that results can even be improved by disocclusion techniques. Whereas the original measure yields a mean mPD of 7.96 mm which is already optimal in this evaluation study, a prior treatment of the disoccluded region by *Spline Interpolation* results in a mean mPD of only 5.93 mm. This improvement is mostly due to the fact that the RMSE in depth direction (t_z) could be greatly reduced by *Spline Interpolation*, from 8.62 mm to 6.9 mm (see TABLE 7.4). However, as indicated by TABLE 7.3, there is no significant difference detectable ($p = 0.86$). An advantage of the prior employment of disocclusion techniques is an increase in success rate (from 94.44% to 100%) and capture range (from 8.55 mm to 11.58 mm). $\mathcal{GC}$ measure performs slightly worse than $\mathcal{GD}$ (minimal mPD of 11.81 mm) but results are still acceptable. TABLE 7.3 shows significant difference in between no disocclusion and *Digital Inpainting* ($p = 0.04$), and *Digital Inpainting* and *Spline Interpolation* ($p = 0.03$). Although there is no improvement detectable for the mean values of the error mea-

Table 7.2.: Evaluation study in artificial scenario with real volume for each similarity measure and each disocclusion technique (including the normal case where no disocclusion was performed)

	Gradient Correlation				**Gradient Difference**			
	normal	Inpainting	Poisson Editing	Spline Interpolation	normal	Inpainting	Poisson Editing	Spline Interpolation
mTRE mean (mm)	2.89	4.07	3.39	2.91	3.45	1.54	1.62	1.53
mTRE range	0.02 - 34.17	0.1 - 17.12	0.01 - 33.74	0.01 - 18.57	0.01 - 29.64	0.05 - 16.26	0.01 - 18.43	0.0 - 19.75
mPD mean (mm)	11.81	18.44	13.0	14.64	7.96	7.23	6.73	5.93
mPD range	0.14 - 137.97	0.27 - 170.13	0.03 - 135.67	0.03 - 124.84	0.01 - 125.84	0.41 - 99.53	0.01 - 100.95	0.0 - 117.11
mRPD mean (mm)	1.21	1.91	1.34	1.51	0.82	0.75	0.7	0.62
mRPD range	0.14 - 137.97	0.27 - 170.13	0.03 - 135.67	0.03 - 124.84	0.01 - 125.84	0.41 - 99.53	0.01 - 100.95	0.0 - 117.11
success rate (%)	89.58	100.0	95.83	100.0	94.44	100.0	100.0	100.0
capture range (mm)	1.9	11.58	3.8	11.58	8.55	11.58	11.58	11.58

	Huber GC				**Tukey GC**			
	normal	Inpainting	Poisson Editing	Spline Interpolation	normal	Inpainting	Poisson Editing	Spline Interpolation
mTRE mean (mm)	6.25	2.47	18.72	17.46	3.05	3.01	17.75	17.16
mTRE range	0.01 - 27.5	0.08 - 23.0	2.6 - 38.7	5.22 - 38.37	0.01 - 27.62	0.05 - 21.16	1.42 - 41.73	0.778 - 38.75
mPD mean (mm)	34.0	6.58	141.61	129.72	14.34	11.22	131.74	121.56
mPD range	0.01 - 264.88	0.24 - 72.08	19.48 - 318.36	4.95 - 420.81	0.01 - 159.64	0.26 - 119.28	9.11- 300.41	3.32 - 341.28
mRPD mean (mm)	3.5	0.68	14.52	13.3	1.5	1.16	13.54	12.49
mRPD range	0.01 - 264.88	0.24 - 72.08	19.48 - 318.36	4.95 - 420.81	0.01 - 159.64	0.26 - 119.28	9.11- 300.41	3.32 - 341.28
success rate (%)	70.83	99.31	61.81	70.14	86.81	96.53	64.58	72.22
capture range (mm)	3.8	5.7	0.95	0.95	14.34	11.4	0.95	0.95

Table 7.3.: Significance values (MATLAB t-test)

Gradient Correlation	Inpainting	Interpolation	Poisson Editing
normal	0.04	0.97	0.47
Inpainting		0.03	0.30
Interpolation			0.46

Huber GC	Inpainting	Interpolation	Poisson Editing
normal	0.00	0.00	0.00
Inpainting		0.00	0.00
Interpolation			0.11

Gradient Difference	Inpainting	Interpolation	Poisson Editing
normal	0.84	0.86	0.69
Inpainting		0.99	0.85
Interpolation			0.86

Tukey GC	Inpainting	Interpolation	Poisson Editing
normal	0.94	0.00	0.00
Inpainting		0.00	0.00
Interpolation			0.44

Table 7.4.: Mean values for estimation errors in rigid body parameters

	Gradient Correlation				**Gradient Difference**			
	normal	Inpainting	Poisson Editing	Spline Interpolation	normal	Inpainting	Poisson Editing	Spline Interpolation
t_x (mm)	6.94	4.69	5.06	6.43	5.32	4.31	4.79	4.3
t_y (mm)	3.61	3.23	2.77	2.56	1.34	3.11	1.25	1.27
t_z (mm)	16.52	17.63	22.09	13.65	8.24	10.72	12.38	6.9
r_x (degree)	0.24	0.25	0.2	0.27	0.15	0.21	0.09	0.17
r_y (degree)	0.35	0.35	0.36	0.3	0.23	0.23	0.25	0.26
r_z (degree)	0.27	0.17	0.13	0.16	0.06	0.05	0.1	0.07
	Huber GC				**Tukey GC**			
	normal	Inpainting	Poisson Editing	Spline Interpolation	normal	Inpainting	Poisson Editing	Spline Interpolation
t_x (mm)	4.86	2.66	13.95	12.85	5.0	4.02	11.89	12.65
t_y (mm)	5.1	2.88	10.21	15.97	3.89	3.85	12.88	12.93
t_z (mm)	18.38	16.7	30.94	24.88	12.89	15.56	24.81	26.92
r_x (degree)	0.36	0.19	0.65	0.67	0.4	0.34	0.74	0.85
r_y (degree)	0.49	0.18	1.11	0.91	0.19	0.28	1.01	0.89
r_z (degree)	0.53	0.06	1.35	1.19	0.25	0.08	1.15	1.06

sures, it is obvious that the maximal $mTRE$ values could be reduced from 34.17 mm to 17.12 mm (*Digital Inpainting*) and to 18.57 mm (*Spline Interpolation*). This is also the reason for the big improvement of success rate and capture ranges as these values are calculated from the $mTRE$ values. TABLE 7.4 confirms this observation as there is slight improvement detectable for some of the RMSE. Robust measures $\mathcal{HGC}, \mathcal{TGC}$ bring up the rear of this evaluation study. Without any prior disocclusion, they yield mean mPD values of 34 mm and 14.34 mm and have low success rates (70.38%,86.81%). These results can only be improved in combination with *Digital Inpainting*. With a mean mPD value of 6.58 mm and 99.31 $\%$ success, $\mathcal{HGC}$ comes close to results achieved by $\mathcal{GC}, \mathcal{GD}$ whereas $\mathcal{TGC}$ still falls a little bit behind (mean mPD: 11.22 mm). This observation is further backed by the significance values ($p = 0.00$ for $\mathcal{HGC}$; $p = 0.94$ for $\mathcal{TGC}$) and the rigid body parameter RMSEs in TABLE 7.4.

7.3.3. Experiments on Patient Data

Additional to the real abdominal CTA scan, two intraoperative fluoroscopy images of the same patient showing occlusion by medical instruments (FIG. 7.1(e)) were provided by our partner clinic. The data had been acquired using a fully mounted

Siemens AXIOM Artis dTA angiography suite with dynaCT software that gives information about the focus setting of the X-ray machine as well as its position relative to the patient table. With this information, we are able to calculate the ground truth projection $\mathbf{P}_{gt}$.

Again, we evaluated the robustness, accuracy, and success of the proposed disocclusion techniques in combination with a 2D-3D registration using the introduced robust similarity measures. As in the previous experiments, a total amount of 16 different cases were evaluated. The image results of the disocclusion procedures are visualized in FIG. 7.1(e-l). TABLE 7.5 shows error measures $mTRE, mPD, mRPD$ represented as mean values and minimum and maximum values of all performed test runs as well as success rate and capture range for each of the cases. For allowing a quantitative determination of the significance of the results, we also performed the *t-test* in between each two of the disocclusion techniques (including none) for each similarity measure separately. The significance values (p values) are presented in TABLE 7.6. A p value equal to or less than 0.05 is considered significant and less than 0.01 is considered very significant. As for the synthetic experiments, we calculated root mean square errors (RMSE) between ground truth values and final registration positions for each single rigid body parameter $(t_x, t_y, t_z, r_x, r_y, r_z)$ introduced in section 3.3.2 (see TABLE 7.7).

Interestingly, the robust measures $\mathcal{HGC}, \mathcal{TGC}$ perform best for the real interventional images. When only regarding the normal without any prior disocclusion technique applied, $\mathcal{HGC}$ yield a mean mPD of 31.41 mm with 99.31% successful registrations and a relatively high capture range of 10.45 mm. Although TABLE 7.6 indicates an almost significant difference in results when comparing the case without disocclusion technique and *Spline Interpolation* or *Stent Editing* ($p = 0.07$,$p = 0.08$), there is hardly any improvement visible in TABLE 7.5. *Stent Editing* even decreases the success rate from 99.31% to 85.83%. In the case of measure $\mathcal{TGC}$, only *Digital Inpainting* is able to improve the results yield by the original method without any prior disocclusion. The mean mPD value decreased from 50.77 mm to 38.29 mm with 98.61% (original: 97.92%) successful cases and capture range of 9.5 mm (original: 3.8 mm). Together with $p = 0.02$ (see TABLE 7.6), this is a significant improvement. TABLE 7.7 shows that mostly rigid body parameters contribute to this improvement as measured by the RMSEs. Similar to $\mathcal{HGC}$, although TABLE 7.6 also indicates high significant difference in results for the other disocclusion techniques (except of *Spline Interpolation* vs. *Stent Editing*), there is no improvement visible in TABLE 7.5 and TABLE 7.7. For $\mathcal{GC}$, TABLE 7.5 shows some improvement for the mean mPD values (from 67.15 mm to as less as 51.66 mm with *Stent Editing*), success rate (from 59.03 % to as much as 96.53 % with *Spline Interpolation*) and capture range (from 1.9 mm to as much as 10.45 mm with *Digital Inpainting*). This behavior is also indicated by TABLE 7.6 that shows significant differences (or near to that) for all disocclusion techniques ($p = 0.02$,$p = 0.09$,$p = 0.08$). For the calculation of success rate and capture range we chose a success threshold of 20 mm. The sudden increase in success rate an capture range indicates that mostly $mTRE$ values of more than 20 mm could be decrease to lie below the threshold. As shown by TABLE 7.7, *Stent Editing*) could reduce the RMSE for the depth translation parameter t_z which is the reason for the lower mean mPD error measure. The

Table 7.5.: Evaluation study on patient data for each similarity measure and each disocclusion technique (including the normal case where no disocclusion was performed)

	Gradient Correlation				**Gradient Difference**			
	normal	Inpainting	Poisson Editing	Spline Interpolation	normal	Inpainting	Poisson Editing	Spline Interpolation
mTRE mean (mm)	15.02	8.82	9.31	8.77	13.23	9.59	10.37	9.59
mTRE range	0.2 - 38.87	0.19 - 22.84	0.19 - 43.76	0.29 - 32.21	1.78 - 33.54	0.81 - 21.91	0.57 - 32.41	0.43 - 27.43
mPD mean (mm)	67.15	53.5	51.66	51.81	71.58	62.4	70.95	63.85
mPD range	0.69 - 273.16	0.97 - 237.55	0.3 - 188.05	1.4 - 201.12	2.83 - 295.18	1.95 - 220.78	2.39 - 273.03	2.31 - 209.7
mRPD mean (mm)	6.78	5.43	5.25	5.26	7.31	6.4	7.19	6.47
mRPD range	0.69 - 273.16	0.97 - 237.55	0.3 - 188.05	1.4 - 201.12	2.83 - 295.18	1.95 - 220.78	2.39 - 273.03	2.31 - 209.7
success rate (%)	59.03	95.83	93.06	96.53	60.41	93.75	94.44	96.53
capture range (mm)	1.9	10.45	1.9	7.6	3.8	6.65	5.7	6.65

	Huber GC				**Tukey GC**			
	normal	Inpainting	Poisson Editing	Spline Interpolation	normal	Inpainting	Poisson Editing	Spline Interpolation
mTRE mean (mm)	7.59	7.53	6.81	6.83	7.95	6.93	11.93	12.29
mTRE range	1.25 - 20.32	0.89 - 24.170	0.46 - 22.81	0.43 - 22.24	1.91 - 27.9	1.26 - 22.29	4.67 - 35.42	2.34 - 29.96
mPD mean (mm)	31.41	33.06	30.8	34.43	50.77	38.29	76.75	78.49
mPD range	2.45 - 135.11	1.51 - 120.18	0.82 - 142.56	2.44 - 126.6	15.09 - 137.81	5.59 - 140.93	19.99 - 256.2	5.74- 220.13
mRPD mean (mm)	3.18	3.35	3.12	3.49	5.18	3.89	7.89	8.07
mRPD range	2.45 - 135.11	1.51 - 120.18	0.82 - 142.56	2.44 - 126.6	15.09 - 137.81	5.59 - 140.93	19.99 - 256.2	5.74- 220.13
success rate (%)	99.31	99.31	85.83	99.31	97.92	98.61	91.67	93.06
capture range (mm)	10.45	7.6	10.45	10.45	3.8	9.5	3.8	3.8

Table 7.6.: Significance values

Gradient Correlation	Inpainting	Interpolation	Poisson Editing
original	0.02	0.09	0.08
Inpainting		0.38	0.53
Interpolation			0.80

Huber GC	Inpainting	Interpolation	Poisson Editing
normal	0.72	0.07	0.08
Inpainting		0.16	0.17
Interpolation			0.98

Gradient Difference	Inpainting	Interpolation	Poisson Editing
original	0.01	0.01	0.05
Inpainting		0.88	0.30
Interpolation			0.25

Tukey GC	Inpainting	Interpolation	Poisson Editing
normal	0.02	0.00	0.00
Inpainting		0.00	0.00
Interpolation			0.54

Table 7.7.: Mean values for estimation errors in rigid body parameters

	Gradient Correlation				**Gradient Difference**			
	normal	Inpainting	Poisson Editing	Spline Interpolation	normal	Inpainting	Poisson Editing	Spline Interpolation
t_x (mm)	12.56	10.52	10.07	9.96	9.6	9.8	10.04	7.87
t_y (mm)	6.95	5.36	5.42	5.37	6.08	5.88	6.22	6.77
t_z (mm)	25.8	23.9	28.14	24.19	21.08	19.35	21.61	22.35
r_x (degree)	0.49	0.43	0.39	0.48	0.49	0.5	0.47	0.43
r_y (degree)	0.54	0.54	0.68	0.73	0.47	0.58	0.65	0.58
r_z (degree)	0.54	0.56	0.57	0.56	0.68	0.65	0.74	0.66

	Huber GC				**Tukey GC**			
	normal	Inpainting	Poisson Editing	Spline Interpolation	normal	Inpainting	Poisson Editing	Spline Interpolation
t_x (mm)	10.31	9.2	9.23	9.2	11.13	9.62	11.23	12.83
t_y (mm)	11.01	9.53	7.34	6.78	8.62	5.1	9.54	9.02
t_z (mm)	24.37	24.49	22.11	21.63	21.53	19.83	24.35	22.01
r_x (degree)	0.61	0.59	0.47	0.48	0.64	0.5	0.5	0.5
r_y (degree)	0.17	0.14	0.37	0.35	0.45	0.38	0.93	0.94
r_z (degree)	0.13	0.13	0.16	0.19	0.22	0.19	0.4	0.41

other disocclusion techniques could improve RMSEs for the other translation parameters t_x, t_y. Although the application of $\mathcal{GD}$ measure without prior disocclusion yield a worse mean mPD value (71.58 mm) than $\mathcal{GC}$ (67.15 mm), its success rate as well as capture range is higher (60.41 $\%$ and 3.8 mm in comparison to 59.09 $\%$ and 1.9 mm). This is due to the definition of success rate and capture range that are both calculated from the $mTRE$ values. As in the case of $\mathcal{GC}$, the registration result improves when one of the three proposed disocclusion techniques is applied beforehand. This is also confirmed by TABLE 7.6 that shows p values of 0.01 for *Digital Inpainting* and *Spline Interpolation*, and 0.05 for *Stent Editing*. The largest decrease in mean mPD values can be seen for *Digital Inpainting* (62.4 mm). Surprisingly, the success rate is still higher for *Spline Interpolation* (96.53 $\%$ vs. 93.75 $\%$), although the mean $mTRE$ values are exactly the same (9.59 mm). For an explanation, we have to take into account the range of $mTRE$ values that is larger for *Spline Interpolation* meaning that more values below the presented mean (and also below the defined success threshold of 20 mm) exist.

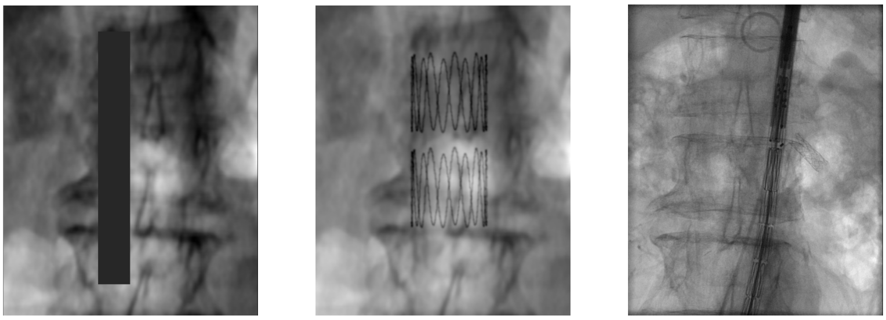

(a) Synthetic projection with thick occlusion

(b) Synthetic projection with thin occlusion

(c) Real fluoroscopy

Figure 7.3.: Image data for the analysis of $\mathcal{HGC}$ and $\mathcal{TGC}$

Table 7.8.: Analysis of behavior of Huber GC and Tukey GC for different occlusion structures

	synthetic (thick structure)			synthetic (thin structure & noise)			real		
	mTRE mean	mPD mean	mRPD mean	mTRE mean	mPD mean	mRPD mean	mTRE mean	mPD mean	mRPD mean
$\mathcal{HGC}$	6.25 mm	34.0 mm	3.5 mm	6.54 mm	39.16 mm	3.11 mm	7.59 mm	31.41 mm	3.18 mm
$\mathcal{TGC}$	3.05 mm	14.34 mm	1.5 mm	7.07 mm	41.42 mm	4.23 mm	7.95 mm	50.77 mm	5.18 mm

7.3.4. Analysis of $\mathcal{HGC}$ and $\mathcal{TGC}$

While performing the above described experiments, we made an interesting observation. Whereas, without any prior disocclusion technique applied to the interventional image, $\mathcal{TGC}$ performs better than $\mathcal{HGC}$ for the synthetic experiments in terms of all accuracy and robustness measures, the opposite is the case for the real experiments. In order to analyze the behavior of both measures for different types of occlusion and dissimilarity, we created a second synthetic projection and inserted a digital model of a stent graft disturbed by Gaussian noise (see FIG. 7.3(b)).

The structure of TABLE 7.8 corresponds to the arrangement of FIG. 7.3 showing from left to right a synthetic projection with a thick occluding structure, another projection with a thin occluding structure disturbed by Gaussian noise and thereby resembling the real case, and a real interventional fluoroscopy image. Regarding all error measures together, $\mathcal{TGC}$ results worsen the more realistic the occluding structure and the image material itself become. The largest change can be observed for the replacement of a thick occluding structure by the more realistic digital stent graft object and the addition of noise. The mean $mTRE$ value increases by 4.02 mm, the mean mPD value by 27.08 mm, and the mean $mRPD$ by 2.73 mm. As a comparison, the change from the synthetic projection with a thin and noisy occluding structure to the real image results in a change of only 0.88 mm / 9.35 mm / 0.95 mm. The mean $mTRE$ values for $\mathcal{HGC}$ also worsen with the change towards more realistic occluding structures and the image material. However, the changes in values are not as high as for tgc. For instance, the mean $mTRE$ value decreases by 0.29 mm when replacing the thick occlusion by a thin and noisy structure, and by 1.05 mm when changing to the real image material. This observation indicates that for large connected occlusions or dissimilarities in images, a registration with $\mathcal{TGC}$ yield better results than with $\mathcal{HGC}$. If perforated or unconnected occluding regions or image dissimilarities are present, $\mathcal{HGC}$ performs better than $\mathcal{TGC}$. This might be due to the different behavior of *Tukey* and *Huber M-estimators* (see Section 5.1). Whereas *Tukey* sets every outlier (result that is higher than the predefined threshold c) to 0, *Huber* includes the sign of the outlier as well as the outlier threshold k. In case of small and thin occluding regions or image dissimilarities, k can be properly chosen to resemble in some sense the occluded region such that the registration optimization is not interrupted by degraded values. For big occlusions, however, it is not possible to resemble the entire region by just one fixed value. The reason why *Tukey* performs well for the digitally inserted thick occlusion because the setting to 0 of outliers act similar as totally neglecting the occluded pixels. It is obvious that it is better rather not to take into account dissimilar regions than setting these regions to a fixed value.

Another interesting observation made in TABLE 7.8 is that, although $\mathcal{HGC}$ yields worse mean $mTRE$ results when applied to real interventional images instead of synthetic projections, the mean mPD results get significantly better in the real experiments. For an explanation, the reader is referred to Section 3.3.5 where the error measures are defined. mPD only measures the error of the projected points. If two points lie on the exact projection line, one farther away from the projection plane, they yield an $mTRE > 0$ but $mPD = 0$. Thereby it is possible that for the above mentioned case, $\mathcal{HGC}$ could bring the points nearer to the projection line, but farther away from each other in z direction.

8. Model-based Detection and 3D Recovery of Stent Shape from Angiographic Images

During the intervention, the catheter and stent position is only visualized in 2D X-ray views. This makes it highly difficult for physicians to place the stent graft in the defined position that was used to define the stent graft parameters. In general, more image acquisitions are needed during this fine positioning. In particular branching vessels need to be made visible in the images before completely unfolding the stent. A "'virtual"' visualization of the still folded or unfolding stent graft within the CTA volume would provide the physician a 3D view of the current situation. This mixed view can help ensuring the correct positioning of the stent in regard to his planned measurements. Such solutions would decrease both the need for extensive use of contrast agent and the radiation dose.

Whereas a deformable 2D-3D registration algorithm for matching abdominal vascularity extracted from preoperative CTA scans to intraoperative angiographic images is already available [57], a visualization of the stent graft in the 3D scan still requires a method for stent graft detection in 2D and correct backprojection into 3D.

In this chapter, we present a novel algorithm to match a 3D model of the stent graft to an intraoperative 2D image showing the device. The method is fully automatic and does therefore not interrupt the medical workflow. By choosing a global-to-local approach, we are able to abandon any user interaction and still meet the required robustness. The complexity of our registration scheme is further reduced by a semi-simultaneous optimization scheme and by including constraints that correspond to the geometry of the stent graft.

8.1. Stent Model

We define the stent segment model to be the curve,

$$\mathcal{M}_i(\mathbf{x}) = (a_i(\mathbf{x}), b_i(\mathbf{x}), c_i(\mathbf{x})) \tag{8.1}$$

consisting of the set of parametric equations

$$a_i(\mathbf{x}) = r_{\mathcal{M},i}(\mathbf{x}) cos(\mathbf{x}) \tag{8.2}$$

$$b_i(\mathbf{x}) = r_{\mathcal{M},i}(\mathbf{x}) sin(\mathbf{x}) \tag{8.3}$$

$$c_i(\mathbf{x}) = A_i sin(p_i \mathbf{x} + s_i) \tag{8.4}$$

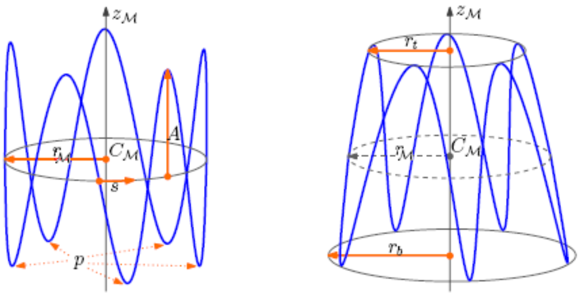

Figure 8.1.: Stent segment model with $r^t = r^b$ (left) and $r^t < r^b$ (right)

with amplitude A_i specifying the height of the segment, period p_i equal to the number of peaks, and phase shift s_i merely shifting the starting point. The radius of the stent segment model is calculated by

$$r_{\mathcal{M},i}(\mathbf{x}) = \left(1 - \frac{\sin(p_i\mathbf{x} + 1)}{2}\right) r_i^t + \frac{\sin(p_i\mathbf{x}) + 1}{2} r_i^b \tag{8.5}$$

with r_i^t and r_i^b representing the upper and lower radius as visualized in Fig. 8.1.

In our notation, an entire stent graft $\mathcal{M} = \{\mathcal{M}_1, \ldots, \mathcal{M}_l\}$ is defined as the set of l stent segments.

8.2. Automatic Feature Extraction

For an improved performance, we first apply a preprocessing procedure on the image I (see Fig. 8.4(b)) in order to outline the stent region $\mathcal{S}$ and to highlight the wire structure. Additional to the wires of the stent graft, the guide wire which is used as navigation support to the physician is also visible in the interventional X-ray images. In order for our matching algorithm to not get stuck in these outliers, we need to eliminate these pixels.

Fig. D.3 displays our preprocessing scheme. For obtaining the catheter silhouette image $\mathcal{C}$ (Fig. 8.3(a)), we employ the Frangi filter [46] for scales $5 - 6$ followed by a median filtering for noise removal in order to capture the catheter pixels.

The stent region $\mathcal{S}$ (Fig. 8.4(c)) can be extracted similarly. First, we subtract thick curvilinear structures from thin curvilinear structures (Frangi filter for scale 2) for only highlighting the stent wires. For further use, let us denote the resulting image as I_{wires} (Fig. 8.3(c)). Subsequent employment of a median filter for noise removal and mean filter for dominant region extraction leads to the desired image region that contains the stent graft. It is worth mentioning that instead of the Frangi filter, any filter can be used that highlights curvilinear structures of selected sizes.

In the end, we subtract the catheter pixels $\mathcal{C}$ from image I_{wires} and mask the result with the stent region $\mathcal{S}$:

$$I_f = (I_{\text{wires}} - \mathcal{C}) \cdot \mathcal{S}. \tag{8.6}$$

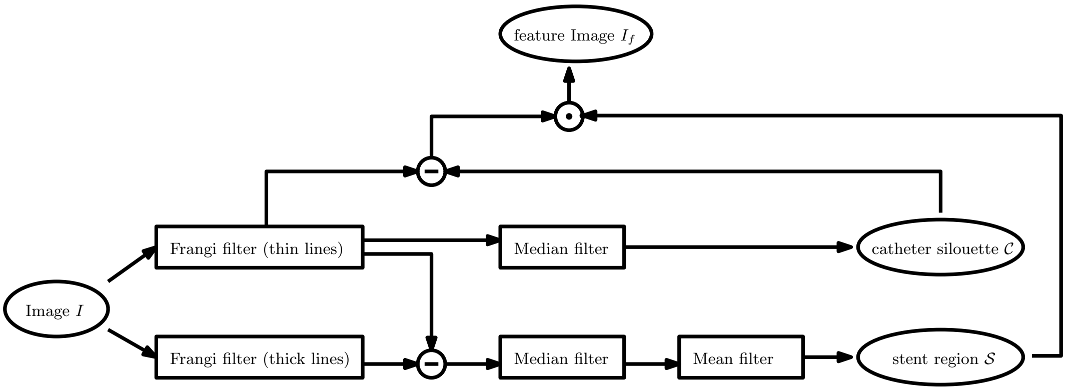

Figure 8.2.: Preprocessing scheme for an automatic computation of the feature image I_f

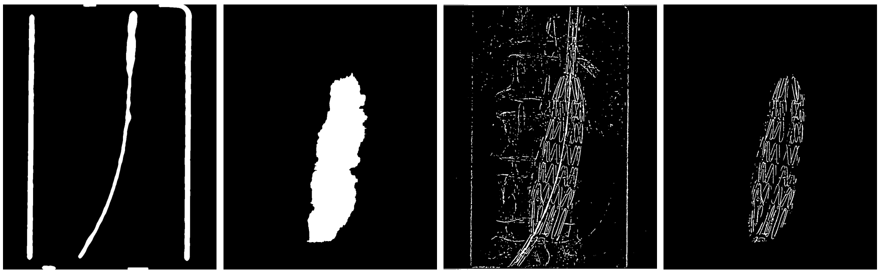
(a) $\mathcal{C}$ (b) $\mathcal{S}$ (c) I_{wires} (d) I_f

Figure 8.3.: Visualization of automatic feature extraction procedure

The resulting feature image is displayed in Fig. 8.3(d). In order to provide a distance measure for the following registration procedure, we calculate distance map D_{I_f} on feature image I_f such that each pixel $x \in D_{I_f}$ represents the distance to the next feature point (non-zero pixel in I_f).

8.3. Registration Algorithm

In order to place the model in the 2D image space of the interventional image I a projection is necessary to map the stent model $\mathcal{M}$ to the image coordinate system. Similar to 2D-3D image registration, the projection transformation $\mathbf{P} = K[R|t]$ consists of the 6-DOF extrinsic parameters $[R|t]$ for rotation and translation of the 3D volume and the 4-DOF intrinsic camera parameter K of the *pinhole camera model* [58]. For the following considerations, we assume the camera matrix K to be given by the interventional angio system.

Using all transformation and model parameters together as

$$\mathbf{p} = \{\mathbf{p}_1, \ldots, \mathbf{p}_l\}, \qquad \mathbf{p_i} = \{R_i, t_i, r_i^t, r_i^b, A_i\} \tag{8.7}$$

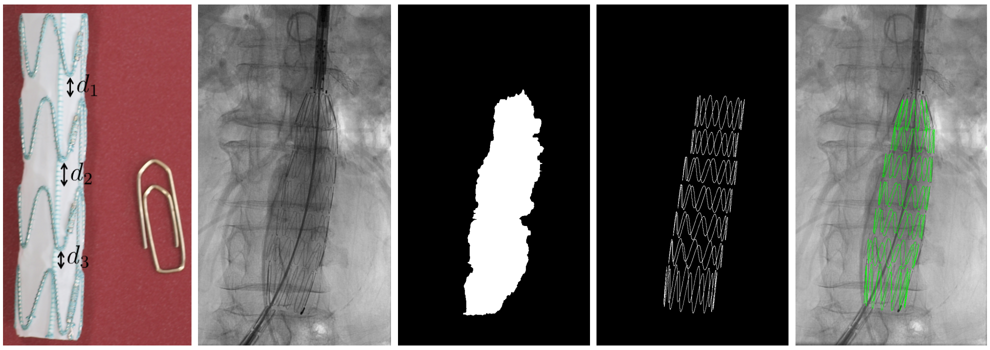

(a) (b) (c) (d) (e)

Figure 8.4.: Overview of our proposed solution (high resolution images are included in the supplemental material): (a) cut-out of an abdominal aortic stent graft, (b) fluoroscopy image commonly acquired during EVAR, (c) extraction of image region including the stent graft wires (*stent region* $\mathcal{S}$), (d) initial stent graft model $\mathcal{M}$ created from xml-file, (e) optimized stent graft model overlayed in green on interventional fluoroscopy image

the registration problem for the entire stent model can be formalized as

$$\hat{\mathbf{p}} = \arg\min_{\mathbf{p}} \sum_{i=1}^{l} \sum_{x\in\mathcal{M}_i} D_{I_f}(T_{\mathbf{p}_i}(x)) \tag{8.8}$$

where $T_{\mathbf{p}_i}(x)$ is a projection of point x of the 3D segment model $\mathcal{M}_i$ using parameters $\mathbf{p}_i$ into 2D image space. This formalization equals a simultaneous registration of all stent segment models introducing a parameter space of dimension $l \times 9$. Considering that conventional abdominal aortic stent grafts consist of more than 10 segments, the cost for optimization increases rapidly. Another drawback is introduced by many local minima in the costfunction plot, each of them belonging to one stent segment that is displayed in the image. The costfunction for the registration of the whole stent model consisting of l stent segments is

$$E(\mathbf{p}) = \sum_{i=1}^{l} \sum_{\mathcal{M}_i} I(T_{\mathbf{p}_i}(\mathcal{M}_i)) \tag{8.9}$$

where $\mathbf{p} = \{\mathbf{p}_1, \ldots, \mathbf{p}_l\}$.

A sequential fitting of each segment of a conventional aortic stent graft leads to parameter space of dimension multiple of 9. In order to reduce the complexity in our registration procedure, we use a semi-simultaneous optimization framework introduced by Sidorov et al. [127]. Instead of optimizing all parameters for all segments at once, we optimize the parameters of one segment for a certain number of iterations and then move to the next randomly chosen segment. By applying this strategy, we implicitly make use of the tubular appearance of the stent graft and constrain the pose change in between neighboring segments.

We can smoothen the costfunction plot by the inclusion of prior knowledge about the stent graft to be implanted: mean diameter, mean amplitude of the stent graft, and distance d_i between consecutive segments (see Fig. 8.4(a)). This information is default for all samples of a certain model by a certain producer and can be delivered by the vendor (i.e. in an xml file). Having this information available and setting the remaining parameters of each segment to initial values, we can model the implanted stent graft approximately and divide our registration problem in two steps. A complete description of our method in pseudo-code is given in Alg. 1.

Global registration

Here, we solve for the overall orientation of all segments in order to be very close for the local calculations. The global pose of the entire stent graft model is defined by the global parameters $K, R_{global}, t_{global}$. The angle γ_{global} for rotation around the camera's z-axis as well as the translation $t^x_{global}, t^y_{global}$ can be estimated from the stent region $\mathcal{S}$ via *principal component analysis* and center of mass detection. Therefore, only rotation around the camera's x- and y-axis and translation in along z-axis need to be optimized and hence, we define $\mathbf{p}_{global} = \{\alpha_{global}, \beta_{global}, t^z_{global}\}$.

Accordingly, let now $\mathbf{p}_i = \{\mathbf{v}_i, \mathbf{t}_i, r^t_i, r^b_i, A_i\}$ define the set of remaining parameters for each single segment i, where $\mathbf{v}_i = [\alpha_i, \beta_i, \gamma_i]^T$ represents the vector containing the three rotation angles that form rotation matrix $\mathbf{R}_i$. Setting parameter vectors $\mathbf{p}_i$ to initial values corresponding to the definitions from the xml file starting with no rotation and translation, the registration problem can be formalized as

$$\hat{\mathbf{p}}_{global} = \arg\min_{\mathbf{p}_{global}} \sum_{i=1}^{l} \sum_{x \in \mathcal{M}_i} D_{I_f}(T_{\{\gamma_{global}, t^x_{global}, t^y_{global}\} \circ \mathbf{p}_{global} \circ \mathbf{p}_i}(x)) \tag{8.10}$$

The optimal $\hat{\mathbf{p}}_{global}$ leads us to the approximated position of the stent graft in the interventional image. In the next step, we will refine the shape and position of each single segment of the stent graft.

Local registration

We aim at finding the correct values for each $\mathbf{p}_i$.Similar to Equ. (8.8) for the simultaneous registration, we define our costfunction for each segment i $(i = 1, \dots, l)$ as

$$E(\mathbf{p}_i) = \sum_{x \in \mathcal{M}_i} D_{I_f}(T_{\{\gamma_{global}, t^x_{global}, t^y_{global}\} \circ \hat{\mathbf{p}}_{global} \circ \mathbf{p}_i}(x)) \cdot \phi(\mathbf{p}_i) \cdot \phi(\mathbf{p}_{i+1}) \tag{8.11}$$

with

$$\phi(\mathbf{p}_i) = \left\| \begin{matrix} |\mathbf{t}_i - \mathbf{t}_{i-1}| - \mathbf{t}^{\Delta}_i \\ |\mathbf{v}_i - \mathbf{v}_{i-1}| - \mathbf{v}^{\Delta}_i \\ |r^t_i - r^b_{i-1}| - r^{\Delta}_i \end{matrix} \right\| + \lambda \tag{8.12}$$

penalizing the change of translation, rotation and radius in between neighboring segments. This change is constraint by the graft material fixing the stent wires (Fig.

8.4(a)) which is not stretchable. Therefore translation, rotation radii as well as the radii of the curves depend on the predefined distance d_i between the segments:

$$\mathbf{t}_i^{\Delta} = \begin{bmatrix} \frac{d_i}{2} \\ \frac{d_i}{2} \\ \frac{A_i}{2} + d_i \end{bmatrix} \qquad \mathbf{v}_i^{\Delta} = \begin{bmatrix} \frac{d_i}{\sqrt{1+d_i}} \\ \frac{d_i}{\sqrt{1+d_i}} \\ \frac{s_i}{2} \end{bmatrix} \qquad r_i^{\Delta} = |r_i^t - r_i^b|$$

In order to account for small measurement errors, an additional parameter λ was added to the penalization equation (8.12).

Algorithm 1 Stent Extraction

```
Require: Stent model $\mathcal{M} = \{\mathcal{M}_1, \dots, \mathcal{M}_l\}$, Image $I$
  $[D_{I_f}, \mathcal{C}, \mathcal{S}] = doPreprocessing(I)$
  $\gamma_{global} \leftarrow PCA(\mathcal{S})$
  $[t^x_{global}, t^x_{global}] \leftarrow centerOfMass(\mathcal{S})$
  for all $i \in \{1, \dots, n\}$ do
    $\mathbf{p}_i \leftarrow initializeSegmentParameters()$
  end for
  $\hat{\mathbf{p}}_{global} \leftarrow doGlobalRegistration(D_{I_f}, \gamma_{global}, t^x_{global}, t^x_{global}, \mathbf{p}_i)$
  while not happy do
    $i \leftarrow randomSelect(\{1, \dots, l\})$
    if first iteration then
      $\tilde{\mathbf{p}} \leftarrow \mathbf{p}_i$
    end if
    for 20 iterations do
      $\hat{\mathbf{p}}_i \leftarrow doLocalRegistration(\gamma_{global}, t^x_{global}, t^y_{global}, \hat{\mathbf{p}}_{global}, \tilde{\mathbf{p}})$
    end for
    $\tilde{\mathbf{p}} \leftarrow \hat{\mathbf{p}}_i$
  end while
```

8.4. Evaluation

Although our method can be applied to interventional X-ray images without knowing the corresponding matrix $\mathbf{P}$, a thorough validation is only possible in 3D requiring a correct calibration of the C-arm system. A possible strategy is to acquire projection images of the stent graft from two or more different views, apply our proposed method to each of the images, and compare the resulting 3D models. Therefore it is crucial that either all images are taken simultaneously or no changes to the stent graft have been made in between the different acquisitions. It is very difficult to find interventional images that fulfill these requirements as bi-planar systems are not considered state-of-the-art imaging for endovascular interventions and physicians only rarely acquire two or more images where the stent graft is in the exact same opening stage. A second approach is possible if a 3D volume of the situation (including the stent graft) is available. Then, the resulting 3D stent model can be compared to a segmentation of the stent. However for interventional cases,

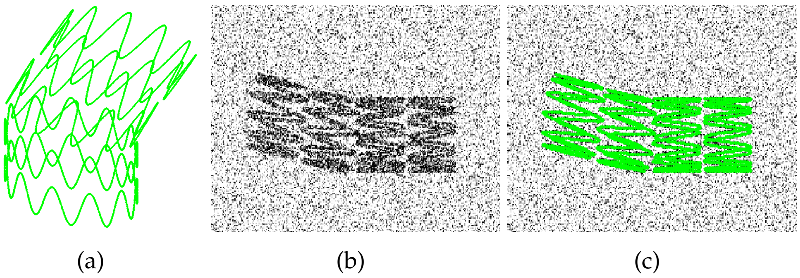
(a) (b) (c)

Figure 8.5.: Synthetic experimental data: (a) 3D digital 4-segment stent model, (b) sample image showing the model with additive Gaussian noise, (c) detection result in 2D overlayed in green

Table 8.1.: Synthetic experiments: RMS errors for each local parameter averaged over total number of included segments

	R (deg)			t (mm)			A (mm)	r^t (mm)	r^b (mm)
	$\mathbf{v}^x$	$\mathbf{v}^y$	$\mathbf{v}^z$	$\mathbf{t}^x$	$\mathbf{t}^y$	$\mathbf{t}^z$			
$\mathbf{R}_3$	0.01	0.03	0.02	0.00	0.00	0.04	0.00	0.00	0.00
$\mathbf{R}_4$	0.01	0.03	0.03	0.00	0.00	0.04	0.00	0.00	0.00
$\mathbf{R}_5$	0.02	0.04	0.04	0.01	0.00	0.05	0.00	0.04	0.02
$\mathbf{R}_6$	0.02	0.04	0.05	0.01	0.01	0.06	0.01	0.04	0.04

only pre- and (maybe) postoperative patient volumes are available that either contain no stent graft at all (preoperative) or a fully opened stent graft acquired at least 6 months after the intervention (postoperative). Due to these difficulties, we decided to quantitatively validate the accuracy of our proposed algorithm on realistic synthetic and phantom data and additionally show the impact of our method on real data.

For creating the synthetic data, we digitally produced binary volumes of size $512 \times 512 \times 512$ showing random stent graft models consisting of 3-6 segments, namely $\mathbf{R}_3, \mathbf{R}_4, \mathbf{R}_5, \mathbf{R}_6$. By applying realistic deformations to each of the segments and calculating preselected projections of the volumes, we obtain 2D images of the stent graft as well as the corresponding ground truth parameter selection.For a unique parameter selection, we added the global rotations and translations to the local parameters $\mathbf{v}_i, \mathbf{t}_i$. We estimated the average noise level of 5 interventional fluoroscopies showing an unfolded stent graft and added it to the projection images (mean 0.59 and variance 0.98). The values were found by estimating the average noise level of 5 interventional fluoroscopies showing an unfolded stent graft. Fig. 8.5 shows a synthetic image including a 4-segment stent graft and its detection result. The registration accuracy is listed in Table 8.1. As expected, the errors values are very small and show the overall impact of our method. Obviously, due to error propagation, values are slightly increasing the more segments are included in the stent model. The sudden change in error values for stent models with 4 and 5 segments are due to the fact that we only employed different top and bottom radii for $\mathbf{R}_5, \mathbf{R}_6$.

Table 8.2.: Details for phantom projection images and the comparison of recovered 3D stent model to real stent graft extracted from CT (DICE and Jaccard metric [125])

	size (pixel)	primary angle (deg) (deg)	secondary angle (deg) (deg)	DICE	Jaccard
A	478×422	18.2	20.1	0.95	0.95
B	478×422	18.2	20.1	0.95	0.95
C	478×422	18.2	20.1	0.95	0.95
D	478×422	18.2	20.1	0.95	0.95

In absence of a publicly available gold standard, we employed the following strategy to create ground truth data for reliable validation of our method. We created our own phantom consisting of the upper part of a swine's leg and inserted a half unfolded sample of a stent graft such that it lies parallel to the bone. Simulating the small catheter that is inserted prior to the stent graft, we integrated a small wire inside the stent graft sample. 10 Radio-opaque markers were sticked to the outside and inside of the box in a predefined pattern to facilitate the subsequent correspondence finding.In order to prevent deformation changes, we placed the entire phantom in a paper box and filled all empty space with insulating foam. After acquiring a 3D CT volume, we took X-ray projection images with a mobile interventional C-arm from 4 different angles. Details of the image sizes and transformations are given in Table 8.2. In absence of an available fixed angio system, we had to estimate the projection matrix for each of the 4 projection images by employing the *normalized Direct Linear Transform (DLT)* algorithm [58] on the corresponding marker positions.

Once $\mathbf{P}$ matrices were estimated, our algorithm was applied to all 4 projection images. We compared the recovered 3D models to the real stent extracted from CT. The 3D segmentation was performed using a combination of manual outlining and region growing. In order to allow for quantitative evaluation of our results, we backprojected the resulting digital stent models into CT space and created a binary volume of the exact same extent and voxel size as the phantom CT volume. Table 8.2 indicates the DICE results for each of the 4 datasets.

For the real experiments, our medical partners kindly provided a set of real interventional fluoroscopy image data (acquired by Siemens AXIOM Artis dTA angiography suite) and corresponding preoperative CTA scans. In absence of ground truth data as the stent graft is not shown within the preoperative volume, we employed the first validation strategy as explained in the beginning of this section. Provided that the C-arm system is correctly calibrated, the amplitude and top and bottom radii of two corresponding segments acquired from different views must be equal up to a common scaling factor. As the angiography system used by our clinical partners is not biplanar, deformation changes need to be taken care of by the experimental setup. In the lower abdominal part of the human body, the aorta and iliac arteries are not exposed to breathing or other organ specific motion and the pulsatile motion originating from the blood pressure is ne-

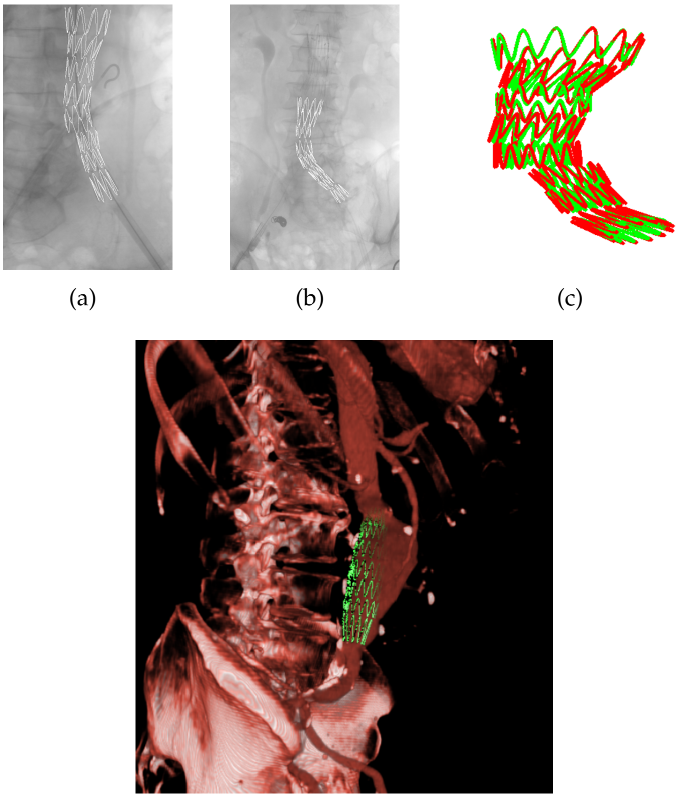

(a) (b) (c)

(d)

Figure 8.6.: Real experiment: (a)-(b) detection results (white) overlayed onto interventional images acquired from two different views, (c) 3D recovery of both stent shapes (green,red) after applying a common scale to all green segments

glectable [73]. The deformation that is induced by the stent graft itself, however, is very significant [35], but can be eliminated by acquiring both images in the same opening stage of the stent graft. Visual results are given in Fig. 8.6. For the combined plot of both models (Fig. 8.6(c)), we applied a common scale of 7.91 to each segment's amplitude and top and bottom radii of the stent model shown in red color. The scale value represents the mean ratio of final values for amplitude and top and bottom radii for each of the 8 segments and yields a root mean square error in model point positions of 2.1 mm. Resulting offsets for the local parameters $(\mathbf{v}^x, \mathbf{v}^y, \mathbf{v}^z, \mathbf{t}^x, \mathbf{t}^y, \mathbf{t}^z, A, r^t, r^b)$ are $(-7.1deg, -6.3deg, -5.4deg, \approx 0.0mm, \approx 0.0mm, \approx 0.0mm, -0.8mm, 0.2mm, 0.6mm)$.

9. Conclusion

After having presented the novelties introduced by our work, we would like to conclude this thesis with a summary and an outlook to future work that emerges from our contributions.

9.1. Summary

An abdominal aortic aneurysm (AAA) is an enlargement of the abdominal aorta, resulting from weakened arterial walls. As preventive treatment procedure, the conventional open surgery has been more and more replaced by endovascular aortic repair (EVAR) due to its minimally invasive nature. In contrast to a complete opening of the patient's abdomen, a stent graft is inserted via an introducer system through one femoral artery into the aneurysmatic aorta excluding the aneurysm sack from the circulation and reducing the pressure on the aortic wall. Once completely unfolded, misplacements of the stent graft lead to partial or total cut-offs of blood supply of vitally important organs and will lead to a life-threatening emergency surgery. Hence, the short and long-term effects of EVAR highly depends on the accurate positioning of the stent graft [60]. An appropriate visualization and advanced image guidance could help improving the difficult situation for the physician as well as increase the cure chance for the patient.

In this thesis, we have presented new approaches to computer-assistance for endovascular abdominal aortic repair. By a fusion of the preoperative high-resolution 3D patient scan and the interventional images, it is possible to bring missing 3D information about the patient's vasculature into the intervention room. A subsequent image-based detection of the stent graft in the interventional image and its simultaneous recovery in 3D makes it possible to further visualize the device in its current position within the preoperative volume.

Our proposed registration algorithms are able to handle difficult image dissimilarities introduced by occluding medical instruments in the images. We have introduced robust similarity measures *Huber Gradient Correlation* and *Tukey Gradient Correlation* and have shown that these are able to improve accuracy and robustness of registration algorithms for matching an intraoperative C-arm cone beam CT data to a preoperative CTA volume of the same patient.

Compared to robust similarity measures that perform an outlier reduction for registration algorithms, disocclusion aims at reconstructing the image in the occluded region while retaining the physical model of the image. This is realized by disocclusion-based 2D-3D registration that we have presented in this thesis. Two novel disocclusion techniques, namely *Spline Interpolation* and *Stent Editing*, have been introduced and incorporated into a medical registration framework. In order to be able to perform a comparative study, we also combined the existing*Digital Inpainting* disocclusion method as well as four different gradient-based similarity measures into the same framework. During experiments of the algorithms on synthetic data as well as real clinical images, we detected an ambiguity of our proposed measures *Huber Gradient Correlation* and *Tukey Gradient Correlation*. In a subsequent analysis, it was discovered that the performance of these measures highly depend on the shape and structure of the occlusion.

In order to complete our research and make our methods applicable for practical usage, we have presented a method for detection of the stent graft in intraoperative 2D images. We have thereby shown for the first time that an image-based detection of the prosthesis and simultaneous visualization within a volume rendering of the patient scan is possible. The method is fully automatic and does therefore not interrupt the medical workflow. By an automatic preprocessing and choosing a global-to-local registration approach, we are able to abandon any user interaction and still meet the desired robustness. Our method . The complexity of our registration scheme is reduced by applying constraints that correspond to the geometric model of the stent graft, and a semi-simultaneous optimization strategy.

9.2. Future Work

In this thesis, we have presented new approaches to computer assistance for EVAR. Although our methods are self-contained, the results point to several interesting directions for future work.

9.2.1. Deformable Registration

Although the abdominal aorta is not subject to breathing motion nor to any other specific organ motion, deformation changes are possible induced by the rigid medical instruments, in particular the stent graft itself. There have been several approaches suggested for deformable 2D-3D registration of vessels in general [57] and of the aorta in particular [85, 117]. However, all of them assume to have angiographic 2D images available where the aorta is equally contrasted. This requires additional contrast injections as due to the large extents of the aorta, the contrast dissolves quickly.

As the abdominal aorta is not subject to breathing motion or any other organ specific motion and the only deformation that happens interventionally is induced by rigid medical devices, another option is to additionally use the information given by the inserted instruments such as the catheter or the stent graft itself. These devices are visible in both angiographic and fluoroscopic images and describe roughly the outline of the vessel, e.g. its centerline. Once the stent graft is completely unfolded, the inner vessel wall can be estimated by transforming the stent into a tubular structure, e.g. a centerline with cross sectional disks representing the radius. In contrast to existing methods, this approach takes into account only a limited but important region within the aorta and deformable registration could therefore be performed more efficiently.

9.2.2. Image-based Tracking of Stent Graft

The opening of a stent graft inside the abdominal aorta is performed under continuous fluoroscopic guidance resulting in a sequence of images capturing different stages of the opening procedure. In this thesis, we have presented a method for accurate 2D detection of the stent graft and simultaneous recovery of its shape in 3D from one single intraoperative 2D image. Having a fluoroscopic sequence available showing several opening stages of the stent graft, the detection and recovery result of a previous frame could serve as initialization for the launching of our method in the next frame. By constraining possible deformation changes in between consecutive frames, efficient image-based tracking of the stent graft could be realized. With the simultaneous recovery in 3D, the actual position and shape of the stent graft could be visualized in the preoperative patient scan. This would allow the physician to directly control the correct positioning of the stent graft such that it correctly covers the aneurysm while not occluding any branching vessels. Moreover, the extracted deformation of the device can directly be applied to the preoperative patient scan allowing an immediate deformable 2D-3D registration of the aorta as discussed in the previous section 9.2.1.

9.2.3. Realistic Deformation Constraints for Virtual Stenting

The possibility of digitally simulating the insertion of a stent inside a blood vessel prior to the intervention and thereby being able to do more accurate measurements and treatment planning, has ever been a strong desire of physicians. Research on *virtual stenting* have emerged from recent advances in simulating biomechanical behavior of organs and anatomy. Existing methods [45, 81, 37] describe the digital stents by cylindrical simplex meshes [30] that model the deformation by second-order partial differential including internal and external forces. Additional constraints calculated from the geometric and mechanical characteristics of the stent also contribute to the deformation simulation. Such an approach is valid for bare-metal intracranial or coronary stents (see appendix A for more detail), however, not for endovascular stent grafts that consist of two different material and has therefore different behavior.

Another common issue of all existing approaches is the unavailability of a concrete description how stent deformation is constraint by degenerated arterial walls. Performing our proposed method for 2D detection of a stent graft and simultaneous recovery of its shape in 3D on a sequence of interventional images showing a complete opening of the stent graft (see section 9.2.2) would result in a series of 3D stent graft models simulating the real deformation in interaction with the anatomy. Extracting such deformation models from a population of patients would provide a basis for in-depth analysis of stent graft deformation and its interaction with degenerated vessel walls. Integrating this knowledge into virtual stenting procedures could provide to the physician a more realistic environment for treatment planning and might eventually broaden the range of aneurysms that can be treated by EVAR.

Appendix

A. Medical Stents

Although many people associate the word "stent" to a prosthetic device used in human medicine, it goes back to the English dentist Charles Stent who invented a material to form dental impression compounds in 1856. The plastic surgeon Jan Esser used the exact same material to craft forms for facial reconstruction and named it "Stent's material" after its inventor [120]. It is difficult to follow an exact line through history, but somehow the expression "stent" ended up being a synonym for some kind of prosthesis replacing or supporting parts of the body structure [59].

In the next two sections, we outline the different shapes of various medical stents. We also describe in detail the differences of certain vascular stents and stent grafts crucial for this thesis.

A.1. Stent Designs

Medical stents are implanted into various anatomical structures and organs. Their design changes with the requirements a supporting prosthesis must fulfill for certain anatomical locations. A selection of different stents in shown in Fig. A.2. *Airway stents* (see Fig. A.1(a)[1]) are built of metal or silicone in a variety of sizes with and without covering providing physicians with many options in managing airway obstructions. A *ureteral stent* (see Fig. A.1(b)[2]) is a thin, flexible tube threaded into the ureter to help urine drain from the kidney to the bladder or to an external collection system. *Prostatic stent* (see Fig. A.1(c)) are used to keep open the male urethra and allow the passing of urine in cases of prostatic obstruction and lower urinary tract symptoms. A *duodenal stent* is placed to prop open an obstruction in the duodenum (first section of the small intestine) which may allow fluid and food to pass more easily and also to keep the duodenum from becoming obstructed again. An *esophageal stent* (see Fig. A.1(d)[3]) is placed at a point of narrowing or blockage to open up the esophagus to help the patient swallow or drink.

The most widely known is the vascular stent placed inside a blood vessel to prevent, or counteract, a disease-induced, localized flow constriction. Also here, its de-

---

[1] From NYU Medical Center, Department of Cardiothoracic Surgery, Division of Thoracic Surgery. Available at `http://www.med.nyu.edu/cvsurgery/thoracic/patientcare/technology/airway.html`.

[2] Bander Ureteral Diversion Stent Set by Cook Medical. Available at `http://www.cookmedical.com/uro/dataSheet.do?id=4870`.

[3] Ultraflex™ Esophageal NG Stent System by Boston Scientific. Available at `http://www.bostonscientific.com/Device.bsci?page=HCP_Overview&navRelId=1000.1003&method=DevDetailHCP&id=10005791&pageDisclaimer=Disclaimer.ProductPage`.

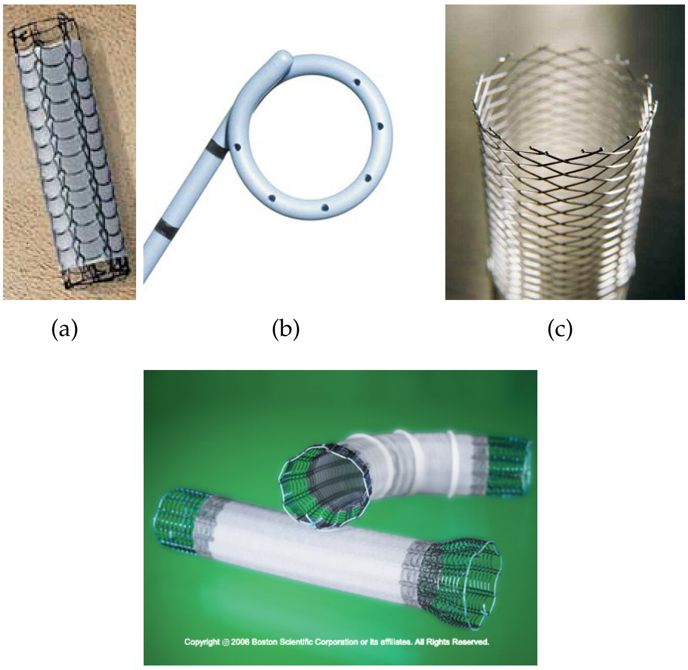

(a) (b) (c)

(d)

Figure A.1.: Stent Designs: (a) covered metal airway stent, (b) urinary stent, (c) prostatic or urethric stent, (d) esophageal stent

sign varies depending on the blood vessel this stent is inserted in. A more detailed analysis on the different designs is given in the following section A.2.

The recent advancements in stent technology have lead to featured devices. Covered with palladium, a *radioactive stent* limits excessive cell growth of the inner membrane of the blood vessel and prevent restenosis. However, because of the constant radiation that is exposed, the use of such stents is not according to radiation protection laws of most countries. Eliminating this drawback, a *drug-eluting stent* is coated with a pharmacologic agent (drug) that is known to interfere with the process of restenosis (reblocking). More recently, a new generation of stents has been introduced. Healing stents are coated with antibodies that attract ingrowth cells of the vessel wall. That way the stent mesh is being covered more quickly and this decreases the risk for restenosis.

A.2. Stent vs. Stent Graft

Vascular stents and *stent grafts* exist in various shapes and configurations depending on the type of blood vessel and kind of disease. Whereas coronary and carotid stents are solely made from metal webs or meshes (see Fig. A.2(a)[4]), (endovascular) stent

---

[4] TAXUS®Express$^{2\mathrm{TM}}$ Atom$^{\mathrm{TM}}$ Paclitaxel-Eluting Coronary Stent System. Available at `http://bostonscientific.mediaroom.com/index.php?s=13&cat=14&mode=gallery:53`.

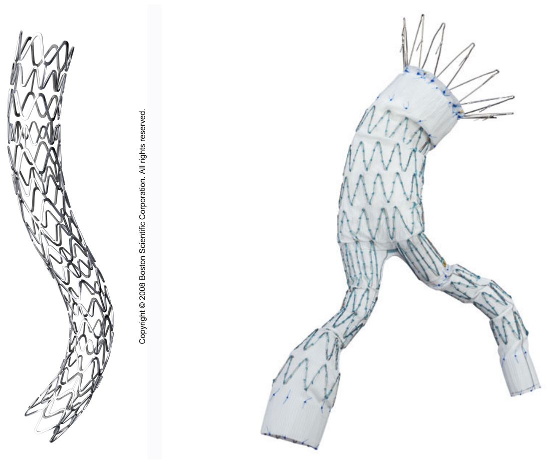

(a) (b)

Figure A.2.: Different design and material: (a) stent, (b) stent graft

grafts (see Fig. A.2(b)[5]) are composed of a synthetic fabric tube (graft) supported by a rigid structure (stent).

Stent grafts used for EVAR usually consist of two or three parts: Either a main body and two legs, or a trunk component (including one of the legs already) and a contra-lateral leg component. The legs are supposed to sit in the iliac arteries, and are frequently referred to as limbs. Various sizes and configurations are available from different vendors, and, additionally to the commercial ones, custom-made stent grafts can be obtained. The components are folded up in order to fit into delivery catheters, and are capable of expanding to the pre-established diameter when placed and released in the artery.

---

[5] Zenith Flex by Cook Medical. Available at `http://www.cookmedical.com/ai/home.do`.

B. AAA-Thrombus Segmentation

For diagnosis and detection of AAA, CTA[1] is the standardized imaging modality. Whereas the aortic lumen is highlighted by injected contrast agent and has strong gradient values to surrounding structures, the aortic wall and aneurysm thrombus are visually very hard to detect without any anatomical expertise (Fig. B.1(a)). Additional difficulties for segmentation algorithms are introduced by severe calcification occurrence inside the thrombus (Fig. B.1(b)).

For allowing an optimal treatment planning of AAAs, the focus of medical as well as engineering research goes towards integrating biomechanical models in the medical workflow. In the current clinical environment, the geometric information of the abdominal aneurysm model is defined by a manual segmentation performed by the surgeon himself. However, this is highly time-consuming and requires a lot of expertise. For these reasons, semi-automatic methods are urgently needed.

In this chapter, we present a hybrid deformable model approach for segmentation of the thrombus in an abdominal aortic aneurysm. Having a presegmentation of the aortic lumen available, our method constructs a deformable model on the lumen boundaries and drive its deformation towards the thrombus boundaries. The energy functional that is minimized during deformation, integrates local as well as global image information and combines it with additional shape constraints. By the use of cubic B-Spline surfaces as deformation model and distance functions, existing gaps in the boundary gradient are overcome and segmentation leakage into adjacent objects is prevented.

In the last decade, several approaches have been published for AAA segmentation. **Subasic et al.** [130] divides the segmentation into two tasks. The inner aortic boundary outlines the blood filled lumen and is segmented by an edge-based geometric deformable model and subsequent morphological postprocessing to obtain the segmented surface. In order to obtain a surface of the outer aortic boundary that defines the vessel wall, the authors utilize a-priori knowledge about the aortic shape to reconstruct low-contrast portions of the aorta including the outer boundary. The slice-wise knowledge-based preprocessing is followed by another run of the edge-based geometric deformable model and subsequent morphological postprocessing already used for segmenting the inner boundary. The method was tested on 12 patient datasets showing tubular AAAs of different shapes and sizes. However, AAAs that cover branching vessels or the aortic bifurcation were not included in the experiments. For the segmentation of the aortic lumen and the thrombus at once, **Zhuge et al.** [147] propose to combine a geometric deformable model with a support vector machine (SVM) classifier evaluating the likelihood that a given voxel is part of the aneurysm. The SVM is trained with voxel location, intensity, and

---

[1] CTA - Computed Tomography Angiography

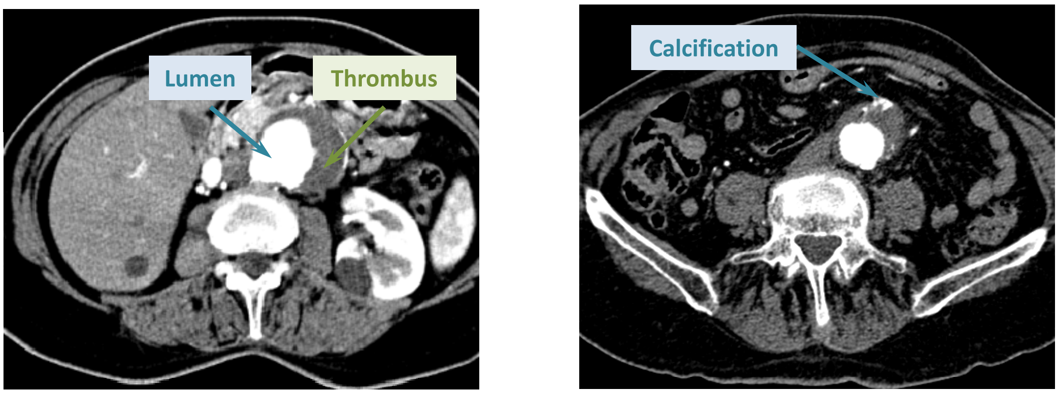

(a) (b)

Figure B.1.: Abdominal Aortic Aneurysm

texture features. Compared to other approaches, the initializing of the defomable model is completely automatic. In order to ease the restriction of purely gradient-based approaches to have well defined object boundaries available, Olabarriaga et al. [102], de Bruijne et al. [29], and Zhuge et al. [147] additionally use a-priori information about the intensity texture of aneurysms to drive the model deformation. Such statistical deformable models indeed give valuable results for AAA segmentation, however, they heavily depend on the quality and quantity of presegmented training sets.

Our method is inspired by the approach of Huang et al. [64] that deforms a model in a common variational framework using both boundary and region information. As a non-parametric kernel-based approximation of the intensity distribution is used, no prior training of classifiers is required. Initially published for application to ventricle segmentation, this method gives good results. For the application to aneurysm thrombus segmentation, we adapted the energy functional to be better adapted to the shape and intensity characteristics of AAAs. In contrast to the free form deformation model used by Huang et al., our approach uses B-Spline surfaces to model the deformation. Thereby, we allow non-uniform distribution of control points that gives stronger smoothness constraints that are modeled locally. Additionally, as our data sets are of big size, we reach a better performance with our deformation model. It needs much less evaluations due to the smaller amount of control points. In the following section, we describe our method in more mathematical detail.

B.1. Segmentation Algorithm

B.1.1. Deformation Model

In this section, we aim at deforming a model $\mathbf{M}$ initialized at the aortic lumen boundary, towards the correct boundaries of an abdominal aortic aneurysm.

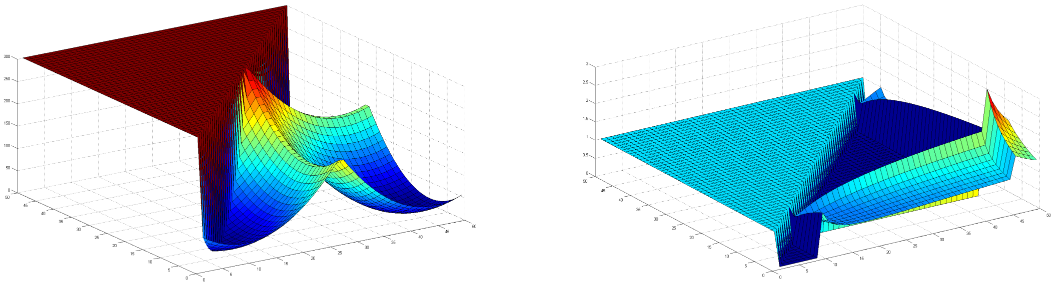

(a) Energy function E_{local} of a simple model (b) Energy function E_{prop} of a simple model

Figure B.2.: Simulation of energy functions

Thereby our deformation model

$$\mathbf{M}(u,v) = \frac{\sum_{i=0}^{N}\sum_{j=0}^{M}\mathcal{N}_{i,p}(u)\mathcal{N}_{j,q}(v)\mathbf{p}_{i,j}}{\sum_{i=0}^{N}\sum_{j=0}^{M}\mathcal{N}_{i,p}(u)\mathcal{N}_{j,q}(v)w_{i,j}} \tag{B.1}$$

is described as a conventional NURBS surface [113] with bidirectional control grid $\mathbf{p}$, nonrational B-spline basis functions $\mathcal{N}$, and weights w.

The model is deformed by adding a displacement vector $\mathbf{f}_{i,j}$ to each control point $\mathbf{p}_{i,j}$. We express this deformation by $\mathbf{M}(u,v) \circ \mathbf{f}$.

We use the following notation with our deformable model $\mathbf{M}$:

$\mathcal{R}_\mathbf{M}$	is the image region enclosed by the model.
$\Omega\backslash\mathcal{R}_\mathbf{M}$	represents the image background.
$\delta\mathcal{R}_\mathbf{M}$	is a narrow band of width δ at the model boundary.

B.1.2. Information Representation

Our approach combines local and global information about the object to be segmented.

The local shape image Φ_{local} contains edge information and enforces the model to deform towards existing image gradients. Therefore, we first extract the edges $\mathbf{E}$ in the original image $\mathbf{I}$. Then

$$\phi_{local}(x) = d(x, \mathbf{E}(\mathbf{I})) \tag{B.2}$$

is represented by the euclidean distance d from each voxel x to the nearest edge point of $\mathbf{E}(\mathbf{I})$.

The global shape image Φ_{global} incorporates information on intensity statistics and drives the model deformation towards statistic region boundaries. Therefore, we sample a few intensity values belonging to the aneurysm thrombus and represent the model texture using a mixture of j Gaussians (Gaussian Mixture Model) each defined by mean μ_j and standard deviation σ_j. Then, the probability density function of a voxel x belonging to the aneurysm region $\mathcal{R}$ is

$$p(x|\mathcal{R}) \quad = \quad \sum_{j=1}^{M}\frac{1}{\sqrt{2\pi}\sigma_j}\exp(-\frac{(x-\mu_j)^2}{2\sigma_j^2})P(j) \tag{B.3}$$

with $P(j)$ presenting the prior probability that pixel x was generated by component j and where $\sum_{j=1}^{M} P(j) = 1$. Applying this pdf to all image voxels, a probability image $\mathbf{P}$ is created. After edge extraction, the global shape image reads

$$\phi_{global}(x) = d(x, \mathbf{E}(\mathbf{P})) \tag{B.4}$$

where every voxel represents the euclidean distance d from each voxel x to the nearest edge point of $\mathbf{E}(\mathbf{P})$.

B.1.3. Model Evolution

The deformation of our model $\mathbf{M}$ is driven by the minimization of an energy functional that is to be explained in detail in this subsection. The different parts of the energy functional make use of the precomputed shape images that were described in the previous subsection.

$$E = \alpha E_{local} + \beta(E_{global} + bE_{prop}) \tag{B.5}$$

The local energy term encourages the model to go along the "geodesic" path, which is the smooth shortest path connecting the two open ends of a gap:

$$E_{local} = \frac{1}{MN} \int_u \int_v (\phi_{local}(\mathbf{M}(u,v) \circ \mathbf{f}))^2 dudv \tag{B.6}$$

Weighting parameter α controls the influence of this term to the overall deformation energy. Fig. B.2(a) shows a plot of this energy for different displacements of the model control points. As one can easily observe, this energy incorporates steep rises and falls and will converge extremely fast to the minimum if initialized correctly.

The global energy term enforces the model deformation towards the edges of the probability image and also chooses the geodesic path to overcome possible gaps.

$$E_{global} = \frac{1}{MN} \int_u \int_v (\phi_{global}(\mathbf{M}(u,v) \circ \mathbf{f}))^2 dudv \tag{B.7}$$

Weighting parameter β controls the influence of this term to the overall deformation energy. Besides the different shape images, the terms (B.6) and (B.7) are constructed in a very similar way and the characteristics of their plots are very similar.

The last energy term used is the maximum likelihood intensity data term, written as

$$E_{prop} = -\frac{1}{MN} \int_u \int_v log\mathbf{P}(\mathbf{I}(\mathbf{M}(x) \circ \mathbf{f})|\mathcal{R}) dudv \tag{B.8}$$

It forces the model to deform towards areas of high probability. The plot of this energy is visualized in Fig. B.2(b). The flat area in the center matches with the homogeneous region inside the aneurysm.

Algorithm 1

```
procedure HybridAAASeg($\mathbf{I}$,$\mathbf{S}_l, t$) return $\mathbf{S}_a$
    $s \leftarrow getThrombusSamples(\mathbf{I})$
    $pde \leftarrow calculateGMM(s)$
    $\mathbf{I} \leftarrow fillLumen(\mathbf{I}, \mathbf{S}_l, pdf)$
    $\mathbf{P} \leftarrow calculatePropImage(\mathbf{I}, pdf)$
    $\mathbf{S} \leftarrow \mathbf{S}_l$
    for all chosen scales of $\mathbf{I}$ do
        $downscale(\mathbf{I})$
        $downscale(\mathbf{P})$
        $scale(\mathbf{S})$
        $initializeModel(\mathbf{M}, \mathbf{S})$
        $(\phi_{local}, \phi_{global}) \leftarrow computeShapeImages(\mathbf{I}, \mathbf{P})$
        $setScaleParameters(\alpha, \beta, b, \lambda)$
        $\mathbf{f} \leftarrow \mathbf{0}$
        while not converged do
            $\mathbf{f}' \leftarrow \mathbf{f} - \lambda \frac{\partial E}{\partial \mathbf{f}}$
            if $|E(\mathbf{f}') - E(\mathbf{f})| < t$ then
                converged
            end if
            $\mathbf{f} \leftarrow \mathbf{f}'$
        end while
        $\mathbf{M}' \leftarrow \mathbf{M} \circ \mathbf{f}'$
        $\mathbf{S} \leftarrow recomputeSegImage(\mathbf{M}')$
    end for
    $\mathbf{S}_a \leftarrow rescale(\mathbf{S})$
end procedure
```

Figure B.3.: Pseudocode for AAA segmentation algorithm

B.1.4. Processing the AAA segmentation

The overall segmentation algorithm *HybridAAASeg* is demonstrated in Fig. B.3. The algorithm requires as input the volume scan **I**, a presegmentation of the aortic lumen S_l, and a value t for the convergence criterion. In order to approximate the Gaussian Mixture Model for the thrombus intensity distribution, some thrombus voxels need to be selected manually ($getThrombusSamples(\mathbf{I})$).

Before computation of all required shape images, the original image scan needs to be adapted to contain valid gradient and texture information. The lumen interior contain high intensity values that do not belong to the intensity distribution of the thrombus. If we compute the shape images with the original scan, our deformation model would be attracted to the high gradients introduced by the aortic lumen boundary. Therefore, we need to fill the lumen voxels with the mean value of the thrombus intensity distribution ($fillLumen(\mathbf{I}, \mathbf{S}_l, pdf)$).

For more accurate results, we use a multiresolution gradient-descent optimization technique. Therefore, all energy parameters and additional optimization parameters need to be defined for each of the chosen scales ($setScaleParameters(\alpha, \beta, b, \lambda)$). At the end of each scale optimization, the deformed model needs to be transferred into a binary volume **S**. Eventually, the resulting segmentation volume is rescaled to the original configuration.

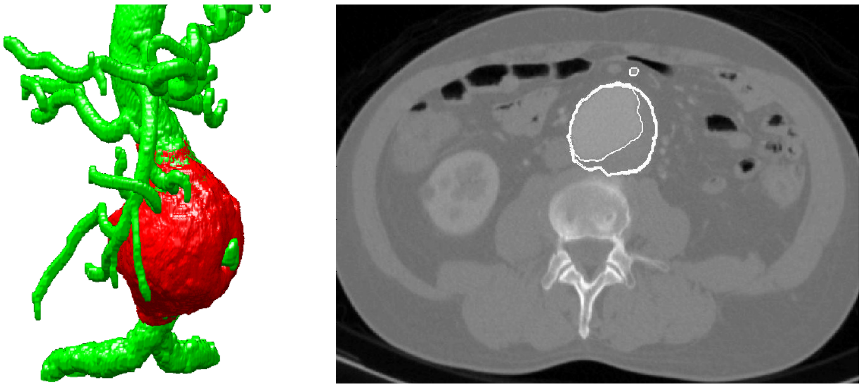
(a) (b)

Figure B.4.: Results: aortic lumen and aneurysm thrombus in (a) 3d and (b) slice visualization

For each scale iteration, the local and global shape images $\phi_{local}, \phi_{global}$ are computed as explained within section B.1.2 employing a Canny edge extraction algorithm.

Except of the selection of thrombus samples in $getThrombusSamples(\mathbf{I})$ and the specification of scale parameters in $setScaleParameters(\alpha, \beta, b, \lambda)$, the presented algorithm is fully automatic.

B.2. Evaluation

For evaluation purposes, we tested our proposed segmentation method on 10 preoperative CTA datasets of varying size 200x200x200-400 and voxel size 0.59x0.59x1.00-2.00 mm. The choice of parameters for each scale is given in the following table.

resolution	α	β	b	λ
1:4	2.5	2	200	4
1:2	1	2	4	400
1:1	1	1	4	900

Table B.1.: Choice of parameters for selected scales

For 5 images, ground truth segmentation data was available and could be used for quantitative evaluation measures such as overlap ratio (OR), sensitivity (S_n), and specificity (S_p). The mean values of those evaluation measures over all 5 datasets are given in table B.2. As one can clearly see, our proposed algorithm gives very promising results.

The remaining 5 results were used for qualitative evaluations performed by medical experts. They were all satisfied by the results that were in most cases consid-

OR	S_n	S_p
0.9316	0.9354	0.9837

Table B.2.: Average evaluation values for comparison with ground truth

ered as optimal. Non-optimal results occurred at bifurcation points where branching vessels were surrounded by thrombus. Those cases require manual refinement of the segmentation. According to the medical experts, this minor postprocessing interaction is still acceptable. They concluded that this implementation is of high significance for the medical workflow and medical research.

C. SASOMI - An Intuitive GUI for AAA-Thrombus Segmentation Refinement

Many clinical applications involve exact segmentation of anatomical structures in all kind of 3D images. When automatic methods fail to meet the required robustness, user interfaces that allow for refining automatic segmentation results are of great help for the medical staff.

For diagnosis and detection of AAA, CTA is the standardized imaging modality. The aortic lumen is highlighted by injected contrast agent and has strong gradient values to surrounding structures. The aortic wall and aneurysm thrombus, however, are visually very hard to detect without any anatomical expertise. Additional difficulties for segmentation algorithms are introduced by severe calcification occurrence inside the thrombus.

For allowing an optimal treatment planning of AAAs, the focus of medical as well as engineering research goes towards integrating biomechanical models in the medical workflow. In order to give realistic simulation results, the geometry of the aneurysm and its thrombus need to be extracted as accurate as possible. In the last decade, several approaches have been published allowing fully- or semi-automatic AAA segmentation (e.g. [34, 102]). Despite of their promising results, it has been shown that in clinical practice, these methods fail to provide the required robustness.

Graphical user interfaces for segmentation of anatomical structures have become extremely popular in clinical practice. Here, a variety of commercial and non-commercial software is available for general usage[1] [141] as well as for specific medical applications [74]. In the case of abdominal aortic aneurysms a CTA scan consists of up to 1000 slices. Therefore a segmentation tool needs to support some kind of interpolation in-between the slices as well as post-refinement possibilities, to improve usability. Furthermore intensity region growing is not applicable as a semi-automatic approach, since the ROIs are not always surrounded by clear and closed contours. To the best of our knowledge, there is no such refinement software available for the segmentation of AAAs.

In this chapter, we present an interactive graphical user interface that provides for the medical staff an intuitive solution for refining an automatic AAA presegmentation. The software transforms the presegmented volume in a NURBS surface providing an intuitive way of interacting with already present segmentation.

---

[1] Materialise, *Mimics*, http://www.materialise.com/mimics

C.1. General Software Design

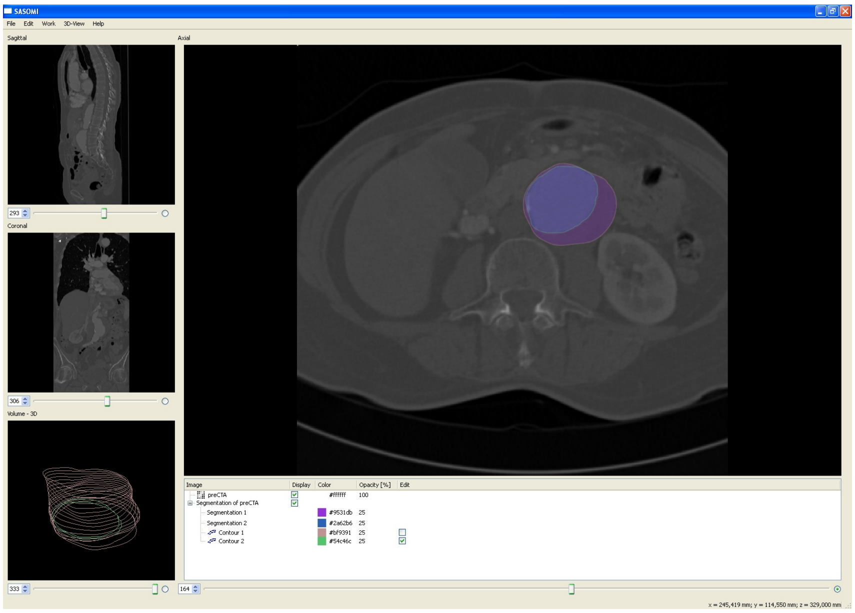

Image	Display	Color	Opacity [%]	Edit
preCTA	☑	#ffffff	100	
Segmentation of preCTA	☑			
Segmentation 1		#9531db	25	
Segmentation 2		#2a62b6	25	
Contour 1		#bf9391	25	☐
Contour 2		#54c46c	25	☑

x = 245,419 mm; y = 114,550 mm; z = 329,000 mm

Figure C.1.: The overall layout of SASOMI software

As displayed in Fig. C.1, the software consists of four different views: Axial, Sagittal, Coronal and Volume - 3D. While each of the first three gives a slice based view of the loaded image according to its direction, the Volume view shows a 3D visualization of the segmentation that can be zoomed and rotated. The segmentation tree underneath the main view offers possibilities to change color and opacity of all segmentations. In the following, we describe some of SASOMI's main features that also represent its main contributions.

Tracing: In addition to free-hand-drawing of a contour in a 2D slice, SASOMI supports edge tracing that simplifies following the outline of an edge using edge detection. While in tracing mode, edge points that are detected in the nearby area of the mouse pointer are displayed as yellow dots [Fig. 2]. To refine an already present contour it is possible to start tracing at one point of the contour and finish at second point. The part in between will then be substituted by the new one. Erasing the last drawn points can be done by drawing backwards. Thanks to edge detection it is not necessary to hit these points exactly.

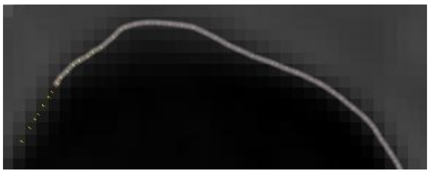

Figure C.2.: Edge tracing

Slice Interpolation: Since it is quite time-consuming to do segmentations on every slice, SASOMI computes a NURBS surface [113] from already segmented slices which is then used to generate the missing slices in-between. It also closes gaps in segments that lie within the same slice. Already segmented slices are transformed into a NURBS curve for a more accurate and smoother visualization. Of course, an interpolation is not always perfect. Therefore the next two functions can be used to optimize the result.

Edge Fitting: To refine the interpolation result this function fits the segmented points to the closest edge found in the image. The calculation of the edge points itself uses a quadratic 2D facet model on the gradient image. Compared to region growing one could consider the contour resulting from the interpolation as a seed which is in most cases already quite close to the actual gradient in the image. Accordingly a lot less comparisons are needed and the given shape also helps the algorithm to stay in a certain boundary.

Directional Edge Fitting: A more enhanced version of the popular Edge Fitting method. Edge points are captured only in the approximate direction of the curve's normal [Fig. 3a]. In addition, a search along the new edge is performed and while points that are not likely to be part of this edge are removed, missing edge points are included. The result will then be transformed into a NURBS curve [Fig. 3b]. Compared to the standard Edge Fitting method it can return more accurate results especially in corners.


(a) (b)

Figure C.3.: Edge fitting

Render 3D Model: As displayed in Fig. C.4, SASOMI allows volume visualizations in three different ways. The slices currently drawn in the Axial view as well as the calculated NURBS surface are displayed as 3D solid volume and axial 2D curves. The first one actually shows the segmented slices as they will be used for export. So even if the volume calculation should be incorrect for some slices, this shows the current state of the segmentation.

(a) (b) (c)

Figure C.4.: Rendering

C.2. Special Refinement Features

C.3. Evaluation

The SASOMI software was implemented in C++ using a Qt-based User Interface and OpenGL as graphics engine. We tested its robustness and user friendliness in a set of different experiments. We asked three engineers and three medical doctors to evaluate the software in two steps. The first task consisted of loading an abdominal CTA scan of a patient suffering from AAA and segmenting the AAA thrombus manually with the help of the given interaction tools. Secondly, these presegmentations were mixed and each user was given one segmented volume created by a different user. They were then asked to use our software to refine this segmentations. The evaluation results are presented in Fig. D.5. The users had to rank the software in each category in numbers 1 (bad) to 10 (excellent).

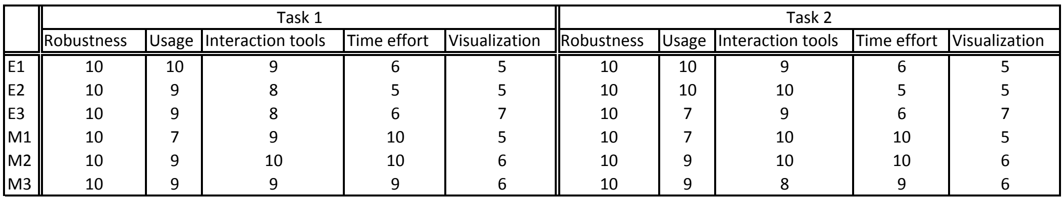

	Task 1					Task 2				
	Robustness	Usage	Interaction tools	Time effort	Visualization	Robustness	Usage	Interaction tools	Time effort	Visualization
E1	10	10	9	6	5	10	10	9	6	5
E2	10	9	8	5	5	10	10	10	5	5
E3	10	9	8	6	7	10	7	9	6	7
M1	10	7	9	10	5	10	7	10	10	5
M2	10	9	10	10	6	10	9	10	10	6
M3	10	9	9	9	6	10	9	8	9	6

Figure C.5.: Evaluation

While the other categories were found to be good to excellent, all users complained about the insufficient volume views. All medical doctors stated that such a volume view of the segmentation does only make sense within a volume rendering environment of the surrounding anatomical structure. The engineers criticized the missing mesh visualization that would make more sense for accessing the geometry in detail.

To test the improvement of interaction time, gained by using the implemented functions, we selected several persons with different level of experience considering the use of graphics software or SASOMI itself. While beginners are users with little or no experience, three users in our test are working as graphic- or web designers. Both got a short introduction in the program's user interface. The persons called experts are using SASOMI already for several weeks.

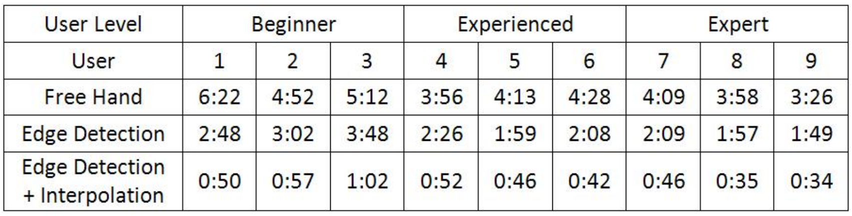

User Level	Beginner			Experienced			Expert		
User	1	2	3	4	5	6	7	8	9
Free Hand	6:22	4:52	5:12	3:56	4:13	4:28	4:09	3:58	3:26
Edge Detection	2:48	3:02	3:48	2:26	1:59	2:08	2:09	1:57	1:49
Edge Detection + Interpolation	0:50	0:57	1:02	0:52	0:46	0:42	0:46	0:35	0:34

Figure C.6.: Interaction time

The task was to segment an object over 20 slices using the different functions the program provides. It is quite obvious that edge detection already accelerates the segmentation process. In addition the variance of the results between the different users is reduced. With interpolation it was enough to process only every fifth slice. The interpolation time of 0.7 seconds for this scenario is already included in the results. It should also to be mentioned that even with nurbs surfaces interpolation does not produce perfect results for every object. Edge fitting can then be used to reduce the effort of refinement.

D. Quantification of Abdominal Aortic Deformation after EVAR

Causes for organ deformation in the human body can generally be classified in three main groups: breathing, organ specific motility (i.e. colon motility), and external forces applied by medical instruments. While the first two have been studied intensively in many publications, the latter is still unknown due to the big variety of instruments and different biomechanical characteristics of the organs. In this work, we propose a method for quantifying the deformation of the abdominal aorta due to a graft prosthesis that is the number one treatment for aneurysms.

Quantification of abdominal aortic deformation is an important requirement for the evaluation of endovascular stenting procedures and the further refinement of stent graft design. During endovascular aortic repair (EVAR) treatment, the aortic shape is subject to severe deformation that is imposed by medical instruments such as guide wires, catheters, and, the stent graft. This deformation can affect the flow characteristics and morphology of the aorta which have been shown to be elicitors for stent graft failures and be reason for reappearance of aneurysms.

We propose a method for extracting and quantifying the specific deformation of the aorta after EVAR. It segments both preoperative and postoperative aortic structures with minimal user interaction and automatically extracts the region of interest around the aneurysm. To this end, the centerlines of both structures are extracted and reduced to the region of interest around the aorta. After an initial rigid registration, non-linear registration of the structures provides pure deformation fields of the aorta. Our method was tested by evaluating 15 datasets of patients that had been treated by EVAR.

D.1. Methodology

Our method for quantifying the aorta's deformation due to stent grafts has the following structure:

1. Rigid registration of preoperative and postoperative scan,
2. Segmentation and preprocessing of preoperative aortic shape,
3. Non-rigid registration.

D.1.1. Rigid registration

As our two CTA volumes contain severe dissimilarity introduced by the high intensities of the stent graft (see Fig. D.1), an appropriate similarity measure needs to

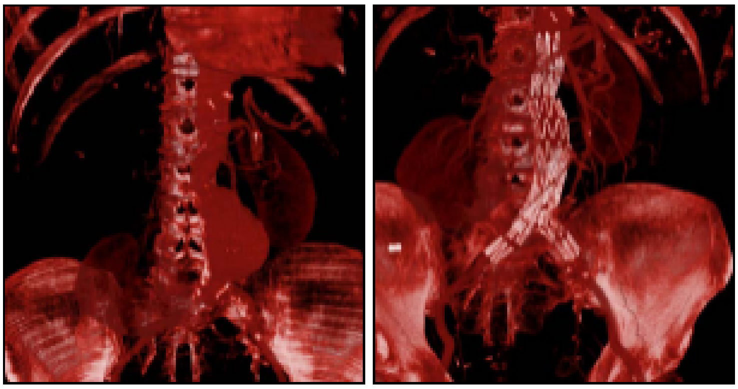

Figure D.1.: Volume rendering of preoperative and postoperative CTA patient scan

be chosen carefully.

We opted for an approach brought up by [33], where dissimilarities are not evaluated by the similarity measure. Let **S** denote a segmentation of the stent graft derived from the postoperative scan by thresholding. The adapted normalized cross correlation (A-NCC) measure only evaluates those voxels that are not part of segmentation **S**.

$$A - NCC(I^F, I^M) = \frac{\sum_{\substack{x \in I^F \cap I^M \\ x \notin \mathbf{S}}} (I^F(x) - \bar{I}^F)(I^M(x) - \bar{I}^M)}{\sqrt{\sum_{\substack{x \in I^F \cap I^M \\ x \notin \mathbf{S}}} (I^F(x) - \bar{I}^F)^2 \sum_{\substack{x \in I^F \cap I^M \\ x \notin \mathbf{S}}} (I^M(x) - \bar{I}^M)^2}} \tag{D.1}$$

with $\bar{I}^F$ and $\bar{I}^M$ representing the mean values in the overlapping regions of the fixed and moving image.
The resulting optimal transformation $\mathbf{T}_{opt}$ that maximizes A-NCC for our pre- and postoperative scans describes the overall rigid body transformation. For our following explanations, we set $\mathbf{I}^M := \mathbf{T}_{opt} * \mathbf{I}^M$.

D.1.2. Segmentation and preprocessing

As we aim to compute the deformation of the aorta induced by the inserted stent graft, the datasets need to be focused to a part of the aortic structures that incorporates only this deformation. We segment the contrasted vessel tree out of the preoperative as well as the postoperative volume using the connected threshold segmentation method provided by ITK[1]. The resulting structures contain many different deformation fields as branching vessels of the aorta scatter in the entire abdominal region. A non-rigid registration of the entire abdominal vessel trees would hence result in a displacement field including several abdominal motions and deformations, not only these of the aorta. The aorta without its branching vessels, however, represents a tubular structure that does not provide unique optimal values

---

[1] Insight Toolkit, http://www.itk.org

for the rotational parameter during registration. Therefore, we developed an algorithm that automatically creates a centerline structure for a desired region around the aneurysm. The user just needs to indicate the position of the aortic bifurcation.

In Fig. D.2, Algorithm 1 describes the overall outline of our preprocessing procedure. As input, it requires a segmentation S of the abdominal vessel tree and a point bif for the aortic bifurcation. First, topological thinning is processed onto S resulting in a centerline structure C for the entire abdominal vessel tree. Then, the root $seed$ of the aortic centerline is calculated by Algorithm 2. Here, the biggest connected component of segmented pixels in the first slice of the segmentation image is computed by counting neighboring pixels of values other than 0. The centerline voxel nearest to the center of mass of the biggest component (assumed to be the aortic lumen) is then taken as seed point. In order to further narrow the information down to the region of interest around the aorta, the centerline structure C is processed by an adapted wave front propagation algorithm shown in Algorithm 3. It adapts the wave propagation approach of [143] by stepping down the aortic centerline from a given seed point $seed$ in region growing manner until the indicated bifurcation bif is reached. At all other bifurcations, our algorithm automatically finds the path belonging to the aorta by comparing the different angles between the connecting parts. The aortic path usually continues in the direction that forms the smallest angle with the previous direction. The branching paths are included into the aortic centerline data only up to the next bifurcation respectively. Thereby, we ensure a fully three-dimensional tree structure T which can be used to cover a full transformation including rotation. Finally, we compute a Danielsson distance map [28] D on the reduced centerline data.

D.1.3. Non-rigid registration

We aim at extracting the deformation that a stent graft imposes to the preoperative aorta, by applying a non-rigid registration procedure to the pre- and postoperative three-dimensional structures. The non-rigid registration problem for the entire abdominal region, however, is highly ill-posed due to several different and independent deformations and motions that are present in these scans. Instead of a displacement field computed from original data, we perform the alignment on single segmented structures that are likely to contain the aortic deformation only. In our case, due to the aneurysm sack present in the preoperative aortic structure, a displacement field computed on the pre- and postoperative segmentation data would include a shrinking deformation whereas in reality, an inserted stent graft models the aortic wall. The preprocessing steps presented in section D.1.2, narrow down the scatter of the abdominal vessel tree to one centerline including the aorta and small parts of all branching vessels.

In order to define the energy $\mathcal{E}$ for centerlines, correspondences of pre- and postoperative centerline points are required. Except of the bifurcation points, it is highly costly to establish correspondences for the other points on the centerlines. We avoid the necessity of correspondences by computing distance maps D^F, D^M on the reduced centerline images and computing the sum of absolute differences

$$\mathcal{E}(\mathbf{D}^F, \mathbf{u} \circ \mathbf{D}^M) = \sum_x |\mathbf{D}^F(x) - \mathbf{u} + \mathbf{D}^M(x)| \tag{D.2}$$

as dissimilarity measure.

D.1.4. Quantification of deformation

With initial rigid registration (section D.1.1) and final non-rigid-registration (section D.1.3), we have obtained the linear and non-linear part of the overall transformation of the abdominal aorta. However, according to [149], deformation fields that are computed by a local nonlinear registration algorithm, still contain a linear transformation $\mathbf{T}_{local} = \mathbf{T}_{linear} \circ \mathbf{T}_{nonlinear}$. In order to obtain a pure non-linear deformation field, the authors suggest to minimize the norm of the displacement field $\mathbf{u}$ of the nonlinear component $\mathbf{T}_{nonlinear}$ with respect to the linear transformation $\mathbf{T}_{linear}$.

$$\min_p \mathcal{E}(\mathbf{T}_{linear}) = \min_p \frac{1}{n} \sum_{i=1}^{n} \| \mathbf{X}_i - \mathbf{T}_{linear}^{-1}(\mathbf{Y}_i) \|^2 \tag{D.3}$$

where $\mathbf{X}$ defines a control point grid of size n over $\mathbf{T}_{global}(I^M)$ and $\mathbf{Y} = \mathbf{X} + \mathbf{u}$ presents the deformed control point grid. As we are only interested in the deformation of the aortic shape, the optimizer needs only to evaluate those displacement positions that belong to the aorta. Once the optimal linear transformation $\mathbf{T}_{linear}$ is computed, we obtain the corresponding minimal displacement field by

$$\mathbf{u}_{minimal}(\mathbf{X}) = \mathbf{T}_{linear}^{-1}(\mathbf{Y}) - \mathbf{X} \tag{D.4}$$

For computational deformation quantification, the mean, maximal, and minimal distance of k selected deformation points can directly be accessed via the displacement field $\mathbf{u}_{minimal}$:

$$meanD(k, \mathbf{u}) = \frac{1}{k} \sum_{i=1}^{k} \| \mathbf{u}_i \| \tag{D.5}$$

$$maxD(k, \mathbf{u}) = \max_{1 \leq i \leq k} \| \mathbf{u}_i \| \tag{D.6}$$

$$minD(k, \mathbf{u}) = \min_{1 \leq i \leq k} \| \mathbf{u}_i \| \tag{D.7}$$

D.2. Evaluation

Experiments have been conducted on 15 patient datasets each consisting of one preoperative and one postoperative CT Angiography (CTA) scan. All images were acquired by a Siemens Somatom Sensation 64 scanner at our partner clinic. The reconstructed image resolution is 0.54 x 0.54 x 1.00 mm.

The preprocessing and remodeling were evaluated visually by comparing the reduced centerline structures. Fig. D.3 shows image results of each preprocessing step. In Fig. D.4(a) and D.4(b), reduced centerline structures of the pre- and postoperative scans are displayed. For obtaining correct deformation results, it is crucial that both trees have the same amount of bifurcations.

As we deal with real medical images, there is no ground truth data available that could be used for the assessment of the registration accuracy. Therefore, we reconstruct centerlines out of the deformed distance maps and evaluate these to the preoperative and postoperative lines. Next to a visual evaluation of the registration error, we choose to use the euclidean distance between the centerlines before and after non-rigid registration.

Fig. D.5(a) shows the evaluation results. For each of the 15 datasets the *initial distance* and *final distance* each presented by their maximal and mean value. Additionally, the initial and final values for the mean μ, variance σ^2, and standard deviation σ over all datasets are given. Our method results in reduced values (*final distance*) for the distance in between the respective shapes. This states that the deformed centerline fits better to the entire shape of the postoperative centerline after non-rigid registration.

The visual assessment of registration accuracy was performed by three experts from our partner medical centers. Two interventional radiologists and one vascular surgeon were asked to evaluate four different visualizations of the non-rigid registration results (see Fig. D.6(a) - D.6(d)) and compare these to visualizations given by existing rigid registration frameworks [33]. While the vascular surgeon had no experience with interventional registration systems, the interventional radiologists had been working with mounted interventional angiography suites before and were, therefore, familiar with rigid registration frameworks. All experts agreed on the importance of visualizing the deformation of the aorta during endovascular interventions and found our visualizations as highly beneficial especially for the difficult task of placing the stent graft very accurately inside the aneurysm. It turned out that, for assessing the registration accuracy, all experts investigated the position of all branching and bifurcation points rather than the position of all centerline points. They argued that the positioning of the stent graft is oriented toward the branching vessels and aortic bifurcation in order to make sure that they are not occluded by the graft. All experts were very satisfied with the accuracy in these important points. In contrast to the vascular surgeon to whom the branching vessels were of no importance, the interventional radiologists were also interested in the accuracy of especially the renal arteries as these are often included within the stent graft as side branches. However, as our approach highly concentrates on the aortic trunk and only takes small parts of branching vessels into account for rotational orientation purposes, branching vessels might not be accurately aligned (see Fig. D.4(d)). All physicians found visualizations as shown in Fig. D.6(d) as highly necessary. It displays an already deformed aortic shape within the original preoperative scan. This evaluation is very important for improvements of stent graft design because it highlights the impact of mechanic forces of the stent graft onto the aortic wall.

Algorithm 1

```
procedure PREPROCESSING($S, bif$)
    $C \leftarrow topolThinning(S)$                          ▷ centerline creation by topological thinning
    $seed \leftarrow findSeed(C, firstSlice(S))$             ▷ calculation of seed point for reduction of centerline
    $T \leftarrow adaptedWaveProp(C, seed, bif)$             ▷ reduction of centerline from seed point to bifurcation
    $D \leftarrow euclidDistanceMap(T)$                      ▷ euclidean distance map of reduced centerline
end procedure
```

Algorithm 1

```
procedure FINDSEED(C,s) return seed
    $max \leftarrow 0$
    for all $(x, y) \in s$ do
        if s(x,y) $= 1$ then
            $R \leftarrow regionGrowing(s, s(x, y))$
            if $max < size(R)$ then
                $max \leftarrow size(R)$
                $center \leftarrow centerOfMass(R)$
            end if
        end if
    end for
    $queue \leftarrow center$
    while notfound do
        $c \leftarrow queue$
        $nlist \leftarrow neighbours(c, s)$
        for all $n \in nlist$ do
            if $C(n) \neq 1$ then
                $queue \leftarrow n$
            else
                $seed \leftarrow n$
                $found$
                $stop$
            end if
        end for
    end while
end procedure
```

Algorithm 2

```
procedure ADAPTEDWAVEPROP(C,s) return T
    $min \leftarrow 180$
    $prev \leftarrow 0$
    $nlist \leftarrow neighbours(s, C)$
    $s \rightarrow T$
    $prev \leftarrow s$
    $s \leftarrow nlist(0)$
    while $s \neq bif$ do
        $s \rightarrow T$
        $nlist \leftarrow neighbour(s, C)$
        $direction \leftarrow s - prev$
        for all $n \in nlist \wedge n \neq prev$ do
            if $angle(direction, n-s) < min$ then
                $min = angle(direction, n - s)$
                $prev \leftarrow s$
                $s \leftarrow n$
            end if
        end for
        for all $n \in nlist \wedge n \neq s$ do
            $t \leftarrow n$
            $blist \leftarrow neighbours(t, C)$
            while $size(blist) \neq 3$ do
                for all $b \in blist \wedge b \neq prev$ do
                    $b \rightarrow T$
                    $t \leftarrow b$
                end for
                $blist \leftarrow neighbours(t, C)$
            end while
        end for
    end while
end procedure
```

Figure D.2.: Preprocessing and remodeling: Algorithm 1 shows general outline, Algorithm 2 and 3 describe the single steps in detail.

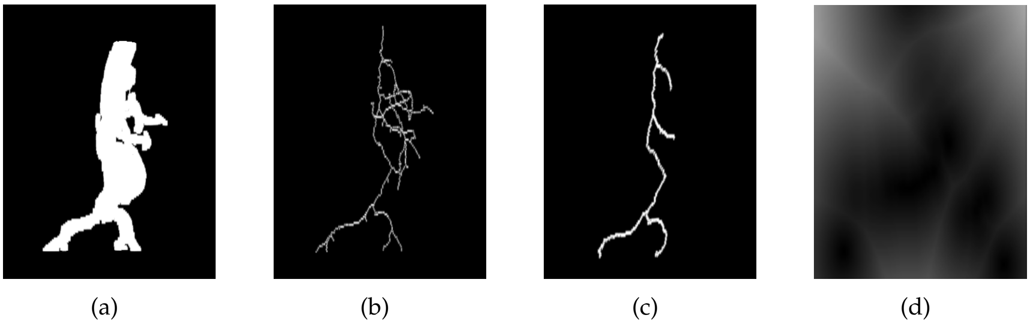
(a) (b) (c) (d)

Figure D.3.: Results of preprocessing and remodeling: (a) initial segmentation of contrasted abdominal vessel tree, (b) complete centerline structure derived by topological thinning, (c) reduced centerline structure concentrating on important region around the aneurysm, (d) final distance map.

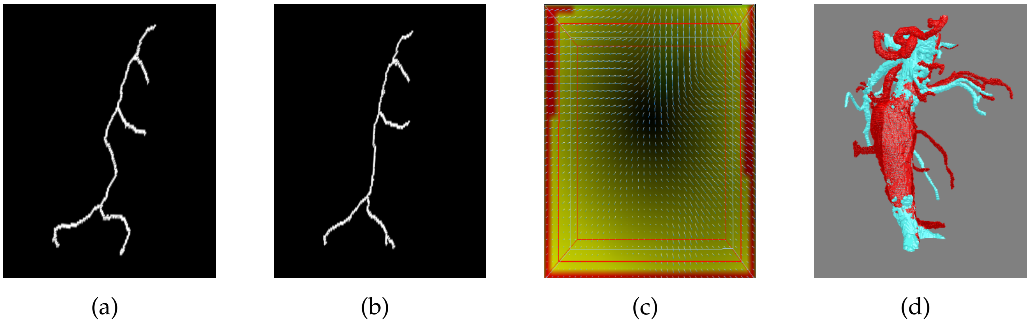
(a) (b) (c) (d)

Figure D.4.: Comparison of reduced centerline structures: (a) preoperative tree, (b) postoperative tree. Registration results: (c) final displacement quivver; (d) deformed preoperative shape (red/dark) overlayed on postoperative shape (blue/light)

	initial distance		*final distance*		*bifurcation distance*			
	max	*mean*	*max*	*mean*	*bif1*	*bif2*	*bif3*	*bif4*
Dataset 1	11,56	3,46	5,22	1,14	6,91	-	6,90	5,45
Dataset 2	14,13	5,41	4,35	1,41	4,97	3,29	7,08	12,90
Dataset 3	29,68	5,27	6,77	1,50	2,89	3,99	4,39	11,61
Dataset 4	15,46	4,17	2,15	1,32	5,45	4,69	3,67	5,45
Dataset 5	16,96	5,41	4,73	1,14	10,23	9,92	7,37	3,38
Dataset 6	10,35	4,46	3,42	1,31	1,02	2,33	4,5	12,84
Dataset 7	11,21	4,27	4,11	1,60	12,45	11,31	11,13	5,92
Dataset 8	12,26	4,17	3,10	1,32	3,06	5,48	4,32	20,32
Dataset 9	17,44	4,46	3,56	1,24	15,78	12,95	11,52	3,05
Dataset 10	19,91	3,41	4,05	1,41	14,1	10,09	9,64	4,12
Dataset 11	26,00	5,27	7,41	1,50	13,77	10,14	10,58	2,43
Dataset 12	15,60	3,17	2,09	1,22	5,09	7,55	6,32	8,88
Dataset 13	9,55	3,46	4,45	1,14	3,01	4,99	4,12	13,83
Dataset 14	16,22	5,11	4,07	1,51	1,45	4,5	3,77	9,28
Dataset 15	13,08	5,27	3,10	1,50	3,78	6,32	4,51	10,74
μ	15,96	4,45	4,17	1,35	6,93	6,97	6,65	8,68
σ	5,66	0,81	1,47	0,15	4,99	3,34	2,83	5,06
σ^2	32,01	0,66	2,17	0,02	24,92	11,17	8,03	25,61

(a)

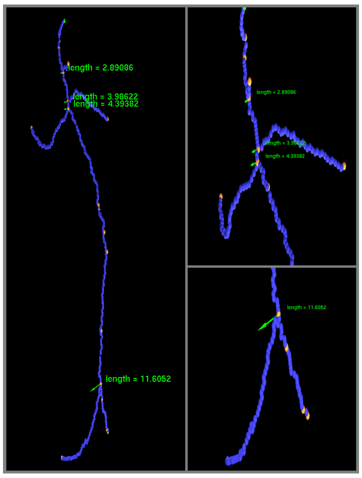

(b)

Figure D.5.: Evaluation results: (a) Accuracy of non-rigid-registration algorithm; (b) Quantification of aortic deformation.

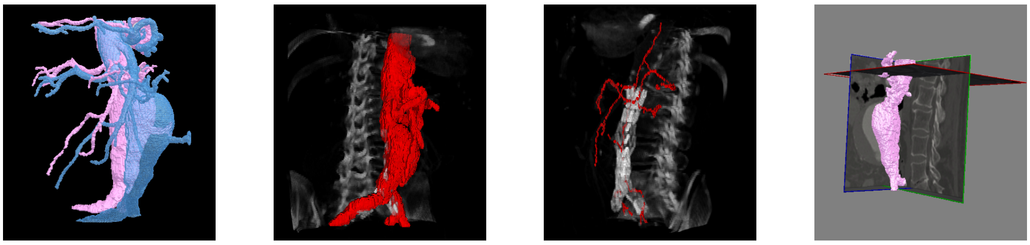

(a) (b) (c) (d)

Figure D.6.: Visual evaluation: (a) deformed preoperative shape overlayed over the original; (b) deformed preoperative shape visualized inside postoperative scan; (c) deformed preoperative centerline integrated within postoperative scan; (d) deformed preoperative shape visualized within preoperative scan.

E. Abbrevations

Medical Terms

AAA	Abdominal Aortic Aneurysm
CPB	Cardiopulmonary Bypass
CT	Computed Tomography
CTA	Computed Tomography Angiography
DICOM	Digital Imaging and Communications in Medicine
DSA	Digitally Substracted Angiography
EVAR	Endovascular Aortic Repair
FDG	^{18}F-Fluorodesoxyglucose
HU	Hounsfield Unit
MRI	Magnetic Resonance Imaging
MRA	Magnetic Resonance Angiography
PACS	Picture Archiving and Communications System
PC-MRA	Phase Contrast Magnetic Resonance Angiography
PET	Positron Emission Tomography
TOF	Time Of Flight
US	Ultrasonography

Technical Terms

2D	2-dimensional (spatial)
3D	3-dimensional (spatial)
4D	4-dimensional (3 spatial and 1 time dimension)
ASM	Active Shape Model
CCD	Charged Coupled Device
CPU	Central Processing Unit
DOF	Degree Of Freedom
DRR	Digitally Reconstructed Radiograph
GLSL	OpenGL Shading Language
GPU	Graphics Processing Unit
IGS	Image Guided Surgery
RLE	Runlength Encoding

F. List of Publications

Journals and Conference Proceedings

F. Manstad-Hulaas, G. A. Tangen, S. Demirci, M. Pfister, S. Lydersen, T. A. Nagelhus Hernes. Endovascular Image-Guided Navigation - Validation of Two Volume-Volume Registration Algorithms. Accepted to *Minimally Invasive Therapy & Allied Technologies*, 2011.

M. Emmersberger, S. Demirci, R. Ghotbi, N. Navab. SASOMI: Semi-Automatic Segmentation Of Medical Images. In Proc. *Bildverarbeitung fuer die Medizin* (BVM), Aachen, Germany, 14-16 March, 2010.

S. Demirci, G. Lejeune, N. Navab. Hybrid Deformable Model for Aneurysm Segmentation. In Proc. *IEEE International Symposium on Biomedical Imaging: From Nano to Macro* (ISBI), Boston, Massachusetts, USA, June 28 - July 1, 2009.

M. Baust, S. Demirci, N. Navab. Stent Graft Removal for Improving 2D-3D Registration. In Proc. *IEEE International Symposium on Biomedical Imaging: From Nano to Macro* (ISBI), Boston, Massachusetts, USA, June 28 - July 1, 2009.

S. Demirci, F. Manstad-Hulaas, N. Navab. Extracting a Purely Non-Rigid Deformation Field of a Single Structure. In Proc. *Bildverarbeitung fuer die Medizin* (BVM), Heidelberg, Germany, 22-25 March, 2009.

S. Demirci, F. Manstad-Hulaas, N. Navab. Quantification of Abdominal Aortic Deformation after EVAR. In Proc. *SPIE Medical Imaging*, Orlando, Florida, USA, 7-12 February, 2009.

S. Demirci, O. Kutter, F. Manstad-Hulaas, R. Bauernschmitt, N. Navab. Advanced 2D-3D Registration for Endovascular Aortic Interventions: Addressing Dissimilarity in Images. In Proc. *SPIE Medical Imaging*, San Diego, California, USA, 16-21 February, 2008.

O. Kutter, S. Kettner (=Demirci), E.U. Braun, N. Navab, R. Lange, R. Bauernschmitt. Towards an Integrated Planning and Navigation System for Aortic Stent-Graft Placement. In Proc. *Computer Assisted Radiology and Surgery* (CARS), Berlin, Germany, 27-30 June, 2007.

Patents

Prof. N. Navab, O. Kutter, S. Demirci. A Method for Registration of Medical Images Containing Image Dissimilarities. 2007E26012 DE / 200801209

Bibliography

[1] N. J. M. Aarts, G. W. H. Schurink, L. J. Schultze Kool, P. J. Bode, J. M. van Baalen, J. Hermans, and J. H. van Bockel. Abdominal aortic aneurysm measurements for endovascular repair: Intra- and interobserver variability of CT measurements. *Eur J Vasc Endovasc Surg*, 18:475–480, 1999.

[2] K. Arya, P. Gupta, P. Kalra, and P. Mitra. Image registration using robust M-estimators. *Pattern Recogn Lett*, 28:1957–1968, 2007.

[3] A. L. Baert, editor. *Encyclopedia of Diagnostic Imaging*. Springer, 2008.

[4] B. T. Baxter, M. C. Terrin, and R. L. Dalman. Medical management of small abdominal aortic aneurysms. *Circulation*, 117(14):1883–1889, 2008.

[5] H. G. Beebe. Late failures of devices used for endovascular treatment of abdominal aortic aneurysm: What have we learned and what is the task for the future? *Perspect Vasc Surg Endovasc Ther*, 14(1):29–49, 2001.

[6] M. Bertalmio, G. Sapiro, V. Caselles, and C. Ballester. Image inpainting. In *Proc. SIGGRAPH*. ACM Press, 2000.

[7] P. J. Besl and N. D. McKay. A method for regsitration of 3D shapes. *IEEE Trans Pattern Anal*, 14(2):239–256, 1992.

[8] L. Biasi, T. Ali, R. Hinchliffe, R. Morgan, I. Loftus, and M. Thompson. Intraoperative DynaCT detection and immediate correction of a type 1a endoleak following endovascular repair of abdominal aortic aneurysm. *Cardiovasc Intervent Radiol*, 32:535–538, 2009.

[9] C. A. Binkert, H. Alencar, J. Singh, and R. A. Baum. Translumbar type ii endoleak repair using angiographic CT. *J Vasc Interv Radiol*, 17(8):1349–1353, 2006.

[10] W. Birkfellner, R. Seemann, M. Figl, J. Hummel, C. Ede, P. Homolka, X. Yang, P. Niederer, and H. Bergmann. Fast DRR generation for 2D/3D registration. In *Proc. Int Conf Medical Image Computing and Computer Assisted Intervention (MICCAI)*, volume 3750 of *LNCS*. Springer, 2005.

[11] W. Birkfellner, R. Seemann, M. Figl, J. Hummel, C. Ede, P. Homolka, X. Yang, P. Niederer, and H. Bergmann. Wobbled splattinga fast perspective volume rendering method for simulation of x-ray images from CT. *Phys Med Biol*, 50 (9):N73–N84, 2005.

[12] J. Bismuth, C. Karmonik, N. Kleiman, M. Valderràbano, and A. B. Lumsden. Future imaging and guidance for endovascular procedures. In T. J. Fogarty and R. A. White, editors, *Peripheral Endovascular Interventions*, pages 479–492. Springer, 3rd edition, 2010.

[13] J. D. Blankensteijn, S. E. de Jong, M. Prinssen, A. C. van der Ham, J. Buth, S. M. van Sterkenburg, H. J. Verhagen, E. Buskens, and D. E. Grobbee. Two-year outcomes after conventional or endovascular repair of abdominal aortic aneurysms. *N Engl J Med*, 352(23):2398–2405, 2005.

[14] G. Borgefors. Hierarchical chamfer matching: a parametric edge matching algorithm. *IEEE Trans Pattern Anal*, 10:849–865, 1988.

[15] F. Bornemann and T. März. Fast image inpainting based on coherence transport. *J Math Imaging Vis*, 28:259–278, 2007.

[16] R. P. Brent. *Algorithms for Minimization without Derivatives*. Prentice Hall, 1973.

[17] J. Canny. A computational approach to edge detection. *IEEE Trans Pattern Anal*, 8(6):679–698, 1986.

[18] P. Cao, F. Verzini, G. Parlani, L. Romano, P. D. Rango, V. Pagliuca, and G. Iacono. Clinical effect of abdominal aortic aneurysm endografting: 7-year concurrent comparison with open repair. *J Vasc Surg*, 40(5):841–848, 2004.

[19] T. W. G. Carrell, B. Modarai, J. R. I. Brown, and G. P. Penney. Feasibility and limitations of an automated 2d-3d rigid image registration system for complex endovascular aortic procedures. *J Endovasc Ther*, 17:527–533, 2010.

[20] V. Caselles, F. Catté, T. Coll, and F. Dibos. A geometric model for active contours in image processing. *Numer Math*, 66(1):1–31, 1993.

[21] E. L. Chaikof, J. D. Blankensteijn, P. L. Harris, G. H. White, C. K. Zarins, V. M. Bernhard, J. S. Matsumura, J. May, F. J. Veith, M. F. Fillinger, R. B. Rutherford, and K. C. Kent. Reporting standards for endovascular aortic aneurysm repair. *J Vasc Surg*, 35(5):1048–1060, 2002.

[22] T. F. Chan and L. A. Vese. Active contours without edges. *IEEE Trans Image Process*, 10(2):266–277, 2001.

[23] T. F. Cootes, C. J. Taylor, D. H. Cooper, and J. Graham. Active shape models - their training and application. *Comput Vis Image Und*, 61(1):38–59, 1995.

[24] M. A. Craeger and J. Loscalzo. Diseases of the aorta. In A. S. Fauci, E. Braunwald, D. L. Kasper, S. L. Hauser, D. L. Longo, J. L. Jameson, and J. Loscalzo, editors, *Harrison's Principles of Internal Medicine*, volume 2. McGraw-Hill Medical, 17th edition, 2008.

[25] D. Cremers, R. Mikael, and R. Deriche. Review of statistical approaches to level set segmentation: Integrating color, texture, motion and shape. *Int J Comput Vision*, 72(2):195–215, 2007.

[26] F. J. Criado. Fundamental skills and "endo-habits". In *Endovascular Intervention: Basic Concepts & Techniques*. Futura Publishing, 1999.

[27] R. H. Daffner. *Clinical Radiology. The Essentials*. Lippincott Williams & Wilkins, 3rd edition, 2007.

[28] P. E. Danielsson. Euclidean distance mapping. *Comput Graph Image Process*, 14(3):227–248, 1980.

[29] M. de Bruijne, B. van Ginneken, M. A. Viergever, and W. J. Niessen. Adapting active shape models for 3D segmentation of tubular structures in medical images. In *Proc. Int Conf Information Processing in Medical Imaging (IPMI)*, volume 2732 of *LNCS*. Springer, 2003.

[30] H. Delingette. General object reconstruction based on simplex meshes. *Int J Comput Vision*, 32(2):111–146, 1999.

[31] G. Delso and S. Ziegler. PET/MRI system design. *Eur J Nucl Med Mol Imaging*, 36(Suppl 1):S86–S92, 2008.

[32] S. Demirci, M. Baust, O. Kutter, F. Manstad-Hulaas, H.-H. Eckstein, and N. Navab. Disocclusion-based 2d-3d registration for aortic interventions. *Medical Physics*, 2011. Accepted.

[33] S. Demirci, O. Kutter, F. Manstad-Hulaas, R. Bauernschmitt, and N. Navab. Advanced 2D-3D registration of endovascular aortic interventions: Addressing dissimilarity in images. In *Proc. SPIE Medical Imaging: Visualization, Image-Guided Procedures*, volume 6918. SPIE, 2008.

[34] S. Demirci, G. Lejeune, and N. Navab. Hybrid deformable model for aneurysm segmentation. In *Proc. IEEE Int Symp Biomedical Imaging: From Nano to Macro (ISBI)*. IEEE Computer Society, 2009.

[35] S. Demirci, F. Manstad-Hulaas, and N. Navab. Quantification of aortic deformation after EVAR. In *Proc. SPIE Medical Imaging: Visualization, Image-Guided Procedures, and Modeling*, volume 7261. SPIE, 2009.

[36] A. P. Dempster, N. M. Laird, and D. B. Rubin. Maximum likelihood from incomplete data via the em algorithm. *J Roy Stat Soc B Met*, 39(1):1–38, 1977.

[37] J. Egger, S. Großkopf, T. O'Donnell, and B. Freisleben. A software system for stent planning, stent simulation and follow-up examinations in the vascular domain. In *Proc. IEEE Int Symp Computer-Based Medical Systems (CBMS)*. IEEE Computer Society, 2009.

[38] K. Eide, A. Ødegård, H. O. Myhre, S. Lydersend, S. Hatlinghus, and O. Haraldseth. DynaCT during EVAR a comparison with multidetector ct. *Eur J Vasc Endovasc Surg*, 37(1):23–30, 2009.

[39] K. R. Eide, A. Ødegård, H. O. Myhre, and O. Haraldseth. Initial observations of endovascular aneurysm repair using Dyna-CT. *J Endovasc Ther*, 14:65 – 68, 2007.

[40] S. Eiho, H. Imamura, and N. Sugimoto. Preoperative and intraoperative image processing for assisting endovascular stent grafting. In T. Ibaraki, T. Inui, and K. Tanaka, editors, *Proc. Int Conf Informatics Research for Development of Knowledge Society Infrastructure (ICKS)*. IEEE Computer Society, 2004.

[41] K. Engel, M. Hadwiger, J. M. Kniss, C. Rezk-Salama, and D. Weiskopf. *Real-Time Volume Graphics*. AK Peters, Ltd., 2006.

[42] A. G. Filler. The history, development and impact of computed imaging in neurological diagnosis and neurosurgery: CT, MRI, and DTI. *Nature Precedings*, 2009. Available at

http://precedings.nature.com/documents/3267/version/5/files/npre20093267-5.pdf.

[43] M. F. Fillinger, S. P. Marra, M. Raghavan, and F. E. Kennedy. Prediction of rupture risk in abdominal aortic aneurysm during observation: Wall stress versus diameter. *J Vasc Surg*, 37(4):724–732, 2003.

[44] J. M. Fitzpatrick and J. B. West. The distribution of target registration error in rigid-body point-based registration. *IEEE Trans Med Imaging*, 20:917–927, 2001.

[45] L. Flórez-Valencia, J. Montagnat, and M. Orkisz. 3D graphical models for vascular-stent pose simulation. In *Proc. Int Conf Computer Vision and Graphics (ICCVG)*. Springer, 2004.

[46] A. F. Frangi, W. J. Niessen, K. L. Vincken, and M. A. Viergever. Multiscale vessel enhancement filtering. In *Proc. Int Conf Medical Image Computing and Computer Assisted Intervention (MICCAI)*, volume 1496 of *LNCS*. Springer, 1998.

[47] G. R. Gadowski, D. B. Pilcher, and M. A. Ricci. Abdominal aortic aneurysm expansion rate: Effect of size and beta-adrenergic blockade. *J Vasc Surg*, 19(4): 727–731, 1994.

[48] S. C. Geller and the members of the Society of Interventional Radiology Device Forum. Imaging guidelines for abdominal aortic aneurysm repair with endovascular stent grafts. *J Vasc Interv Radiol*, 14:S263/S264, 2003.

[49] D. Gerogiannis, C. Nikou, and A. Likas. Robust image registration using mixtures of t-distributions. In *Proc. Int Conf Computer Vision (ICCV)*. IEEE Computer Society, 2007.

[50] K. A. Giles, A. D. Hamdan, F. B. Pomposelli, M. C. Wyers, S. E. Dahlberg, and M. L. Schermerhorn. Population-based outcomes following endovascular and open repair of ruptured abdominal aortic aneurysms. *J Endovasc Ther*, 16:554–564, 2009.

[51] C. Göksu, P. Haigron, O. Acosta, and A. Lucas. Endovascular navigation based on real/virtual environments cooperation for computer assisted team procedures. In *Proc. SPIE Medical Imaging: Visualization, Image-Guided Procedures*, volume 5367. SPIE, 2004.

[52] J. Golzarian. Imaging after endovascular repair of abdominal aortic aneurysm. *Abdom Imaging*, 28:236–243, 2003.

[53] J. Golzarian and J. Struyven. Imaging of complications after endoluminal treatment of abdominal aortic aneurysms. *Eur Radiol*, 11:2244–2251, 2001.

[54] Y. Gouëffic, J.-P. Becquemin, P. Desgranges, and H. Kobeiter. Midterm survival after endovascular versus open repair of infrarenal aortic aneurysms. *J Endovasc Ther*, 12(1):47–57, 2005.

[55] N. E. Green, S. Y. J. Chen, J. C. Messenger, B. M. Groves, and J. D. Carroll. Three-dimensional vascular angiography. *Curr Probl Cardiol*, 29(3):104–142, 2004.

[56] R. K. Greenberg, S. Haulon, S. P. Lyden, S. D. Srivastava, A. Turc, M. J. Eagleton, T. P. Sarac, and K. Ouriel. Endovascular management of juxtarenal aneurysms with fenestrated endovascular grafting. *J Vasc Surg*, 39(2):279–287, 2004.

[57] M. Groher, D. Zikic, and N. Navab. Deformable 2d-3d registration of vascular structures in a one view scenario. *IEEE Trans. Med. Imag.*, 28(6):847–860, 2009.

[58] R. Hartley and A. Zisserman. *Multiple View Geometry*. Cambridge University Press, second edition edition, 2003.

[59] M. Hedin. The origin of the word stent. *Acta Radiol*, 38:937–939, 1997.

[60] B. H. Hill, Y. G. Wolf, W. A. Lee, F. R. Arko, C. Olcott IV, P. J. Schubart, R. L. Dalman, E. J. Harris, T. J. Fogarty, and C. K. Zarins. Open versus endovascular AAA repair in patients who are morphological candidates for endovascular treatment. *J Endovasc Ther*, 9:255–261, 2002.

[61] D. L. Hill, P. G. Batchelor, M. Holden, and D. J. Hawkes. Medical image registration. *Phys Med Biol*, 46(3):1–45, 2001.

[62] B. A. Howell, T. Kim, A. Cheer, H. Dwyer, D. Saloner, and T. A. M. Chuter. Computational fluid dynamics within bifurcated abdominal aortic stent-grafts. *J Endovasc Ther*, 14(2):138–143Kurt Liffman, PhDa, Michael M. D. Lawrence–Brown, FRACSb, James B. Semmens, PhDc, Anh Bui, PhDa, Murray Rudman, PhDa, and David E. Hartley, FIRb, 2007.

[63] C. Huang and O. Mitchell. A euclidean distance transform using grayscale morphology decomposition. *IEEE Trans Pattern Anal*, 16:443–448, 1994.

[64] X. Huang, D. N. Metaxas, and T. Chen. MetaMorphs: Deformable shape and texture models. In *Proc. IEEE Conf Computer Vision and Pattern Recognition (CVPR)*. IEEE Computer Society, 2004.

[65] P. J. Huber. *Robust Statistics*. John Wiley & Sons, Ltd., 1981.

[66] H. Imamura, N. Ida, N. Sugimoto, S. Eiho, S.-i. Urayama, and K. Ueno, Katsuya andx Inoue. Registration of preoperative CTA and intraoperative fluoroscopic images for assisting aortic stent grafting. In *Proc. Int Conf Medical Image Computing and Computer Assisted Intervention (MICCAI)*, volume 2489 of *LNCS*. Springer, 2002.

[67] K. Irie, Y. Murayama, T. Saguchi, T. Ishibashi, M. Ebara, H. Takao, and T. Abe. Dynact soft-tissue visualization using an angiographic C-arm system: Initial clinical experience in the operating room. *Neurosurgery*, 62(3):266–272, 2008.

[68] E. M. Isselbacher. Thoracic and abdominal aortic aneurysms. *Circulation*, 111: 816–828, 2005.

[69] M. Jacob, T. Blu, and M. Unser. Efficient energies and algorithms for parametric snakes. *IEEE Trans Image Process*, 13(9):1231–1243, 2004.

[70] S. Kaneko, Y. Satoh, and S. Igarashi. Using selective correlation coefficient for robust image registration. *Pattern Recogn*, 36:1165–1173, 2003.

[71] M. Kass, A. Witkin, and D. Terzopoulos. Snakes: Active contour models. *Int J Comput Vision*, 1(4):321–331, 1988.

[72] A. Khamene, P. Bloch, W. Wein, M. Svatos, and F. Sauer. Automatic registration of portal images and volumetric CT for patient positioning in radiation therapy. *Med Image Anal*, pages 96–112, Feb. 2006.

[73] A. Klein, L. J. Oostveen, M. J. W. Greuter, Y. Hoogeveen, L. J. Schultze Kool, C. H. Slump, and W. K. J. Renema. Detectability of motions in aaa with ecg-gated cta: a quantitative study. *Med Phys*, 36(10):4616–4624, 2009.

[74] L. König, M. Groher, A. Keil, C. Glaser, M. Reiser, and N. Navab. Semi-automatic segmentation of the patellar cartilage in mri. In *Proc Workshop Bildverarbeitung für die Medizin (BVM)*. Springer, 2007.

[75] C. W. Kotze, L. J. Menezes, R. Endozo, A. M. Groves, P. J. Ell, and S. W. Yusuf. Increased metabolic activity in abdominal aortic aneurysm detected by 18F-fluorodeoxyglucose (18F-FDG) positron emission tomography/computed tomography (PET/CT). *Eur J Vasc Endovasc Surg*, 38(1):93–99, 2009.

[76] P. Lacroute and M. Levoy. Fast volume rendering using a shear-warp factorization of the viewing transformation. In *Proc. SIGGRAPH*. ACM Press, 1994.

[77] S.-H. Lai. Robust image matching under partial occlusion and spatially varying illumination change. *Computer Visian and Image Understanding*, 78:84–98, 2000.

[78] G. Langs, N. Paragios, P. Desgranges, A. Rahmouni, and H. Kobeiter. Learning deformation and structure simultaneously: In situ endograft deformation analysis. *Medical Image Analysis*, In Press, Corrected Proof:–, 2010.

[79] G. Langs, N. Paragios, R. Donner, P. Desgrange, A. Rahmouni, and H. Kobreiter. Motion analysis of endovascular stent-grafts by MDL based registration. In *Proc. IEEE Workshop Mathematical Methods in Biomedical Image Analysis (MMBIA)*. IEEE Computer Society, 2007.

[80] D. LaRose. *Iterative X-ray/CT Registration Using Accelerated Volume Rendering*. PhD thesis, Carnegie Mellon University, 2001.

[81] I. Larrabide, M. Kim, L. Augsburger, M. C. Villa-Uriol, D. Rüfenacht, and A. F. Frangi. Fast virtual deployment of self-expandable stents: Method and in vitro evaluation for intracranial aneurysmal stenting. *Med Image Anal*, 2010. doi: 10.1016/j.media.2010.04.009.

[82] I. Larrabide, A. Radaelli, and A. Frangi. Fast virtual stenting with deformable meshes: Application to intracranial aneurysms. In *Proc. Int Conf Medical Image Computing and Computer Assisted Intervention (MICCAI)*, volume 5242 of *LNCS*. Springer, 2008.

[83] M. Levoy. Display of surfaces from volume data. *IEEE Comput Graph Appl*, 8 (3):29–37, 1988.

[84] X. Li, J. Yang, and Y. Zhu. Digitally reconstructed radiograph generation by an adaptive monte carlo method. *Phys Med Biol*, 51:2745–2752, 2006.

[85] R. Liao, Y. Tan, H. Sundar, M. Pfister, and A. Kamen. An efficient graph-based deformable 2D/3D registration algorithm with applications for abdominal

aortic aneurysm interventions. In *Proc. Int Workshop Medical Imaging and Augmented Reality (MIAR)*, volume 6326 of *LNCS*. Springer, 2010.

[86] K. Liffman, M. M. D. Lawrence-Brown, J. B. Semmens, A. Bui, M. Rudman, and D. E. Hartley. Analytical modeling and numerical simulation of forces in an endoluminal graft. *Journal of Endovascular Therapy*, 8(4):358–371, 2001.

[87] E. C. Lin and A. Alavi. *PET and PET/CT. A Clinical Guide*. Thieme Medical Publishers, 2nd edition, 2009.

[88] D. Magee, A. Bulpitt, and E. Berry. Level set methods for the 3D segmentation of CT images of abdominal aortic aneurysms. In *Proc. Medical Image Understanding and Analysis (MIUA)*. BMVA, 2001.

[89] D. Magee, A. Bulpitt, and B. Elizabeth. Combining 3D deformable models and level set methods for the segmentation of abnormal aortic aneurysms. In T. F. Cootes and C. J. Taylor, editors, *Proc. British Machine Vision Conf (BMVC)*. BMVA, 2001.

[90] J. Maintz and M. Viergever. A survey of medical image registration. *Med Image Anal*, 2(1):1–36, 1998.

[91] R. Malladi, J. A. Sethian, and B. C. Vemuri. Shape modeling with front propagation: A level set approach. *IEEE Trans Pattern Anal*, 17(2):158–175, 1995.

[92] F. Manstad-Hulaas, S. Ommedal, G.-A. Tangen, P. Aadahl, and T. Hernes. Side-branched AAA stent graft insertion using navigation technology: A phantom study. *Eur Surg Res*, 39:364–371, 2007.

[93] F. Manstad-Hulaas, G. A. Tangen, S. Demirci, M. Pfister, S. Lydersen, and T. A. Nagelhus Hernes. Endovascular image-guided navigation - validation of two volume-volume registration algorithms. *Minim Invasiv Ther*, 2010. Accepted.

[94] P. Markelj, D. Tomaževič, F. Pernuš, and B. Likar. Robust gradient-based 3-D/2-D registration of CT and MR to x-ray images. *IEEE Trans Med Imaging*, 27(12):1704–1714, 2008.

[95] Y. Masutani, T. Dohi, F. Yamane, H. Iseki, and K. Takakura. Interactive virtualized display system for intravascular neurosurgery. In *Proc. Joint Conf Computer Vision, Virtual Reality and Robotics in Medicine and Medical Robotics and Computer-Assisted Surgery (CVRMed-MRCAS)*, volume 1205 of *LNCS*. Springer, 1997.

[96] J. Mattes, I. Steingruber, M. Netzer, K. Fritscher, H. Kopf, W. Jaschke, and R. Schubert. Quantification of the migration and deformation of abdominal aortic aneurysm stent grafts. In *Proc. SPIE Medical Imaging: Image Processing*, volume 6144. SPIE, 2006.

[97] M. McGuire and H. Stone. Techniques for multiresolution image registration in the presence of occlusions. *IEEE Trans Geosci Remote*, 38(3):1476–1478, May 2000.

[98] National Electrical Manufacturers Association, 1300 N. 17th Street, Rosslyn, Virginia 22209 USA. *Digital Imaging and Communications in Medicine (DICOM)*, 2009.

[99] J. Nelder and M. R. Ashworth. A simplex method for function minimization. *Computer J*, 7:308–313, 1965.

[100] C. Nikou, F. Heitz, and J.-P. Armspach. Robust voxel similarity metrics for the registration of dissimilar single and multimodal images. *Pattern Recogn*, 32:1351–1368, 1999.

[101] I. M. Nordon, R. J. Hinchliffe, A. H. Malkawi, J. Taylor, P. J. Holt, R. Morgan, I. M. Loftus, and M. M. Thompson. Validation of DynaCT in the morphological assessment of abdominal aortic aneurysm for endovascular repair. *J Endovasc Ther*, 17(2):183–189, 2010.

[102] S. D. Olabarriaga, J.-M. Rouet, M. Fradkin, M. Breeuwer, and W. J. Niessen. Segmentation of thrombus in abdominal aortic aneurysms from CTA with nonparametric statistical grey level appearance modeling. *IEEE Trans Med Imaging*, 24(4):477– 485, 2005.

[103] R. C. Orth, M. J. Wallace, and M. D. Kuo. C-arm Cone-beam CT: General principles and technical considerations for use in interventional radiology. *J Vasc Interv Radiol*, 19:814–821, 2008.

[104] S. Osher and J. Sethian. Fronts propagating with curvature-dependent speed: Algorithms based on Hamilton–Jacobi formulations. *J Comput Phys*, 79:12–49, 1988.

[105] K. Ouriel, D. G. Clair, R. K. Greenberg, S. P. Lyden, P. J. O'Hara, T. P. Sarac, S. D. Srivastava, B. Butler, and E. S. Sampram. Endovascular repair of abdominal aortic aneurysms: Device-specific outcome. *J Vasc Surg*, 37:991–998, 2003.

[106] C. A. Pelizzari, G. T. Y. Chen, D. R. Spelbring, R. R. Weichselbaum, and C.-T. Chen. Accurate three-dimensional registration of CT, PET, and/or MR images of the brain. *J Comput Assist Tomogr*, 13(1):20–26, 1989.

[107] G. P. Penney, J. Weese, J. A. Little, P. Desmedt, D. L. G. Hill, and D. J. Hawkes. A comparison of similarity measures for use in 2-D3-D medical image registration. *IEEE Trans Med Imaging*, 17(4):586 – 595, 1998.

[108] P. Pérez, M. Gangnet, and A. Blake. Poisson image editing. *ACM Trans Graphic*, 22(3):313–318, 2003.

[109] S. Periaswamy and H. Farid. Medical image registration with partial data. *Med Image Anal*, 10:452–464, 2006.

[110] T. M. Peters. Image-guided surgery. In Y. Kim and S. C. Horii, editors, *Display and PACS*, volume 3 of *Handbook of Medical Imaging*, pages 103–153. SPIE, 2000.

[111] M. Petrou and C. Petrou. *Image Processing: The Fundamentals*. John Wiley & Sons, Ltd., 2nd edition, 2010.

[112] O. S. Pianykh. *Digital Imaging and Communications in Medicine (DICOM). A Practical Introduction and Survival Guide*. Springer, 2008.

[113] L. Piegl and W. Tiller. *The NURBS Book*. Springer, 1997.

[114] M. J. D. Powell. An efficient method for finding the minimum of a function of several variables without calculating derivatives. *Computer J*, 7(2):155–162, 1964.

[115] W. H. Press, S. A. Teukolsky, W. T. Vetterling, and B. P. Flannery. *Numerical Recipes in C: The Art of Scientific Computing*. Cambridge University Press, 2 edition, 1992.

[116] S. Pujol, P. Cinquin, M. Pecher, I. Bricault, and D. Viorin. Minimally invasive navigation for the endovascular treatment of abdominal aortic aneurysm: Preclinical validation of the endovax system. In *Proc. Int Conf Medical Image Computing and Computer Assisted Intervention (MICCAI)*, volume 2875 of *LNCS*. Springer, 2003.

[117] A. Raheem, T. Carrell, B. Modarai, and G. Penney. Non-rigid 2D-3D image registration for use in endovascular repair of abdominal aortic aneurysms. In *Proc. Medical Image Understanding and Analysis (MIUA)*. BMVA, 2010.

[118] C. Reeps, M. Essler, J. Pelisek, S. Seidl, H.-H. Eckstein, and B.-J. Krause. Increased 18F-fluorodeoxyglucose uptake in abdominal aortic aneurysms in positron emission/computed tomography is associated with inflammation, aortic wall instability, and acute symptoms. *J Vasc Surg*, 48(2):417–423, 2008.

[119] F. Rengier, T. F. Weber, F. L. Giesel, D. Böckler, H.-U. Kauczor, and H. von Tengg-Kobligk. Centerline analysis of aortic CT angiographic examinations: Benefits and limitations. *Am J Roentgenol*, 192:W255–W263, 2009.

[120] M. E. Ring. The story of dr. charles stent. *Journal of the History of Dentistry*, 49 (2):77–80, 2001.

[121] D. B. Russakoff, T. Rohlfing, D. Rueckert, R. Shahidi, D. Kim, and C. R. Maurer, Jr. Fast calculation of digitally reconstructed radiographs using light fields. In *Proc. SPIE Medical Imaging: Image Processing*, volume 5032. SPIE, 2003.

[122] H.-P. W. Schlemmer, B. J. Pichler, M. Schmand, Z. Burbar, C. Michel, R. Ladebeck, K. Jattke, D. Townsend, C. Nahmias, P. K. Jacob, W.-D. Heiss, and C. D. Claussen. Simultaneous MR/PET imaging of the human brain: Feasibility study. *Radiology*, 248(3):1028–1035, 2008.

[123] J. A. Sethian. *Level Set Methods and Fast Marching Methods. Evolving Interfaces in Computational Geometry, Fluid Mechanics, Computer Vision, and Materials Science*. Number 3 in Cambridge Monographs on Applied and Computational Mathematics. Cambridge University Press, 2nd edition, 1999. ISBN 0-521-64557-3.

[124] C. E. Shannon. A mathematical theory of communication. *Bell Syst Tech J*, 27: 379–423, 623–656, 1948.

[125] D. W. Shattuck, G. Prasad, M. Mirza, K. L. Narr, and A. W. Toga. Online resource for validation of brain segmentation methods. *NeuroImage*, 45:431–439, 2009.

[126] G. W. Sherouse, K. Novins, and E. L. Chaney. Computation of digitally reconstructed radiographs for use in radiotherapy treatment design. *Int J Radiat Oncol Biol Phys*, 18(3):651–658, 1990.

[127] K. Sidorov, S. Richmond, and D. Marshall. An efficient stochastic approach to groupwise non-rigid image registration. In *Proc. IEEE Conf Computer Vision and Pattern Recognition (CVPR)*. IEEE Computer Society, 2009. ISBN 978-1-4244-3992-8.

[128] J. M. Smyth, D. G. Sutton, and J. G. Houston. Evaluation of the quality of CT-like images obtained using a commercial flat panel detector system. *Biomedical Imaging and Intervention Journal*, 2(4):e48, 2006.

[129] N. Strobel, O. Meissner, J. Boese, T. Brunner, B. Heigl, M. Hoheisel, G. Lauritsch, M. Nagel, M. Pfister, E.-P. Rührnschopf, B. Scholz, B. Schreiber, M. Spahn, M. Zellerhoff, and K. Klingenbeck-Regn. 3D imaging with flat-detector C-arm systems. In M. F. Reiser, C. R. Becker, K. Nikolaou, and G. Glazer, editors, *Multislice CT*, Medical Radiology, pages 33–51. Springer, 3rd edition, 2009.

[130] M. Subasic, S. Loncaric, and E. Sorantin. Model-based quantitative AAA image analysis using a priori knowledge. *Comput Meth Prog Bio*, 80(2):103–114, 2005.

[131] Z. Tauber, Z.-N. Li, and M. S. Drew. Review and preview: Disocclusion by inpainting for image-based rendering. *IEEE Transactions on Systems, Man, and Cybernetics*, 37:527–540, 2007.

[132] D. Tomaževič, B. Likar, and F. Pernuš. 3-D/2-D registration by integrating 2-D information in 3-D. *IEEE Trans Med Imaging*, 25(1):17–27, 2006.

[133] D. W. Townsend and T. Beyer. A combined PET/CT scanner: the path to true image fusion. *Br J Radiol*, 75:S24–S30, 2002.

[134] J. W. Tukey. *Exploratory Data Analysis*. Addison-Wesley Publishers, 1977.

[135] G. R. Upchurch and T. A. Schaub. Abdominal aortic aneurysm. *Am Fam Physician*, 73(7):1198–1204, 2006.

[136] S. Vaezy and V. Zderic. *Image-Guided Therapy Systems*. Engineering in Medicine & Biology. Artech House, 2009. ISBN 9781596931091.

[137] E. van de Kraats, G. Penney, D. Tomaževič, T. van Walsum, and W. Niessen. Standardized evaluation methodology for 2-D-3-D registration. *IEEE Trans Med Imaging*, 24(9):1177–1189, 2005.

[138] A. C. Venbrux, H. K. Chen, G. D. Tren, and D. A. Gagarin. A brief history of image-guided therapy: Endovascular milestones and nonvascular interventions. In M. A. Mauro, K. Murphy, K. Thomson, and C. L. Zollikofer, editors, *Image-guided interventions*, volume 1, pages 5–16. Saunders, 2008.

[139] A. Waldeyer and U. Waldeyer. *Anatomie des Menschen*, volume 1. Walter de Gruyter & Co., 6th edition, 1968.

[140] J. Weese, G. P. Penney, P. Desmedt, T. M. Buzug, D. L. G. Hill, and D. J. Hawkes. Voxel-based 2-D/3-D registration of fluoroscopy images and CT

scans for image-guided surgery. *IEEE Trans Inf Technol Biomed*, 1(4):284–293, 1997.

[141] I. Wolf, M. Vetter, I. Wegner, T. Bottger, M. Nolden, M. Schobinger, M. Hastenteufel, T. Kunert, and H. P. Meinzer. The medical imaging interaction toolkit. *Med Image Anal*, 9(6):594–604, 2005.

[142] C. Xu, D. Pham, and J. Prince. Image segmentation using deformable models. In M. Sonka and J. Fitzpatrick, editors, *Medical Image Processing and Analysis*, volume 2 of *Handbook of Medical Imaging*, pages 129–174. SPIE Press, 2000.

[143] C. Zahlten, H. Juergens, and H. Peitgen. Reconstruction of branching blood vessels from ct data. In *Proc. Eurographics Workshop Visualization in Scientific Computing*. Springer, 1994.

[144] C. K. Zarins, R. A. White, E. B. Diethrich, K. J. Hodgson, and T. J. Fogarty. Aneurx stent graft versus open surgical repair of abdominal aortic aneurysms: Multicenter prospective clinical trial. *J Vasc Surg*, 29(2):292–305, 1999.

[145] E. Zeitler, F. Olbert, K. Detmar, W. Krause, E. Ammann, F. Stösslein, T. Pollack, T. Schmidt, and M. Wucherer. Roentgen angiography. In E. Zeitler, editor, *Radiology of Peripheral Vascular Diseases*, Medical Radiology - Diagnostic Imaging and Radiation Oncology, pages 123–201. Springer, 2000.

[146] C. Zhang, M.-C. Villa-Uriol, and A. F. Frangi. Evaluation of an efficient GPU implementation of digitally reconstructed radiographs in 3D/2D image registration. In *Proc. SPIE Medical Imaging: Image Processing*, volume 7623. SPIE, 2010.

[147] F. Zhuge, G. D. Rubin, S. Sun, and S. Napel. An abdominal aortic aneurysm segmentation method: Level set with region and statistical information. *Med Phys*, 33(5):1440–1453, 2006.

[148] D. Zikic, B. Glocker, O. Kutter, M. Groher, N. Komodakis, A. Kamen, N. Paragios, and N. Navab. Linear intensity-based image registration by Markov Random Fields and Discrete Optimization. *Med Image Anal*, 14(4):550–562, 2010.

[149] D. Zikic, M. Sass Hansen, B. Glocker, and et al. Computing minimal deformations: Application to construction of statistical shape models. In *Proc. IEEE Conf Computer Vision and Pattern Recognition (CVPR)*. IEEE Computer Society, 2008.